Characterization of a novel Optical Micro-machined Ultrasound Transducer

Leinders, Suzanne

DOI
10.4233/uuid:474e53d4-de7a-483a-9ce8-18eb99f902fa

Publication date
2017

Document Version
Final published version

Citation (APA)
Leinders, S. (2017). *Characterization of a novel Optical Micro-machined Ultrasound Transducer*. [Dissertation (TU Delft), Delft University of Technology]. https://doi.org/10.4233/uuid:474e53d4-de7a-483a-9ce8-18eb99f902fa

Characterization of a novel Optical Micro-machined Ultrasound Transducer

Proefschrift

ter verkrijging van de graad van doctor
aan de Technische Universiteit Delft,
op gezag van de Rector Magnificus prof. ir. K.C.A.M. Luyben,
voorzitter van het College voor Promoties,
in het openbaar te verdedigen op
maandag 11 december 2017 om 12:30 uur

door

Suzanne Margriet LEINDERS

natuurkundig ingenieur geboren te Den Haag

Dit proefschrift is goedgekeurd door:

promotor:	prof. dr. ir. N. de Jong
promotor:	prof. dr. H.P. Urbach
co-promotor:	dr. ir. M.D. Verweij

Samenstelling promotiecommissie:

Rector Magnificus,	voorzitter
prof. dr. H.P. Urbach,	Technische Universiteit Delft, promotor
prof. dr. ir. N. de Jong,	Technische Universiteit Delft, promotor
dr. ir. M.D. Verweij,	Technische Universiteit Delft, co-promotor

onafhankelijke leden:

prof. dr. ir. A. van Keulen,	Technische Universiteit Delft
prof. dr. ir. R. Baets,	Ghent University
prof. dr. A.G.J.M. van Leeuwen,	Universiteit van Amsterdam
prof. dr. S. Manohar,	Universiteit Twente
prof. dr. ir. A.F.W. van der Steen,	Technische Universiteit Delft / Erasmus MC, reservelid

This research was supported by the IOP Photonic Devices programme of NL-Agency of the Dutch Ministry of Economic Affairs (project number IPD100026) and by TNO.

This free electronic version of this thesis can be downloaded from:
`http://repository.tudelft.nl`

ISBN 978-94-028-0870-4

Printed in The Netherlands.

Summary

We design and demonstrate a prototype ultrasound sensor based on a photonic micro-ring resonator integrated on a silicon membrane, and show that it can detect very low pressure ultrasound waves. The use of integrated photonics in future array transducers has several benefits: for instance it provides a small spatial footprint, compatibility with MRI due to the lack of electrical wiring, easy interrogation of the array of elements and ease of mass production, which may result in cost-effective fabrication of array transducers. To understand the working principle of the sensor, we have modeled the basic sensor element, fabricated the sensor and measured the response of the sensor to ultrasound. We have studied the response of the optical resonator separately before we integrate the resonator on the membrane and measure the response of the entire sensor. Besides the characterization of the sensor, we have expanded the existing knowledge of acoustical noise to determine the noise mechanism of the sensor.

Although ultrasound sensors are widely used in both industrial and medical applications, this thesis mainly focuses on use in medical diagnostics. Currently, ultrasound transducers are amongst others used to image such diverse objects as the coronary arteries, heart valves, liver, kidneys, prostate, brain and thyroid, but the most familiar application is the echo imaging of the fetus. The basis of the conventional ultrasound transducer consists of piezoelectric material that converts an electrical signal into a pressure wave and vice versa. During the last decades the single element transducers are replaced by one-dimensional arrays of sensors and during the last few years we have seen the emergence of two-dimensional arrays of sensors. Hence the development is focused on miniaturization of the sensor elements and fabrication of large dense arrays.

In this thesis, we have designed the basic element of a possibly future array ultrasound sensor that is based on integrated photonics. We have used the resulting

Optical Micro-machined Ultrasound Sensor (OMUS) to investigate the working principle. The element consists of a silicon optical waveguide that is coupled to a photonic racetrack-shaped optical resonator with a spatial footprint of 50 μm by 10 μm. The optical resonator is positioned on a silicon-dioxide membrane with a thickness of 2.5 μm and a diameter of about 100 μm. When a pressure wave is incident on the element, the membrane deforms and thus deforms the optical resonator. The deformation of the optical resonator shifts the optical resonance frequencies. This shift is recorded by an external interrogation system.
We have fabricated the photonic circuit of the sensor in a semi-industrial CMOS line. The resulting wafer-piece (die) contains 220 nm high and 400 nm wide silicon waveguides on top of a 2 μm thick silicon-dioxide layer on top of a 250 μm thick silicon substrate. Next, we have deposited a 0.5 μm thick silicon dioxide cladding on top of the die to isolate the waveguide from the water. Finally, we have created the membrane by locally removing the entire silicon substrate with use of deep reactive ion etching from the back of the die.
The prototype sensor is used to give proof of concept. We have used a laser and photo-receiver to interrogate the optical resonator and a conventional ultrasound transducer to transmit the pressure waves that were received by the sensor. We have found that the sensor had a resonance frequency of 0.76 MHz with a -6 dB bandwidth of 19 %. Furthermore, we have demonstrated that this prototype is capable of detecting pressures as low as 0.4 Pa. The latter matches the performance of the state of the art piezo-electric transducers while the spatial footprint of our sensor is 65 times smaller.
The sensor elements were further investigated by characterizing the strain-induced shift of the resonances of the optical resonator. We have applied a well defined strain to the racetrack resonators and have identified three different influences on the shift of resonances; dispersion, change in effective index and change in track-length. We have found that the linear wavelength shift per applied strain varies between 0.5 and 0.75 pm/microstrain depending on the width of the waveguide and the orientation of the silicon crystal for infrared light around 1550 nm wavelength. The influence of the increasing ring circumference is about three times larger than the influence of the change in waveguide effective index, and the two effects oppose each other.
The influence of the membrane is investigated by applying increasing static loadings to the sensor. In this study, we have integrated a short optical resonator on the membrane, which experiences a radial deformation rather than a uniform elongation. The measurement results show a non-linear response with high sensitivity at the beginning of the curve where small loadings are applied and lower sensitivity to the larger loadings.
The dynamic behavior of the sensor is investigated with a laser vibrometer. Due to simultaneous read-out of the sensor and the vibrometer, the read-out of the sensor can be compared to the vibration of the membrane and vibration of the entire sensor. We were able to show that the sensitivity of the sensor to low pressure signals is indeed induced by the membrane of the sensor, as the back of the sensor shows no significant vibrations. Furthermore, we have shown that the resonance frequency of the sensor can be tuned using different membrane diameters.

The noise level of our sensor is different from conventional ultrasound transducers due to the lack of electrical circuits. The noise of the optical sensor is only caused by acoustical noise, which is not well described in literature. Therefore, we have expanded the existing knowledge of acoustical noise by analyzing two mechanisms of acoustical noise. We show that in thermodynamic equilibrium the noise power delivered by the medium to the sensor balances the noise power delivered by the sensor to the medium. Moreover, we show that for sensors with vanishing aperture area, the noise pressure due to the molecular motion in the medium will reach a well-defined finite limit.

Samenvatting

In dit proefschrift ontwerpen en demonstreren we een prototype ultrageluidsensor die bestaat uit een optische micro-ring-resonator op een silicium membraan. We laten zien dat deze sensor zeer lage ultrageluid drukgolven kan detecteren. Het gebruik van geïntegreerde optica in toekomstige matrix tranducenten heeft verschillende voordelen: de technologie past bijvoorbeeld op een klein oppervlak, is te combineren met MRI omdat er geen elektrische bedrading nodig is, maakt dat een matrix van elementen makkelijk uitleesbaar is en is via massa productie te produceren hetgeen mogelijk resulteert in kosteneffectieve fabricatie van matrix transducenten. Om de werking van de sensor te begrijpen hebben we een model gemaakt van het basis element, deze sensor gefabriceerd en de respons op ultrageluid gemeten. We hebben eerst apart de respons van de optische resonator bestudeerd voordat we de resonator in het membraan hebben geïntegreerd en de respons van de hele sensor hebben gemeten. Naast het karakteriseren van de sensor hebben we de bestaande kennis van akoestische ruis verruimd om het ruismechanisme van de sensor te kunnen bepalen.

Hoewel ultrageluidsensoren worden gebruikt in zowel industriële als medische toepassingen, focust dit proefschrift zich op de medische diagnostiek. De meest bekende toepassing hierin is de echo van een foetus, maar de ultrageluidsensoren worden ook gebruikt om beelden te maken van allerlei objecten zoals de kransslagaders, hartkleppen, lever, nieren, prostaat, hersenen en schildklier. De basis van de conventionele ultrageluidtransducenten bestaat uit piëzo-elektrisch materiaal dat een elektrisch signaal in een drukgolf converteert en andersom. Al sinds tientallen jaren hebben enkel-elementstranducenten plaatsgemaakt voor een ééndimensionale array van transducentelementen. Als gevolg daarvan heeft de ontwikkeling zich met name gericht op het verkleinen van de transducentelementen en het fabriceren van matrices met hoge dichtheid van elementen.

In dit proefschrift hebben we het basis element ontworpen van een mogelijk toekomstige matrix ultrageluidsensor dat gebaseerd is op geïntegreerde optica. We hebben de resulterende optische micro-gefabriceerde ultrageluidsensor (OMUS) gebruikt om de werking daarvan te onderzoeken. Het element bestaat uit een optische golfgeleider van silicium die aan een optische ellips-vormige resonator wordt gekoppeld. Deze resonator heeft een spatieel oppervlak van 50 μm bij 10 μm. De optische resonator is gepositioneerd op een membraan van siliciumdioxide dat een dikte heeft van 2.5 μm en een diameter rond de 100 μm. Wanneer een drukgolf het element raakt vervormt het membraan en daarmee ook de optische resonator. De deformatie van de optische resonator zorgt voor een verschuiving van zijn optische resonantiefrequenties. Deze verschuiving wordt geregistreerd door een extern uitlees systeem.
We hebben het optische circuit van de sensor in een semi-industriële CMOS lijn gefabriceerd. De resulterende silicium schijf (wafer) bevat 220 nm hoge en 400 nm brede silicium golfgeleiders op een 2 μm dikke siliciumdioxide laag op een 250 μm dik slicium substraat. Hierna hebben we de golfgeleiders met een 0.5 μm dikke laag slicium bedekt om de golfgeleiders van het water te isoleren. Tenslotte hebben we het membraan gemaakt door lokaal via de achterkant met een diepe reactieve ion ets het volledige silicium substraat te verwijderen.
Het prototype sensor is gebruikt om te laten zien dat het concept werkt. We hebben gebruik gemaakt van een laser en fotodiode om de optische resonator uit te lezen en een conventionele ultrageluidtranducent om de drukgolf op te wekken. We hebben een resonantie frequentie van 0.76 MHz gevonden met een -6 dB bandbreedte van 19 %. Verder laten we zien dat dit prototype een minimale druk van 0.4 Pa kan detecteren. Deze druk komt overeen met die van de meest moderne piëzo-elektrische trandsucenten terwijl het oppervlak van onze sensor 65 keer kleiner is.
De sensorelementen zijn verder onderzocht door het karakteriseren van de rekgeïnduceerde verschuiving van de resonanties van de optische resonatoren. We hebben een goed gedefinieerde rek aangebracht op de ellips-vormige resonatoren en hebben drie verschillende invloeden op de resonatieverschuiving kunnen onderscheiden; dispersie, verschil in effectieve index en verschil in baanlengte. We hebben voor infrarood licht met een golflengte rond 1550 nm een variatie tussen 0.5 en 0.75 pm/microrek van de lineaire golflengte-verschuiving per aangebrachte rek gevonden, die afhankelijk is van de breedte van de golfgeleider en de oriëntatie van het silicium kristal. De invloed van de toenemende baanomtrek is ongeveer drie keer zo groot als de invloed van het verschil in de effectieve index van de golfgeleider. Daarnaast werken de twee effecten tegengesteld.
De invloed van het membraan is onderzocht door een toenemende statische last op de sensor aan te brengen. In dit onderzoek is een korte optische resonator op het membraan geïntegreerd, die een radiële deformatie ondervindt in plaats van een uniforme verlenging. De meetresultaten laten een niet-lineaire respons zien met hoge gevoeligheid in het begin van de curve waar kleine lasten worden aangebracht en lagere gevoeligheid voor de hogere lasten.
Het dynamische gedrag van de sensor is met een laservibrometer onderzocht. Door het gelijktijdig uitlezen van de sensor en de vibrometer kan de meetwaarde van de

sensor vergeleken worden met de vibratie van het membraan en de vibratie van de gehele sensor. Hierdoor kunnen we laten zien dat de gevoeligheid van de sensor voor lage druk signalen inderdaad door het membraan wordt geïnduceerd omdat de achterkant van de sensor geen significante trillingen laat zien. Verder laten we zien dat de resonantiefrequentie van de sensor kan worden beïnvloed door gebruik van membranen met verschillende diameter.
Het ruisniveau van onze sensor verschilt van conventionele ultrageluidsensoren door het ontbreken van elektrische circuits. De ruis van de optische sensor wordt alleen veroorzaakt door akoestische ruis, die niet goed is beschreven in de literatuur. Daarom hebben we de bestaande kennis van akoestische ruis uitgebreid door twee ruismechanismen van akoestische ruis te analyseren. We laten zien dat in thermodynamisch evenwicht het ruis vermogen dat door de omgeving aan de sensor wordt afgegeven in balans is met het ruis vermogen dat door de sensor aan zijn omgeving wordt afgegeven. Bovendien laten we zien dat voor sensoren met een oneindige klein oppervlak de ruis druk door moleculaire beweging in het medium een goed gedefinieerde eindige limiet bereikt.

Contents

Chapter

1

General introduction

This thesis describes the development and characterization of an ultrasound sensor based on integrated photonics. The use of light as information carrier makes this sensor different from the state-of-the-art piezo-electric ultrasound transducers. It provides a large data transfer capacity due to a broad bandwidth. Moreover the sensor is made using standard Complementary Metal Oxide Semiconductor (CMOS) fabrication processes, which allows for mass production. To design a high quality sensor that has comparable or even better image qualities than the state-of-the-art transducers, complete understanding of the sensor is necessary. Therefore we investigated the optical, mechanical and acoustical aspects of the sensor.
This chapter starts with an introduction of the main background of medical imaging and development of conventional ultrasound transducers (Sec. 1.1). Then we describe the aim of the research that was carried out in Sec. 1.2. In this part, we briefly describe the working principle of the sensor to get some understanding of the sensor. For a detailed description of the sensor as well as its operating principle we refer the reader to Chapter 4. In Sec. 1.3 we will discuss the development in the use of guided light in sensors and the semiconductor industry as fabrication platform. The outline of this thesis is presented in Sec. 1.4.

1.1 Medical imaging

Medical ultrasound is often used for diagnostic imaging of patients. Compared to other imaging techniques as CT and MRI, it has a lot of benefits; the images are real-time, it is safe (no radiation), inexpensive and the system is portable. The name ultrasound imaging refers to the use of high ($\geq$ 1 MHz) frequency sound waves to image the inside of the body. A device, named transducer, is used to

emit soundwaves into the body. These waves partly reflect on the inhomogeneities inside the body. The transducer receives the reflected waves (echoes) and with use of the time of flight the axial depth of the tissue can be determined. A single transmission provides the location of the scatterers in the beam line of the transducer. To create an image, multiple lines are needed and hence the area of interest has to be scanned. Three typical ultrasound images are shown in Figure 1.1 with on the left an image of a fetus, in the middle an image of the 4 chambers and valves of the heart and on the right an ultrasound image of an artery.
The development of diagnostic ultrasound instrumentation as we know it today was initiated around the time of the end of the Second Wold War [1]. The conventional transducers used to make an image consist of piezoelectric material. Piezoelectricity is defined as an electrical polarization related to mechanical strain. The polarization is proportional to the strain and changes sign with it [2]. Thus piezoelectric materials accumulate an electric charge in response to an applied mechanical stress and vice versa. The first ultrasound transducers were made of Quartz. This material has a high mechanical strength and low internal friction, but needs large amplitude voltages to be driven. Later, piezoelectric ceramics were used which had an improved efficiency and could be processed into varying shapes and sizes. In 1954, lead titanate-zirconate compositions (PZT) were discovered as piezoelectric material which had the additional benefits of a larger operating temperature range [3]. Currently, PZT is still used as transduction material in the state-of-the-art transducers, while research for new materials like single crystals (e.g. Lead Magnesium Niobate-Lead Titanate (PMN-PT)) or composites continues [1].
The efficiency of a transducer in conversion of energy depends next to the material on the frequency of excitation. To improve the energy transfer between the piezoelectric material and the tissue, matching layers and backing layers are often used. A scheme of a conventional transducer is shown in Figure 1.2. This transducer contains a large backing block that prevents movement of the bottom part of the piezoelectric layer. The matching layer, which has an impedance in between the piezoelectric material and the tissue, is here indicated as plastic 'nose'.
Next to the development of new materials, other aspects of the transducers were also adapted. The transducers changed from single element transducers into arrays, which contain many small transducer elements in a line (linear array) or in a plane (matrix array). Arrays give the option to illuminate an entire area at once, or electrically scan the area of interest [1]. With these arrays higher resolution images could be obtained with a much faster acquisition time [4].
The transducers used for medical imaging are designed for specific applications. The materials, element dimensions, shape and resonance frequency are optimized to obtain the penetration depth and resolution needed for each procedure. The applications that require dense arrays with small outer dimensions of the transducer are the ones where our sensor can provide most added value. Such applications can be found in the field of intra-operative image guidance (e.g. Intravascular Cardiac Echography (ICE)), where the device should not interfere with the procedure [5], or in the field of internal medical diagnostics, for instance Transesophageal Echocardiography (TEE) or Intravascular Ultrasound (IVUS). In these last two diagnostic applications the transducer is positioned on a catheter which is posi-

tioned inside the body. With a TEE image the catheter containing the transducer is positioned via the mouth or nose in the esophagus to image the hart. In case of IVUS the catheter is positioned inside a coronary artery to image the artery wall. In both cases a small transducer is required that nevertheless consists of multiple elements. Because the transducer is mounted on a catheter, the number of coaxial cables that connects the catheter to the computer is also limited, which provides an additional design challenge.

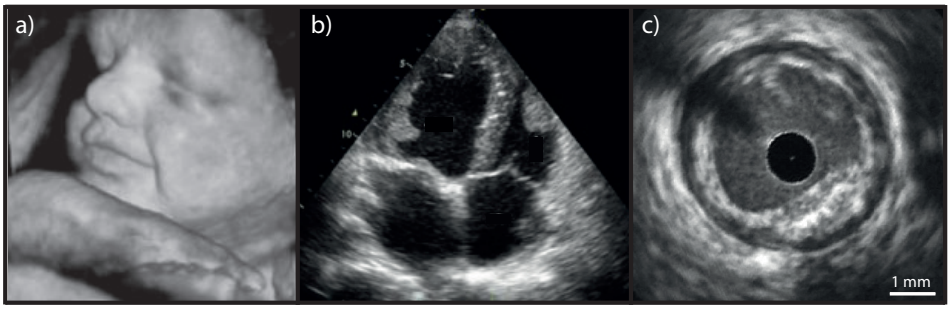

Figure 1.1: Ultrasound images of a) fetus obtained with 3D ultrasound [6], b) apical 4-chamber view of the heart obtained with transthoracic echocardiography [7] and c) a cross-section of a coronary artery obtained with IVUS [8].

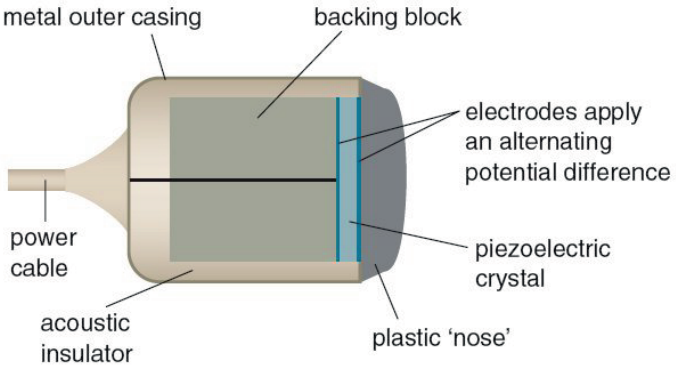

Figure 1.2: Scheme of ultrasound transducer [9].

1.2 An optical micro-machined ultrasound sensor for (medical) ultrasound

The aim of this research project was to design, fabricate and test an ultrasound sensor based on a new operation principle. This operation principle makes use of integrated photonics. Therefore our read-out system tracks the light spectrum over time. When an acoustical wave is incident on the sensor the transmission spectrum changes. We can explain this by describing the working principle of the sensor. The sensor consist of a photonic waveguide (bus waveguide) that guides the light from one side of the sensor towards the other side. We positioned a photonic ring resonator, which is a looped waveguide with distinct resonances, in the middle of the sensor. A part of the light spectrum is coupled from the photonic waveguide into this ring resonator. When we transmit a broad light spectrum through the bus waveguide and record the transmission spectrum at the end of the waveguide, instead of a flat spectrum we measure resonance dips consistent with the resonance frequencies of the ring resonator. We want to obtain a modulation of this spectrum due to ultrasound waves. This is done by positioning the ring resonator on an acoustical membrane. When a pressure wave is incident on the acoustical membrane, the membrane and thus the integrated ring resonator will deform. The deformation of the ring resonator influences the position of the resonances in the transmission spectrum. When one resonance is monitored over time using light with a very narrow spectrum, an incident pressure wave causes a time dependent shift of this resonance dip, which is observed as a modulation of the transmitted light intensity.
A main benefit of this new operating principle is the sensors in-susceptibility to electromagnetic interference. Therefore the sensor can be used in combination with MRI and other radiative environments. An other advantage is the possibility to stack data of several sensors in the spectrum. As a result only a single fiber is required as read-out of an entire array.
To get a good understanding of this sensor and be able to determine the feasibility as ultrasound sensor we investigated several aspects. We studied the optical components on the chip [10] as well as the influence of strain on the ring resonators (Chapter 3). We provided proof of concept with the first ultrasound measurements performed with a prototype (Chapter 4). We determined the influence of the membrane with a static pressure analysis and a study of the membrane motion (Chapter 5). Finally we derived a theory about the noise pressure levels that determines the minimal pressure level that can be measured with this type of sensor (Chapter 6).

1.3 Integrated photonic systems and micro-machining fabrication technology

Our sensor uses light as information carrier to benefit from fiber optics. Fiber optics, first developed in the 1970s, revolutionized the telecommunications industry. Compared to copper wires, optical fibers have the benefit of low attenuation and

interference, high reliability over long distances, a long life span and a very high information capacity [11].
We choose silicon and silicondioxide as materials for the index-guided based photonic waveguides. This allows us to use silicon-on-insulator technology for fabrication and hence profit from 50 years of development in semiconductor fabrication technology. This mainly means ease of fabrication and hence mass production.
Chip production today is based on photolithography. In this process high energy UV-light is shone through a mask upon a photosensitive film covering the silicon wafer. The illuminated part of the photosensitive layer forms the pattern of the chip and is developed into a layer that protects the underlying silicon. With etching processes the silicon that is not protected by the mask is removed. The wafer is cleaned by removing the mask. Most designs require several of these fabrication sequences [12].
Lots of structures can be created with this fabrication technique, but there are limitations that have to be taken into account when a design is made. For instance, there are variations present in the height of the silicon light-guiding layer and the chip can contain structures that have a slightly different size than designed for. Furthermore the lithography can only be optimized for one feature size, meaning that only this feature size is according to specifications. A final consideration is the fact that the sides of the patterns are not perfectly straight, but have an angle of about 10 degrees [10].

1.4 Outline of this thesis

With this brief introduction to the different fields involved we have obtained a general idea why this new sensor can be of importance to the medical field. In the remaining part of this thesis, we discuss the work done to obtain this sensor as well as the investigation of the different aspects of the sensor.
Chapter 2 presents a short overview of the theory that is important for the design of our sensor. It first describes the basic concepts that we used to model the sensor. The second part of this chapter describes the modeling results. With the models we obtained possible dimensions and corresponding resonance frequencies for our prototype device. We also calculated the first values of the pressure levels that could be received.
Chapter 3 studies the shift in the optical resonances due to an applied static mechanical strain to the ring resonator. The influence of different physical aspects on the ring resonator is investigated, such as: the elongation of the track, the change in cross-section of the waveguide due to the Poisson ratio, the change in the refractive index of the silicon and silicondioxide due to the photo-elastic effect and the dispersion in the waveguide.
Chapter 4 presents the proof-of-concept of the sensor. We present the first measurement results of the response of our sensor to an acoustical pressure wave. We determined the transfer function and hence its resonance frequency. We found a noise equivalent pressure that indicated that we fabricated a very sensitive ultrasound sensor.

Chapter 5 describes the characterization of the sensor. We investigated what the behavior of the sensor is under static and dynamic loading as well as the initial shape. Due to the fabrication technique of the silicon wafer, we found that initial strain is present, which influences the behavior of the membrane. Instead of linear theory, large deflection theory is needed to understand the static pressure measurements. Furthermore it is shown that only the membrane itself is significantly responding to the ultrasound waves.
Chapter 6 presents a theory to determine the noise level of small sensors. The noise floor of our sensor is different from the state-of-the-art transducers due to the lack of piezoelectric material. Hence our sensor is only prone to the noise generated by thermal motion of the atoms in the membrane and the water, while the piezoelectric transducers also have to deal with the high electrical noise from the electrical impedance.
Chapter 7 concludes and summarizes the thesis.

Chapter

2

Basic concepts and membrane design

Abstract – To be able to design a prototype sensor the basic concepts of the sensor should be known. This chapter describes the basis concepts of photonic waveguides, couplers and ring resonators as well as the linear theory for membrane deflection. With use of these concepts the membrane thickness and diameters are obtained. It is shown that a membrane thickness of 1.2 μm of silicon left underneath the 2.5 μm silicondioxide results in the most induced strain in the layer of the photonic waveguide for a resonance frequency of 1 MHz. Membrane diameters from 60 to 100 μm result in resonance frequencies of 3.2 to 0.9 MHz in water. Calculations showed a minimum detectable pressure level in the order of 600 Pa, which is sufficient for ultrasound sensing.

This chapter is based on the following publication:

S. M. Leinders, W. J. Westerveld, J. Pozo, P. L. M. J. van Neer, K. W. A. van Dongen, H. P. Urbach, N. de Jong, and M. D. Verweij, "Membrane design of an all-optical ultrasound receiver," in *Proceedings IEEE International Ultrasonics Symposium*, Prague, Jul. 2013, pp. 2175–2178

The general concept of the sensor is that the transmitted light traveling through the optical waveguide is modulated by the mechanical deformation of the optical ring resonator due to an incident ultrasound wave. To design such a sensor we need to understand the concepts of guided light and its mechanical response to pressure. An overview of the main concepts is given in the first part of this chapter, starting with the theory of photonic waveguides followed by the linear theory of membrane deflection. The second part shows the first modeling results for the dimensions and the corresponding resonance frequency of the sensor. These are used to obtain an estimate for the membrane diameter and thickness as starting values for the design of the prototype.

2.1 Photonic waveguides

This section describes the theory for high-index-contrast silicon waveguides. It only describes the theory that is of interest in our design. The reader is referred to [10] for a broader description of the theory and newly derived theory for these kind of waveguides. We start with the description of waves that can propagate in a waveguide (Section 2.1.1). Then the coupling of light from the straight waveguide towards the ring resonator via a directional coupler is described (Section 2.1.2) and we finalize with the description of a ring resonator (Section 2.1.3).

2.1.1 General description of a dielectric photonic waveguide

Photonic waveguides confine light and transport it over a given distance. The confinement is done by index guiding where the core of the waveguide has a higher refractive index than the surrounding. The photonic waveguides that are discussed are rectangular waveguides made of silicon. They have a SiO_2 burried oxide (BOX) substrate and an air or SiO_2 cladding. The waveguides have a typical height of 220 nm and width of 400 nm. The assumed free-space wavelength λ of the light is 1.55 μm. A schemamtic picture of such a silicon-on-insulator (SOI) waveguide is shown in Figure 2.1a, with its fundamental transverse electric (TE) mode depicted in Figure 2.1b. The fundamental mode has most of its energy in the

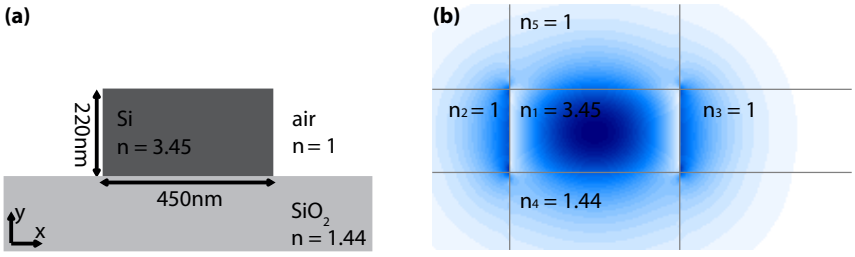

Figure 2.1: Cross-section of a SOI waveguide. a) Sketch of the waveguide b) Sketch of the E_x component of the fundamental mode in color. Dark blue represents a large field, white represents zero field [10].

center of the waveguide. The modes can be described with Maxwell's equations. In our description we approximate silicon and silicon dioxide as linear dielectrics with permittivity ϵ, which means that the material polarization is proportional to the electric field. We neglect magnetic behavior of the dielectrics by using the permeability of vacuum μ_0. All optical descriptions given are valid for monochromatic light with angular frequency ω and vacuum wavelength $\lambda = \omega/2\pi c$ where c is the speed of light in vacuum. The physical electromagnetic fields are described by the real components of the complex vector fields $\boldsymbol{\mathcal{E}}$ and $\boldsymbol{\mathcal{H}}$ of the electric and magnetic fields respectively. Maxwell's complex equations for monochromatic light in an isotropic linear dielectric medium without charges are given by [13]

$$\nabla \times \boldsymbol{\mathcal{E}} = -i\omega\mu_0 \boldsymbol{\mathcal{H}}, \tag{2.1}$$

$$\nabla \times \boldsymbol{\mathcal{H}} = i\omega\epsilon \boldsymbol{\mathcal{E}}, \tag{2.2}$$

$$\nabla \cdot \epsilon\boldsymbol{\mathcal{E}} = 0, \tag{2.3}$$

$$\nabla \cdot \boldsymbol{\mathcal{H}} = 0. \tag{2.4}$$

The latter two equations (2.3) and (2.4) are not independent and follow directly from the first two equations (2.1) and (2.2). The refractive index n depends on the permittivity as $n = \sqrt{\epsilon/\epsilon_0}$, with ϵ_0 the permittivity of vacuum. The permittivity profile $\epsilon(x, y, z)$ describes the devices as is indicated in Figure 2.1a and hence describes how the electromagnetic field behaves.

Electromagnetic fields in a homogeneous isotropic medium without charges obey the wave equations

$$(\nabla^2 + n^2k^2)\boldsymbol{\mathcal{E}} = 0, \tag{2.5}$$

$$(\nabla^2 + n^2k^2)\boldsymbol{\mathcal{H}} = 0, \tag{2.6}$$

with $k = \omega/c$ the free-space propagation constant [13, Ch. 9]. A dielectric waveguide is fully described by its permittivity profile $\epsilon(x, y)$ which is invariant in the z-direction, i.e. the direction in which the light propagates. We may assume that the propagating wave solutions have the form

$$\boldsymbol{\mathcal{E}}(x, y, z) = \boldsymbol{E}(x, y)e^{-i\beta z}, \qquad \boldsymbol{\mathcal{H}}(x, y, z) = \boldsymbol{H}(x, y)e^{-i\beta z}, \tag{2.7}$$

with β the propagation constant.
To find a solution in the form of Eq. 2.7 for the light propagation through rectangular dielectric waveguides, we can use the extended description of Marcatili's approximate analytical approach [14] or numerical mode solvers.
The field on the chip has to deal with losses. These losses are introduced by imperfections of the silicon and by waveguide bends. In case of the waveguide bends the mode in the bend changes with respect to the mode of the straight waveguide. This happens because the wave fronts at the outside of the bend have to propagate faster than the wave fronts at the inside. As a result the power of the mode moves towards the outside of the bend [15]. This effect is stronger for sharper bends. When we include losses the electrical field of the TE mode is described by

$$\boldsymbol{\mathcal{E}}(x, y, z) = \boldsymbol{E}(x, y)e^{-i\beta z - \alpha_p z}, \tag{2.8}$$

with α_p the propagation loss.
The effective index is often expressed in terms of the propagation constant as

$$n_e \equiv \frac{\beta}{k}. \tag{2.9}$$

The effective group index n_g is defined as

$$n_g \equiv \frac{\partial \beta}{\partial k}. \tag{2.10}$$

We can also find an explicit expression for the group index in terms of the first-order dispersion in the effective index n_e as

$$n_g = n_e - \lambda \frac{\partial n_e}{\partial \lambda}. \tag{2.11}$$

In our case, we only use a small wavelength span around a center wavelength λ_c. Therefore we approximate the wavelength-dependence of the effective index $n_e(\lambda)$ as linear so that

$$\beta(\lambda) \approx 2\pi \left[\frac{n_e(\lambda_c) - n_g(\lambda_c)}{\lambda_c} + \frac{n_g(\lambda_c)}{\lambda} \right]. \tag{2.12}$$

2.1.2 Directional couplers

It is possible to couple light from one waveguide into another by means of a directional coupler. Such a directional coupler consists of two parallel single-mode waveguides positioned close together as is shown in Figure 2.2a-b. We use a directional coupler to couple a fraction of the light from the straight waveguide into the ring resonator. The electric field in the coupler $\mathcal{E}^c$ can be approximated as a superposition of the two modes of the isolated waveguides a and b. The amplitudes of the two modes vary along the length of the coupler as is shown in Figure 2.2c. The electromagnetic field is approximated as

$$\mathcal{E}^c(x, y, z) \approx E^a(x, y)u_a(z) + E^b(x, y)u_b(z), \tag{2.13}$$

with u_a and u_b the complex modal amplitudes of waveguides a and b respectively and E^a and E^b the modal electric fields of the waveguides. When light propagates through waveguide b at the start of the coupler, i.e. $z = 0$, all energy is in this waveguide and therefore the amplitude of this mode is maximal and the mode in waveguide a is zero ($u_a(0) = 0$). At the effective coupling length of the coupling, i.e. $z = \tilde{L}$, the amplitudes of both modes in the coupler is given by

$$u_b(\tilde{L}) = \tau u_b(0), \quad u_a(\tilde{L}) = \kappa u_b(0). \tag{2.14}$$

The effective coupling length $\tilde{L} = L + \Delta L$ consist of the length of the coupler L and an contribution ΔL from a part of the bends of the waveguide. The complex amplitudes τ and κ are calculated using coupled mode theory. The derivation is

given in [10], but the final formula for the coupling amplitudes for two waveguides is given by

$$\tau = \left(\cos s\tilde{L} - \frac{i\delta}{s}\sin s\tilde{L}\right) e^{i(\beta_b+\kappa_{bb}-\delta)\tilde{L}}, \tag{2.15}$$

$$\kappa = -\left(\frac{i\kappa_{ab}}{s}\sin s\tilde{l}\right) e^{i(\beta_b+\kappa_{bb}-\delta)\tilde{L}}, \tag{2.16}$$

where β_b is the propagation constant of mode b, κ_{bb} is the correction to this propagation constant originating from the other waveguide, $\delta \equiv 1/2(\beta_b + \kappa_{bb} - \beta_a - \kappa_{aa})$ is the difference between the corrected propagating constants of the guides and $s = \sqrt{\kappa_{ba}\kappa_{ab} + \delta^2}$ is the coupling coefficient. Coupling coefficient κ_{ab} represents the coupling from the mode of waveguide b to the mode of waveguide a and κ_{ba} represents the coupling from the mode of waveguide a to the mode of waveguide b. These coefficients dominate s. The guides in the coupler that we study are designed to be identical, but we experimentally observed non-zero δ in our couplers.

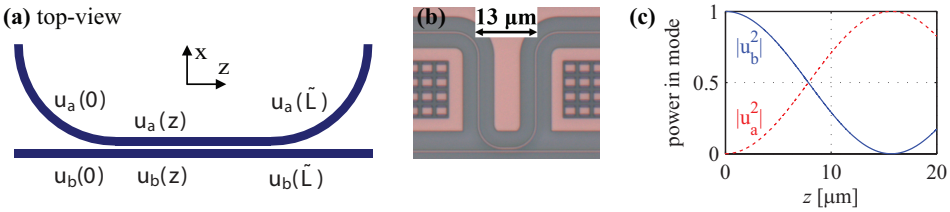

Figure 2.2: Directional coupler and its behavior. a)Top view of a directional coupler with bus waveguide b and second waveguide a. b) Optical microscope photo of a directional coupler in SOI. The very narrow pinkish lines are the waveguides. c) The normalized power in each mode at a certain coupling length z. The coupling coefficient s is 0.1 for identical waveguides ($\delta = 0$) [10].

2.1.3 Ring resonators

Ring resonators consist of a looped optical waveguide and a coupling mechanism to couple light into the loop. The shape of the ring is arbitrary. We use racetrack resonators which are elongated rings with a straight part between the bends (Fig. 2.3). As coupling mechanism we use two directional couplers (Sec 2.1.2). A losless coupler without reflections is generally described by [16]

$$\begin{pmatrix} b_1 \\ b_2 \end{pmatrix} = \begin{pmatrix} \tau^* & \kappa \\ -\kappa^* & \tau \end{pmatrix} \begin{pmatrix} a_1 \\ a_2 \end{pmatrix}, \tag{2.17}$$

where a_1, a_2, b_1 and b_2 are the waveguide terminals and κ and τ are the coupling coefficients from the bus waveguide to the ring resonator and vice versa as indicated in Figure 2.3. The relation between the coupling coefficients is given by $|\tau|^2+|\kappa|^2 = 1$ and the * is the complex conjugate.

When the wave travels through the racetrack resonator it experiences after one round-trip a phase delay ϕ_ρ and a decay by a factor α, so that

$$a_2 = \alpha e^{i\phi_\rho} b_2. \tag{2.18}$$

We can obtain the power in the output waveguide $|b_1|^2$ by substituting Eq.(2.18) in Eq.(5.1) to find

$$b_2 = \frac{-\kappa^*}{1 - \tau\alpha e^{i\phi_\rho}} a_1, \tag{2.19}$$

and

$$b_1 = \left(\tau^* - \frac{\kappa\kappa^*\alpha e^{i\phi_\rho}}{1 - \tau\alpha e^{i\phi_\rho}}\right) a_1, \tag{2.20}$$

with $\tau = |\tau|e^{i\phi_\tau}$ and ϕ_τ the phase delay due to the coupler. We can rewrite Eq.(2.20) into

$$b_1 = \frac{-\alpha + |\tau|e^{i(\phi_\rho+\phi_\tau)}}{e^{-i\phi_\rho} - \alpha|\tau|e^{i\phi_\tau}} a_1. \tag{2.21}$$

We compute $|b_1|^2 = b_1 b_1^*$ and use $2\cos\theta = e^{i\theta} + e^{-i\theta}$ to get

$$|b_1|^2 = \frac{\alpha^2 + |\tau|^2 - 2\alpha|\tau|\cos\theta}{1 + \alpha^2|\tau|^2 - 2\alpha|\tau|\cos\theta} |a_1|^2, \tag{2.22}$$

where $\theta = \phi_\rho + \phi_\tau$ is the net phase delay of traveling through the ring and coupler. In case of two bus waveguides with identical couplers we include the transmission through the second coupler in the track round-trip by replacing α with $\alpha|\tau|$. Eq.(2.23) changes then into

$$|b_1|^2 = \frac{(\alpha^2 + 1 - 2\alpha\cos\theta)|\tau|^2}{1 + \alpha^2|\tau|^4 - 2\alpha|\tau|^2\cos\theta} |a_1|^2, \tag{2.23}$$

with in this case $\theta = \phi_\rho + 2\phi_\tau$. When the racetrack including the couplers has length l, the transmission through the directional couplers with effective length $\tilde{L}$ is given by Eq. (2.15). The phase delay due to propagation through a waveguide with length $l - 2\tilde{L}$ is equal to $\phi_\rho = \beta(l - 2\tilde{L})$. The total phase delay of the ring is therefore given by

$$\theta = -\beta l + 2\delta\tilde{L} - 2\kappa_{bb}\tilde{L} + 2arg\left\{\cos s\tilde{L} - \frac{i\delta}{s}\sin s\tilde{l}\right\}. \tag{2.24}$$

For a coupler with two identical waveguides, neglecting the κ_{bb} and with linear dispersion of the effective index, the phase delay reduces to

$$\theta = -\beta l = -2\pi\left[\frac{n_e - n_g}{\lambda_c} + \frac{n_g}{\lambda}\right] l, \tag{2.25}$$

with $n_e \equiv n_e(\lambda_c)$ and $n_g \equiv n_g(\lambda_c)$.
When we measure the transmission spectrum of a waveguide coupled with a single directional coupler to a ring resonator, given by $|b_1|^2$ as a function of wavelength,

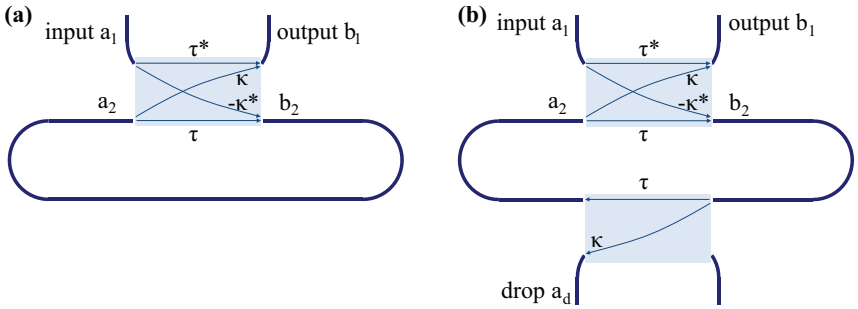

Figure 2.3: Sketch of ring resonator and (a) one directional coupler or (b) two directional couplers. [10].

we observe resonance dips for $\theta = 2\pi m$ with m an integer number. The resonance wavelengths λ_m for two identical waveguides in the coupler are given by

$$m\lambda_m = n_e(\lambda_m)l. \tag{2.26}$$

A typical transmission spectrum for our sensor is shown in Figure 2.4. The difference between two successive resonance dips is indicated by the free spectral range (FSR). We may approximate the FSR by linearizing the relation between m and $\lambda(m)$ in Eq.(2.26) and then computing $|\Delta\lambda|$ for $\Delta m = 1$ to obtain,

$$\Delta\lambda_{FSR} = \left|\frac{\partial\lambda}{\partial m}\right|\Delta m = \frac{\lambda^2}{(n_e - \lambda\frac{\partial n_e}{\partial\lambda})l} = \frac{\lambda^2}{n_g l}. \tag{2.27}$$

At resonance we have $\cos\theta = 0$ and thus Eq.(2.23) becomes

$$|b_1|^2 = \frac{(\alpha - |\tau|)^2}{(1 - \alpha|\tau|)^2}|a_1|^2. \tag{2.28}$$

This relation shows that there is no transmission at the resonance wavelengths when $|\tau| = \alpha$, hence when the round-trip loss of the racetrack is equal to the power coupled to the racetrack. This condition is called critical coupling. The minimum transmitted power $|b_{1,\min}|^2$ occurs at resonance while the maximum transmitted power $|b_{1,\max}|^2$ occurs in between the resonances. The extinction ratio, defined as $r \equiv |b_{1,\min}|^2/|b_{1,\max}|^2$, and the full-width at half-max (FWHM) of the transmission spectrum show the shape of the resonances as a function of the waveguide and coupler properties and are given by

$$r = \frac{(\alpha - |\tau|)^2(1 + \alpha|\tau|)^2}{(\alpha + |\tau|)^2(1 - \alpha|\tau|)^2}, \tag{2.29}$$

and

$$\Delta\lambda_{FSR} = \frac{\lambda^2}{\pi l n_g}\cos^{-1}\left[\frac{2\alpha|\tau|}{1 + \alpha^2|\tau|^2}\right]. \tag{2.30}$$

The FWHM depends on the losses in the resonator and scales with the FSR, while for the extinction ratio the critical coupling is most important. When α is replaced

by $\alpha|\tau|$, Eq.(2.26)-(2.30) are also valid for two couplers, as the second coupler acts as an additional source of loss.

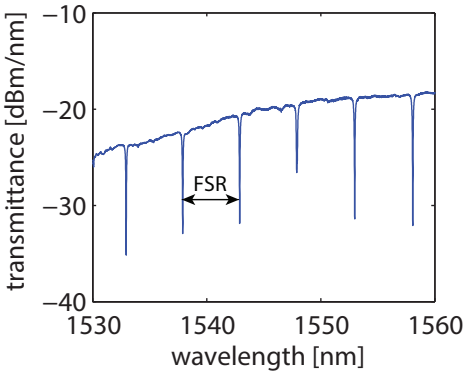

Figure 2.4: Measured transmission spectrum of a ring resonator. The FSR is indicated.

2.2 Membrane deflection

To obtain a sensitive sensor, it is essential to design a membrane with high strain values at the position of the optical ring resonator when it is deformed. In this subsection, we study the strain distribution on the membrane as well as the resonance frequency of the OMUS.

2.2.1 Static strain profiles

For small deflections of the membrane i.e. when the deflections of the plate are small in comparison with the thickness of the plate, the theory of pure bending of plates can be applied. It is assumed that the middle plane, or neutral surface, of the plate does not undergo any extension during bending [17]. When we consider a differential element of a thin plate with a thickness h and area $dx\ dy$ as is Figure 2.5, the governing equation of the deflection $w(r,\theta,t)$ due to an external loading q in polar coordinates is given by [17, 18]

$$D\nabla^4 w(r,\theta,t) + \rho h \frac{\partial^2 w(r,\theta,t)}{\partial t^2} = q(r,\theta,t), \tag{2.31}$$

where $\nabla^4 = \nabla^2\nabla^2$ with $\nabla^2 = \frac{\partial^2}{\partial r^2} + \frac{1}{r}\frac{\partial}{\partial r} + \frac{1}{r^2}\frac{\partial^2}{\partial \theta^2}$ the Laplacian in polar coordinates and ρ is the density of mass. The flexural rigidity D of the plate is given by

$$D = \frac{E}{1-\nu^2}\int_{-h/2}^{h/2} z^2 dz = \frac{Eh^3}{12(1-\nu^2)}, \tag{2.32}$$

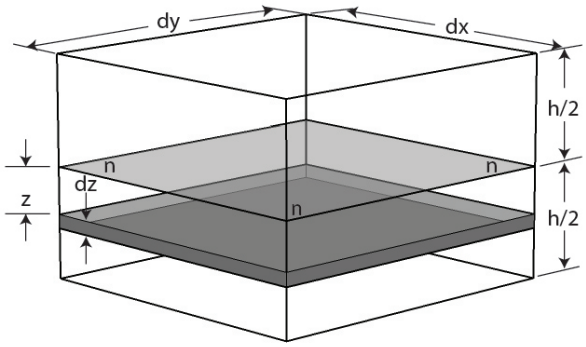

Figure 2.5: Differential element of a thin plate with neutral plane n at half the thickness h of the plate and lamina at z below the middle plane.

with E the Young's modulus and ν the Poisson ratio. When different materials are used, we integrate over the separate layers with their specific material properties to obtain the flexural rigidity of the entire plate [17].
The displacement $w(r, \theta, t)$ measures the deflection of the middle plane of the plate. When we look at a lamina with thickness dz located at a distance z below the middle plane n of the plate indicated in Figure 2.5, the normal strains defined as the relative elongation of the lamina ($\epsilon_l \equiv \Delta l/l$) are given by

$$\epsilon_x = \frac{z}{r_x}, \tag{2.33}$$

$$\epsilon_y = \frac{z}{r_y}, \tag{2.34}$$

where r_x and r_y are the radii of curvature in the x, z-plane and y, z-plane respectively. We assume small deflections and slopes and therefore the curvatures may be approximated with use of the second order derivatives of the displacement (e.g. $r_x \approx -1/\frac{\partial^2 w}{\partial x^2}$) such that

$$\epsilon_x = -z\frac{\partial^2 w}{\partial x^2}, \tag{2.35}$$

$$\epsilon_y = -z\frac{\partial^2 w}{\partial y^2}. \tag{2.36}$$

The shear strain is given by

$$\gamma_{xy} = -2z\frac{\partial^2 w}{\partial x \partial y}. \tag{2.37}$$

From Hooke's law the strains relate to the stresses as

$$\epsilon_x = \frac{1}{E}(\sigma_x - \nu\sigma_y), \tag{2.38}$$

$$\epsilon_y = \frac{1}{E}(\sigma_y - \nu\sigma_x), \tag{2.39}$$

with ν the Poisson ratio. Combining Eqs. (2.35)-(2.39) results in a radial and transverse stress along the thickness of the membrane in polar coordinates these stresses are

$$\sigma_r = \frac{Ez}{1-\nu^2}\left(\frac{\partial^2 w}{\partial r^2} + \nu\frac{\partial^2 w}{\partial \theta^2}\right), \tag{2.40}$$

$$\sigma_\theta = \frac{Ez}{1-\nu^2}\left(\frac{\partial^2 w}{\partial \theta^2} + \nu\frac{\partial^2 w}{\partial r^2}\right), \tag{2.41}$$

$$\tau_{r\theta} = G\gamma_{r\theta} = -2Gz\frac{\partial^2 w}{\partial r \partial \theta}. \tag{2.42}$$

In a static situation, Eq. (2.31) can be simplified to:

$$D\nabla^4\omega(r,\theta) = q(r,\theta). \tag{2.43}$$

With a symmetrical load the deflection of a circular membrane is independent of θ hence $w(r,\theta) = w(r)$. Assuming that the membrane has clamped boundaries, hence $w(a) = 0$, and $\frac{\partial w(a)}{\partial r} = 0$, and the deflection has a maximum at the center of the membrane, i.e. $\frac{\partial w(0)}{\partial r} = 0$, this equation can be solved resulting in [17]

$$w(r) = \frac{q}{64D}\left(a^2 - r^2\right)^2. \tag{2.44}$$

We can determine the maximum or minimum stress at the lower or upper face of the plate. These maximum or minimum stress is the same in the lower and upper face but has an opposite sign. In the radial direction of a face, the absolute maximum is found at the boundary of the plate where $\sigma_r = -3qa^2/(4h^2)$ and a slightly lower value is found at the center of the plate with opposite sign where $\sigma_r = 3(1+\nu)qa^2/(8h^2)$ [17]. We do not know the exact boundary conditions of our sensor as the membrane is part of the chip itself. When we therefore model the displacement of the chip under uniform loading we can get the displacement and radial curves for a 100 μm diameter membrane (Fig. 2.6). A typical curve of the radial strain in a layer has positive values at the edge of the membrane where it is extended, while towards the center negative values are present due to a compression of the surface. Between the center and edge is a circular area without radial strain which is around 1/3 of the radius from the edge of the membrane.

2.2.2 Resonance frequency of membranes

To obtain the fundamental mode of the membrane we solve Eq. (2.31) without loading. We assume a solution $w(r,\theta,t) = W(r,\theta)e^{-i\omega t}$ with ω the angular frequency and t the time. If we go through the mathematics, we find the solution for full circular plates as

$$W(r,\theta) = \{AJ_n(\beta r) + CI_n(\beta r)\}\begin{bmatrix}\sin n\theta \\ \cos n\theta\end{bmatrix}, \tag{2.45}$$

with J_n the Bessel function of the first kind, I_n the modified Bessel function of the first kind and $\beta^4 = \omega^2\rho h/D$ [18,19]. When we apply clamped boundary conditions

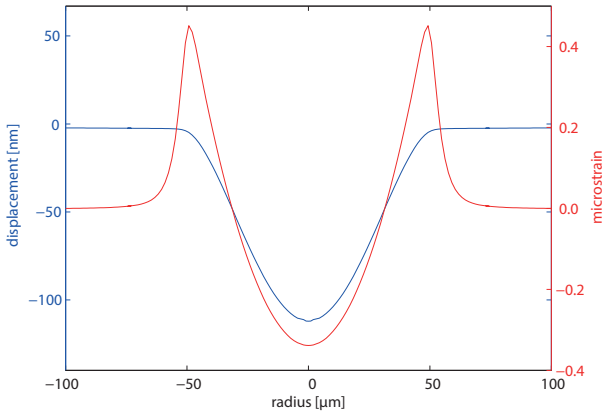

Figure 2.6: Typical displacement curve of a circular membrane with a radius of 50 μm (blue line) and corresponding radial strain curve in a lamina of the plate (red line).

we get

$$I_n(\beta a)J_n'(\beta a) - J_n(\beta a)I_n'(\beta a) = 0. \tag{2.46}$$

Each value of n in this equation will have an infinite number of roots, which give the resonance frequencies. We define $\lambda_{nm} = \beta_{nm}a$ where n is the integer arising in Eq. (2.46) and m is corresponding to the order of the root for a given n. The fundamental mode has for instance a value of $\lambda_{01}^2 = 10.216$. The normal modes are given by

$$W_{nm}(r,\theta) = \left\{ J_n(\beta_{nm}r) - \frac{J_n(\beta_{nm}a)}{I_n(\beta_{nm}a)} I_n(\beta_{nm}r) \right\} \begin{bmatrix} \sin n\theta \\ \cos n\theta \end{bmatrix}. \tag{2.47}$$

Because $\lambda_{nm}^2 = \omega a^2 \sqrt{\rho h/D}$, we are able to calculate the resonance frequency $f = \omega/2\pi$ in air which is given by [19]

$$f = \frac{1}{2\pi} \frac{\lambda_{nm}^2}{a^2} \sqrt{\frac{D}{\rho h}}. \tag{2.48}$$

One side of the sensor will be submerged in water instead of air, which will give an extra load on the membrane. The resonance frequency will shift downwards by a factor that could be approximated by

$$f_w = \frac{f_a}{\sqrt{1+\gamma\Gamma}}, \tag{2.49}$$

where f_w is the resonance frequency for water, f_a the resonance frequency for air, Γ a non-dimensional added virtual mass factor, which is a function of mode shapes and boundary conditions and $\gamma = \frac{\rho_w a}{\rho_p h}$ with ρ_w the density of mass of the water and ρ_p the density of mass of the plate [20].

2.3 Membrane modeling

The theory in the previous section demonstrated that the resonance frequency of the membrane can only be exactly determined for air and for known boundary conditions. To deal with water loading and unknown boundary conditions we have to solve the problem numerically. We like to obtain values for the ideal thickness of the membrane, given a certain resonance frequency and find the corresponding resonance frequency in water of certain membrane diameters. We will first describe the modeling parameters followed by the results of the static and dynamic simulations.

2.3.1 Specifications and modeling parameters

In the numerical simulation we use a 2D axis-symmetric domain and modeled the device as a 250 μm silicon layer below the 2.5 μm SiO_2 layer (including the top layer). The 220 nm thick silicon waveguides are neglected. We assume for simplicity that the strain induced at 0.5 μm from the top, i.e. the waveguide layer, will represent the strain induced in the waveguide. The acoustical membrane is created by removing a part of the substrate. In the static analyses, described in Section 2.3.2, the thickness of silicon left under the SiO_2 layer is varied each time. In the dynamic analyses, described in Section 2.3.2, we model three different membranes with diameters of 60 μm, 80 μm and 100 μm. In these dynamic models, the membranes consist only of SiO_2, and the area underneath the membrane is filled with air. The remaining part of the modeling domain is filled with water.
The discretization of the receiver design contained at least 12 points per wavelength. The water domain is large enough to avoid interference from reflecting waves from the boundaries of the domain. In both studies we used a density of mass of 2329 kg/m^3 for the silicon and an isotropic Young's modulus of 170 GPa and Poisson ratio of 0.28. The silica has a density of 2200 kg/m^3, Young's modulus of 70 GPa and a Poisson ratio of 0.17.

2.3.2 Modeling results

To analyze the strain profiles and determine the response of the receiver, we perform two different analyses which are described in this section. The first part is a static analysis by which we compute the dimensions of the membrane. The second part is a dynamic study in which the response and sensitivity of the receiver are obtained.

Static analysis

The acoustical membrane can be developed for all kinds of applications. We designed a membrane that has an acoustical resonance at 1 MHz when it is submerged in water. To find the optimal dimensions, i.e. inducing the highest amount of strain in the optical resonator, we investigate whether an optimum is present when the thickness of the membrane is varied. The thickness of the membrane consists of at least the 2.5 μm SiO_2 layer, so only the thickness of the silicon was varied from

Table 2.1: Response of three prototype receivers due to an incident plane wave

Membrane diameter [μm]	Resonance frequency [MHz]	Sensitivity [microstrain/kPa]	Minimum detection level [Pa]
60	3.2	1.3	1540
80	1.6	3.4	590
100	0.9	3.2	625

0 μm to 10 μm. For each thickness of the membrane the corresponding radius is calculated by Eqs. (2.48) and (2.49) to obtain a resonance frequency of 1 MHz. For every thickness and corresponding radius, we determine with a finite element model the maximum absolute strain that can be induced in the membrane. We used a static pressure of 1 kPa. The results show that the maximum strain varies from 0.17 to 0.45 microstrain. The maximum value is attained when 1.2 μm of silicon is left underneath the 2.5 μm SiO_2 layer.
Although an optimum exists, the difference in strain in the range of 0 μm to 4 μm of silicon is only a factor of 1.5. In the fabrication process of the membrane, the flatness and thickness of the silicon layer is difficult to control. A well-controlled fabrication can be performed when all the silicon up to the SiO_2 layer is removed, using a chemically selective etch process. Therefore we have finally choosen to remove all the silicon in the design of the prototypes and in the remaining study.

Dynamic analysis

We designed three prototypes with different membrane diameters to determine the response and influence of the membrane on the performance of the sensor. In a time domain analysis, we used an incident acoustic plane wave with Gaussian pulse shape with a maximum amplitude of 50 kPa and pulse width of 0.6 μs. The time and frequency response of the 80 μm diameter membrane are shown in Figure 2.7. The results of all the receivers are listed in Table 2.1. For every receiver, we numerically obtained the resonance frequency of the membrane. The maximum strain values, present in the time simulations, were used to calculate the sensitivity by dividing the strain by the maximum of the incoming pressure field. To determine the minimum pressure detection level, we assumed to have an optical detector with a resolution of 1 pm and we used 0.5 pm/microstrain for the shift in the light spectrum due to strain from [21].
The results show that our device can be well used for ultrasound sensing. The three times less sensitivity of the smallest membrane suggest that there is a minimum footprint of the element. Furthermore, we conclude that the membrane with a 80 μm diameter is the most sensitive receiver.

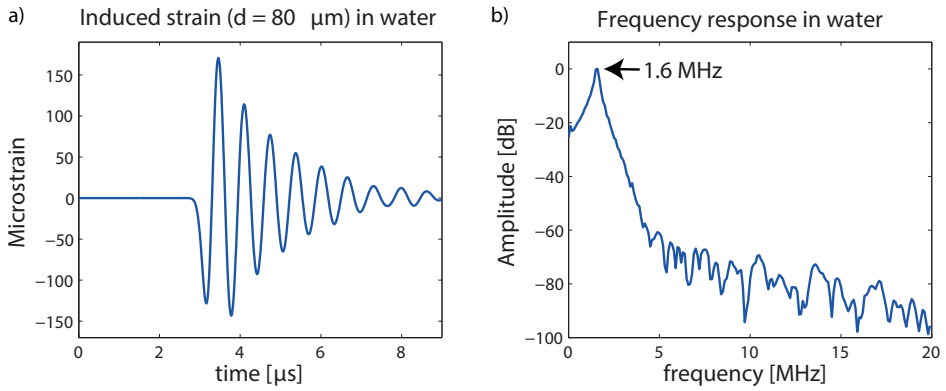

Figure 2.7: a) The induced strain by a propagating Gaussian pressure wave and b) the frequency response of the 80 μm diameter membrane. Both plots apply to the center point of the waveguide layer.

2.4 Conclusion

With use of the basic concepts of waveguides and membrane deflection we have been able to design a prototype sensor. When we look at the static strain profiles we conclude that the optical resonator needs to be positioned at maximum distance from the neutral plane, i.e. at the top or at the bottum, and either in the center or at the edge of the membrane. When the sensor is realized, the waveguide needs to be protected from the water and will therefore be positioned below a 0.5 μm cladding. Therefore the maximum distance from the neutral plane is a little bit less in the final design. Because of the current racetrack shape of the ring resonators we will position it in the center of the membrane where the largest area with similar strain values is present. Because this area with similar strain is limited, the maximum length of the ring resonator is limited to 2/3 of the membrane diameter.

The thickness of the membrane should in optimal situation contain a layer of 1.2 μm silicon underneath the silicondioxide for a membrane with resonance around 1 MHz. Although this optimum exist we prefer to build a prototype that could easily be compared to models and hence contains a flat and evenly thick membrane. Therefore we will remove all the silicon with a well-controlled chemically selective etch process.

The dynamic simulations show that the obtained sensitivity of the sensor is sufficient for ultrasound sensing. Furthermore is it possible to fabricate the membrane diameters that correspond to resonance frequencies in the MHz range.

Chapter

3

Optical characterization of strain sensors based on silicon waveguides

Abstract – Microscale strain gauges are widely used in micro electro-mechanical systems (MEMS) to measure strains such as those induced by force, acceleration, pressure or sound. We propose all-optical strain sensors based on micro-ring resonators to be integrated with MEMS. We characterized the strain-induced shift of the resonances of such devices. Depending on the width of the waveguide and the orientation of the silicon crystal, the linear wavelength shift per applied unit of strain varies between 0.5 and 0.75 pm/microstrain for infrared light around 1550 nm wavelength. The influence of changing ring circumference is about three times larger than the influence of the change in waveguide effective index, and the two effects oppose each other. The strong dispersion in 220 nm high silicon sub-wavelength waveguides accounts for a decrease in sensitivity of a factor 2.2 to 1.4 for waveguide widths of 310 nm to 860 nm. These figures and insights are necessary for the design of strain sensors based on silicon waveguides.

This chapter is based on the following publication:

W. J. Westerveld, S. M. Leinders, P. M. Muilwijk, J. Pozo, T. C. van den Dool, M. D. Verweij, M. Yousefi and H. P. Urbach "Characterization of integrated optical strain sensors based on silicon waveguides," in *JSTQE*, Vol. 11, No. 4, December 2013

Earlier results based on micro-ring resonators where we excited the fundamental TM-like mode of a 300 nm high silicon waveguide were published as W.J. Westerveld, J. Pozo, P.J. Harmsma, R. Schmits, E. Tabak, T.C. van den Dool, S.M. Leinders, K.W.A. van Dongen, H.P. Urbach, and M. Yousefi, "Characterization of a photonic strain sensor in silicon-on-insulator technology," *Optics Letters*, vol. 37, no. 4, pp. 479–481, Feb 2012.

3.1 Introduction

Microscale strain gauges are widely used in micro electro-mechanical systems (MEMS) to measure strains such as those induced by force, acceleration, pressure or (ultra)sound [22, 23]. These sensors are traditionally based on a piezoresistive or piezoelectric material which transduces the strain to an electrical signal. Alternatively, optical resonators can be used as sensing element, providing particular benefits: high-speed readout, small sensor size, small multiplexer size (1 mm^2), insensitivity to electromagnetic interference, and no danger of igniting gas explosions with electric sparks.
Integrated optics technology allows the optical strain sensors, as well as their multiplexing circuit, to be integrated with MEMS. The sensing elements and their multiplexers can often be fabricated in a single processing step. Silicon-on-insulator (SOI) has emerged as one of the focus platforms for integrated optics, and is relatively straightforward to integrate with MEMS, as MEMS are most commonly made of silicon. Micro-electronic research institutes have tailored CMOS fabrication processes to the demands of SOI optical circuits, and now offer cheap and reproducible wafer-scale fabrication [24, 25]. The high contrast of the refractive index of SOI ridge waveguides allows for a small device footprint, and single-mode guides have a cross-section of only 400×220 nm^2.
We employ ring resonators as sensing element. Such a resonator consists of a waveguide which is looped, forming a closed cavity which has specific optical resonance wavelengths. Any change in the size or in the refractive index of this waveguide shifts its resonances, and this shift can be accurately recorded.
Several groups have reported on sensor micro opto-electro-mechanical systems (MOEMS) that are based on silicon integrated optical ring resonators, such as strain gauges [26, 27], or pressure sensors [28–30]. An application of particular interest is as ultrasound sensor for medical intravascular ultrasonography (IVUS). IVUS has been recommended for the diagnostics of atherosclerosis [31, 32]. IVUS is an invasive technique for blood vessel imaging where the sensor is attached to a catheter and brought inside the artery. Using an array of sensors improves the image quality but wiring many piezoelectric sensors with coaxial cables requires too much space for this application. As solution, we proposed a micro-machined ultrasound transducer (MUT) with optical readout [33]. This sensor consists of a silicon ring resonator integrated in a membrane that deforms due to ultrasonic waves. Integrated optical multiplexers allow high-speed read-out of many sensors via one optical fiber and, moreover, insensitivity to electromagnetic interference allows usage inside MRI scanners.
The relation between strain and silicon waveguides is of broader interest than sensing. Electro-mechanical modulation of silicon optical resonators may be employed to modulate optical signals, for application in the field of telecommunication [34]. As alternative to silicon waveguide-based ring resonators, it is also possible to use photonic crystals cavities, which have their own dispersion relations [35]. Strain has also been used to modify the birefringence of larger SOI rib waveguides [36]. Strain is inevitable when using silicon photonic circuits on a flexible substrate [37]. Another interesting field of research is the strain-induced change in the electronic

band-gap and the optical refractive index of silicon, with the possibility to introduce second-order nonlinearity [38–40]. However, details of the relation between an applied strain and the shift in optical resonance of ring resonators have not been studied.
We characterized the shift of the resonance wavelengths which is caused by a well-defined strain. We quantified the contribution of three physical effects: the strain-induced change in circumference of the resonator, the strain-induced change in effective index of the waveguide, and the dispersion which is strong in sub-wavelength silicon waveguides. This knowledge is required for the design of mechanical sensors based on silicon integrated optics, such as ring resonators or Mach-Zehnder interferometers.
This chapter is organized as follows: first we present the devices which are used to study the effect of strain on silicon optical waveguides (Sec. 3.2), then we derive opto-mechanical theory describing these devices (Sec. 3.3), after which we detail the experimental setup and methodology (Sec. 3.4). The characterization and the analysis of the devices are presented in Sec. 3.5 and Sec. 3.6, respectively, and we draw some conclusions in Sec. 3.7.

3.2 Devices

In this section, we first describe the SOI-technology in which the devices are fabricated, secondly detail the ring resonators and then describe the sets of devices that we studied.
The integrated optical devices are in silicon-on-insulator technology, with 220 nm thick waveguides of mono-crystalline silicon. The guides are on top of a 2 μm thick buried oxide (BOX) layer which is on top of a 675 μm thick silicon substrate. We deposited a 2 μm thick SiO_2 cladding layer using plasma-enhanced chemical vapor deposition (PEVCD), so that the silicon waveguides are embedded in silica. The devices were fabricated via the EU-funded ePIXfab consortium at IMEC (Leuven, Belgium) [24, 25]. IMEC fabricated the devices in their CMOS line with 193 nm deep-UV lithography. The waveguides are not exactly rectangular but have a side-wall-angle of 10 degrees. We measured the average widths of the fabricated waveguides with a helium ion microscope (Carl Zeiss SMT), providing an accuracy of 15 nm.
We designed long racetrack-shaped ring resonators in an "add-drop" configuration (Fig. 3.1), and excite the "input" waveguide with infrared light with wavelengths λ around a center wavelength λ_c of 1550 nm. A directional coupler couples light from the "input/output" waveguide to the resonator, and an identical coupler is used half-way the racetrack to couple light to a "drop" waveguide. The transmitted spectrum $T(\lambda)$ in the "output" port has dips at the resonance wavelengths of the resonator. We characterized the couplers and 59% of the power is coupled from the waveguide to the track, such that the power which goes straight-through the coupler $|t|^2 = 41\%$. Having a strong coupling in a symmetric add-drop configuration gives resonance dips with good extinction ratio even for high losses in the racetrack or for variations in coupling (e.g. due to fabrication) [16].

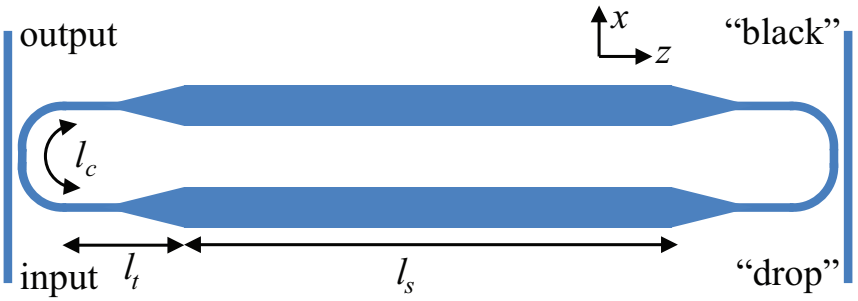

Figure 3.1: Sketch of racetrack resonator with in/output ports (not to scale). Long straight waveguide has length $l_s = 1000$ μm and width w. Taper section has length $l_t = 64.35$ μm (4.35 μm long waveguide of width 400 nm, taper with a length varying from 0 to 60 μm, followed by a waveguide of width w to close the space.) Coupler section has length l_c and consists of two 10 μm long parallel guides (width ∼400 nm, gap 220 nm), and bends with a radius of 5 μm.

Silicon is anisotropic, so its deformation depends on the direction in which a force is applied. Therefore two sets of devices were fabricated and characterized; one with the long side of the racetrack parallel to the ⟨110⟩ direction of the silicon crystal and one with the long side parallel to the ⟨100⟩ direction of the silicon crystal. Reference [41] explains the crystal planes in a "(100) wafer" as we used. We characterized the influence of the width of the waveguide on the shift in resonance, therefore each set of devices consists of resonators with waveguide widths varying from 310 nm up to 860 nm.

3.3 Theory

This section presents the theory of ring resonators such as presented in the previous section, i.e. a looped waveguide with a varying width. First, Sec. 3.3.1 presents the optical theory of ring resonators, then Sec. 3.3.2 derives the opto-mechanical theory. Sec. 3.3.3 applies the theory to the long racetrack resonators under study. The relations derived in this section are used as fitting function of the measured spectra, and as basis for the analysis of the measurements.

3.3.1 Ring and racetrack resonators

The transmitted optical power T of a micro-ring resonator with two lossless couplers in an add-drop configuration such as shown in Figure 3.1 is [16]

$$T = \frac{\alpha^2|t|^2 + |t|^2 - 2\alpha|t|^2\cos(\delta)}{1 + \alpha^2|t|^4 - 2\alpha|t|^2\cos(\delta)}, \tag{3.1}$$

where $|t|^2$ is the straight-through power of the coupler and α^2 is the power transmission due to one round-trip through the ring ($\alpha = 1$ means zero loss). T thus

describes the optical power transmitted from the input to the output of the connecting waveguide, and is wavelength dependent because δ is wavelength-dependent. The phase delay δ of one round-trip through the ring (including passing the couplers) is

$$\delta = \oint n_e(\rho, \lambda)\frac{2\pi}{\lambda}\mathrm{d}\rho = \langle n_e(\lambda)\rangle\frac{2\pi}{\lambda}l, \tag{3.2}$$

where the waveguide effective index $n_e(\rho, \lambda)$ is averaged over the position ρ in the track with circumference l as $\langle n_e(\lambda)\rangle \equiv \frac{1}{l}\oint n_e(\rho, \lambda)\mathrm{d}\rho$. The effective index in the coupler is approximated equal to the effective index of a single isolated waveguide. The strong modal dispersion in sub-wavelength silicon waveguides is approximated to be linear around the center wavelength λ_c, and is expressed in terms of the effective group index $n_g \equiv n_e - \lambda\frac{\partial n_e}{\partial \lambda}$, so

$$n_e(\rho, \lambda) = n_e(\rho) + \big(n_e(\rho) - n_g(\rho)\big)\big(\frac{\lambda}{\lambda_c} - 1\big) \tag{3.3}$$

where n_e and n_g at the right-hand-side, denoted without λ dependence, are evaluated at λ_c. As λ and ρ are independent,

$$\langle n_e(\lambda)\rangle = \langle n_e\rangle + (\langle n_e\rangle - \langle n_g\rangle)(\frac{\lambda}{\lambda_c} - 1), \tag{3.4}$$

from which it is observed that the transmission spectrum of a racetrack resonator with varying width is described by the same relation as a resonator with a single waveguide, but with averaged effective index $\langle n_e\rangle$ and group index $\langle n_g\rangle$.
Equation (3.1) with Eqs. (5.11) and (3.4) will be fitted to the measured resonance spectra to accurately obtain $\langle n_g\rangle$ and $\langle n_e\rangle$, from which the resonance wavelengths are calculated.

3.3.2 Strain-induced resonance shift of ring resonators

This section details the shift in the resonances of a ring resonator due to an applied mechanical strain. Four physical effects play a role when elongating a ring- or racetrack resonator. First, the circumference of the track l increases. Second, the cross section of the waveguide shrinks due to the Poisson effect. Third, the refractive indices of the silicon and SiO_2 change due to the photo-elastic effect. The latter two effects together influence the effective index n_e of the waveguide. Fourth, the shift in resonance is affected by the dispersion in the waveguide.
In our case, a homogeneous strain S_z is applied parallel to the long sides of the racetrack resonator (the z-direction). The transmitted spectrum of the connecting waveguide shows dips at the resonance wavelengths λ_m when $\delta = m2\pi$, or

$$m\lambda_m = \oint n_e(\rho, \lambda_m, S_z)\,(1 + S_\rho(\rho, S_z))\,\mathrm{d}\rho. \tag{3.5}$$

The effective index of the waveguide depends on a mechanical deformation. The local strain in the direction of the track S_ρ is taken into account by stretching each element $\mathrm{d}\rho$ to $(1 + S_\rho)\mathrm{d}\rho$. For the straight waveguide of the racetracks as in

Figure 3.1, the z- and ρ-directions coincide, whereas they do not for the coupler section. We found that the relation between an applied strain S_z and the shift in resonance wavelength is linear, which is explained by the fact that the applied strains are small. A description of this linear influence can be found by taking the first derivative of Eq. (5.12) with respect to S_z,

$$m\frac{\partial\lambda_m}{\partial S_z} = \oint\left\{\left(\frac{\partial n_e}{\partial S_z} + \frac{\partial n_e}{\partial\lambda_m}\frac{\partial\lambda_m}{\partial S_z}\right)(1+S_\rho) + n_e\frac{\partial S_\rho}{\partial S_z}\right\}\mathrm{d}\rho,$$

which we evaluate at zero strain (i.e. $S_z = S_\rho = 0$). Solving this equation for $\partial\lambda_m/\partial S_z$, substituting m from Eq. (5.12), and dividing by track circumference l gives

$$\frac{\partial\lambda_m}{\partial S_z} = \frac{\lambda_c}{\langle n_g\rangle l}\oint\left(\frac{\partial n_e}{\partial S_z} + n_e\frac{\partial S_\rho}{\partial S_z}\right)\mathrm{d}\rho, \tag{3.6}$$

with λ_c the resonance wavelength λ_m without deformation. This equation is easiest understood when considering a resonator with a single waveguide shape (i.e. $\langle n_e\rangle = n_e$ and $\langle n_g\rangle = n_g$). In that case,

$$\frac{\partial\lambda_m}{\partial S_z} = \underbrace{\frac{n_e}{n_g}}_{\text{dispersion}}\Big\langle\underbrace{\frac{\lambda_c}{n_e}\frac{\partial n_e}{\partial S_z}}_{\text{eff. index}} + \underbrace{\lambda_c\frac{\partial S_\rho}{\partial S_z}}_{\text{track-length}}\Big\rangle, \tag{3.7}$$

where the influence of the different physical effects are indicated. Without dispersion, $n_e/n_g = 1$. For the part of the track which is in the direction of the applied strain $S_\rho = S_z$, so $\partial S_\rho/\partial S_z = 1$, hence the contribution of the track-length change is simply λ_c.

3.3.3 Strain-induced resonance shift of long racetracks

We measured very long racetracks because this will allow for neglecting the influence of the tapers and the couplers. In the long racetrack resonators, Eq. (5.12) reads

$$m\lambda_m = 2l_s n_s(1+S_z) + \int_{\text{tapers}} n_e\,(1+S_\rho)\,\mathrm{d}\rho + \int_{\text{couplers}} n_e\,(1+S_\rho)\,\mathrm{d}\rho, \tag{3.8}$$

where the contributions of the different sections of the track are separated (see Fig. 3.1, with l_s, l_t, and l_c indicating the straight, taper and coupler sections, respectively) and n_s is the effective index of the long straight waveguide. We calculate the first-order influence of strain on this racetrack similarly to Eq. (3.6), and rewrite the equation such that the influence of the tapers and the couplers is

written as a correction to the shift caused by the long straight guides,

$$\begin{aligned}\langle n_g\rangle\frac{\partial\lambda_m}{\partial S_z} =&\lambda_c\left(\frac{\partial n_s}{\partial S_z}+n_s\right)\\ &+\frac{\lambda_c}{l}\int\limits_{\text{tapers}}\left(\frac{\partial n_e}{\partial S_z}+n_e\frac{\partial S_\rho}{\partial S_z}-\frac{\partial n_s}{\partial S_z}-n_s\right)\mathrm{d}\rho\\ &+\frac{\lambda_c}{l}\int\limits_{\text{couplers}}\left(\frac{\partial n_e}{\partial S_z}+n_e\frac{\partial S_\rho}{\partial S_z}-\frac{\partial n_s}{\partial S_z}-n_s\right)\mathrm{d}\rho.\end{aligned} \tag{3.9}$$

We will justify later that the second and third term of the right-hand-side of this equation are small compared to the first one, and hence can be neglected, resulting in

$$\langle n_g\rangle\frac{\partial\lambda_m}{\partial S_z}\approx\lambda_c\left(\frac{\partial n_s}{\partial S_z}+n_s\right). \tag{3.10}$$

The taper is a waveguide in the z-direction with a width varying from 400 nm up to the width w of the long section waveguide. The second term at the right-hand-side of Eq. (3.9) is the relative contribution of the taper to the resonance shift, with respect to the contribution of a waveguide with width w of the same length. The relative contribution of the taper is smaller than the relative contribution of a 400 nm wide waveguide of the same length. Using Eq. (3.10), it is thus found that the second term of the right-hand-side of Eq. (3.9) is smaller than

$$\frac{4l_t}{l}\left|\underbrace{\langle n_g\rangle\frac{\partial\lambda_m}{\partial S_z}}_{\text{width under study}}-\underbrace{\langle n_g\rangle\frac{\partial\lambda_m}{\partial S_z}}_{\text{width 400 nm}}\right|. \tag{3.11}$$

The third term of Eq. (3.9) comes from the effect of the couplers including the bend waveguides. This contribution can be either positive (as for the long waveguides) or negative (as the path-length might shrink due to the Poisson effect). We expect the magnitude to be smaller than twice the effect of a straight waveguide of equal length that is strained in its long direction. Thus the 3rd term in Eq. (3.9) is smaller in magnitude than

$$2\frac{2l_c}{l}\left(\langle n_g\rangle\frac{\partial\lambda_m}{\partial S_z}\right). \tag{3.12}$$

As will be shown in Sec 3.5, the maximum measured difference in $\langle n_g\rangle(\partial\lambda_m/\partial S_z)$ for the devices under study with different waveguide widths is 10%. For these long racetracks, $4l_t/l = 11\%$, so the second term in Eq. (3.9) is smaller than 1.1%. The third term is smaller than $4l_c/l = 5\%$. Equation (3.10) is used in the characterization of the measurements. We characterized both $\langle n_g\rangle$ and $\partial\lambda_m/\partial S_z$. The effective index of the straight waveguide n_s is computed with a numerical mode solver, which allows us to extract the strain-induced change in effective index.

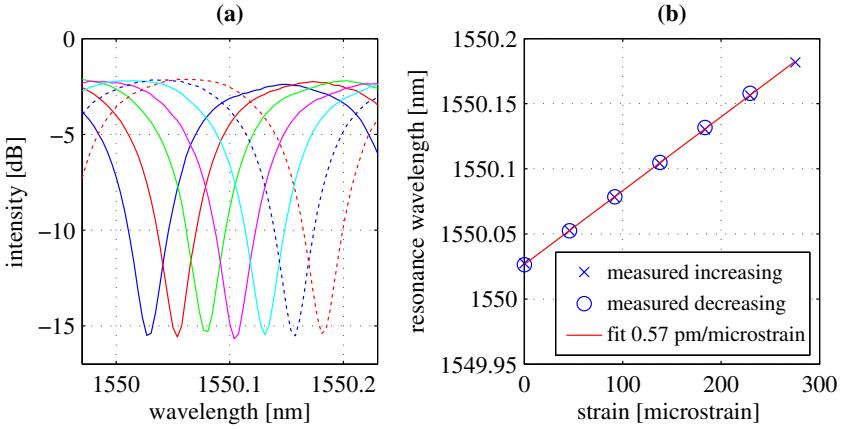

Figure 3.2: Example of resonance shift due to an applied strain. **(a)** Small span of 7 measured spectra for increasing values of applied strain. Resonance dips shift to the red. Racetrack in the <100> crystalline direction, with waveguide width 400 nm. **(b)** The wavelengths of the resonance dips λ_m in (a) are plotted versus the applied strain S_z. The wavelengths of the resonance dips for decreasing values of strain are also plotted. Resonance shift $\partial\lambda_m/\partial S_z$ is obtained from a linear fit.

Similar to Eq. (5.13) in the more general Sec. 3.3.2, we indicate the effects of the different phenomena in Eq. (3.10)

$$\frac{\partial\lambda_m}{\partial S_z} = \underbrace{\frac{n_s}{\langle n_g\rangle}}_{\text{dispersion}} \Big(\underbrace{\frac{\lambda_c}{n_s}\frac{\partial n_s}{\partial S_z}}_{\text{eff. index}} + \underbrace{\lambda_c}_{\text{track-length}} \Big). \tag{3.13}$$

This result is used in the interpretation of the measurements in Sec. 3.6. In fact, track-averaged group index $\langle n_g\rangle$ can be approximated as the group index n_g of the straight waveguide. We have used the numerical mode solver to show that this approximation is valid within 1%. In our analysis, we use the track-averaged group index which was accurately measured.

3.4 Methodology

We characterized the photonic chips in an automated setup in which they are bent such that the top layer with the racetrack resonators is strained. Transmission spectra of the resonators were recorded for elongations varying from 0 to 275 microstrain. As example, Figure 3.2a shows a resonance dip of the measured spectra for increasing strain. The resonance wavelengths, and the group index n_g, were extracted from fitting a relation for ring resonator transmission. Figure 3.2b shows the resonance wavelength λ_m plotted versus the applied strain.

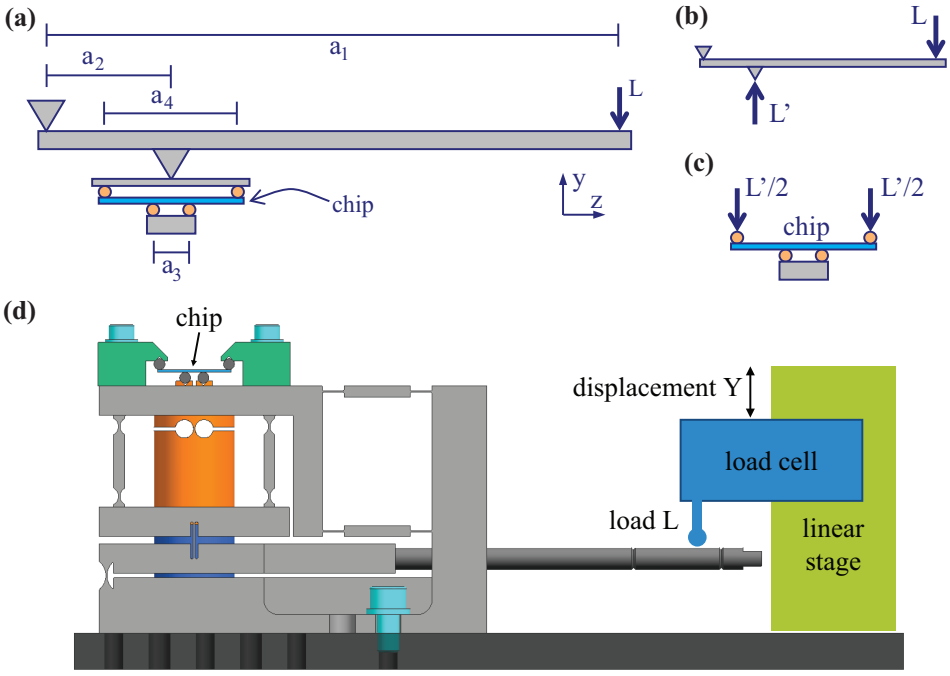

Figure 3.3: **(a-c)** Analysis of the mechanical setup. **(d)** Sketch of the mechanical setup. Composed of the CAD drawing that was used to fabricate the setup (left-hand-side), and a sketch of the linear stage with the load cell (right-hand-side).

3.4.1 Mechanical setup: four point bending

We designed and fabricated a mechanical setup in which the chips are bent such that the top layer with the photonic circuit is uniformly strained (Fig. 3.3). The setup is equipped with elastic elements to provide an accurate bending moment to the chip, without hysteresis or other non-linearities. Between the two inner supports, the chip experiences a constant bending moment M (known as *pure bending*) [42]

$$M = \frac{a_1(a_4 - a_3)}{4a_2} L, \tag{3.14}$$

with L the load applied at the lever. The bending of the chip is described by plate bending theory for *thin plates with small deflections* [43], as its thickness H is small compared to its width W and length. An assumption in this theory is that the normal stresses in the x-direction can be neglected, so that there is no strain S_x in the x-direction and the width W of the chip does not change due to the applied load. In the setup, the deflection of the chip at considerable distance from its ends can be assumed to be cylindrical. In this mechanical analysis the influence of upper layers of the chip (BOX layer, waveguide layer, and cladding layer) is neglected as their total thickness of 4.220 μm is much smaller than the

chip thickness of 675 μm. Hooke's law and plate bending theory give the relation between the stress σ_z and strain S_z in the chip [41, 43]:

$$\sigma_z = \frac{E_z}{1 - \nu_{xz}\nu_{zx}} S_z, \tag{3.15}$$

with Young's modulus[1] E_z and anisotropic Poisson's ratios[2] ν_{xz} and ν_{zx}. Combining Eqs. (3.14) and (3.15) with the cylindrical deflection of the chip gives the strain S_z on the top surface of the chip in the mechanical setup

$$S_z = \frac{3a_1(a_4 - a_3)(1 - \nu_{xz}\nu_{zx})}{2a_2 W H^2 E_z} L. \tag{3.16}$$

A precise linear stage (Newport MFA-CC) applies a force to the lever, while a load cell (Omega LECB5) measures the actual applied load L. It was observed that the relation between the displacement of the linear stage Y and the applied load L is linear in the regime of our measurements, and also that the repeatability of the linear stage position Y was higher than the repeatability of the load cell. Therefore, we extracted a single number for the resistance of the chip to bending, $\partial Y/\partial L$, from all the measurements performed on a chip.

3.4.2 Optical setup

The transmission spectra of the racetracks were measured with near infrared light around $\lambda_c = 1550$ nm. An amplified spontaneous emission light-source (OptoLink C-band ASE) was used to emit this light, and a 5 nm span of the spectra were recorded with an optical spectrum analyzer (Yokogawa AQ6370B). The input and output waveguides of the racetrack resonators are routed to out-of-plane grating couplers at convenient locations on the chip, and coupled to cleaved optical fibers via free-space [44, 45]. These fibers were mounted on stages with piezo positioning, and automatically actively aligned in the horizontal (x,z)-plane before recording a spectrum. All transmission spectra are normalized to the transmission spectrum of a reference waveguide, which was smoothened by convolution with a 1 nm wide Gaussian window to remove Fabry-Pérot resonances originating from reflections of the out-of-plane grating couplers.
A relation for ring resonator transmittance, Eqs. (3.1)-(3.4), was fitted to the recorded spectrum. The ring length l and straight-through power of the coupler $|t|^2 = 41\%$ were fixed, while the effective index $\langle n_e \rangle$, group index $\langle n_g \rangle$, resonator waveguide loss α^2 and fiber-coupling loss were fitted. The resolution bandwidth of the optical spectrum analyzer (OSA) was incorporated in this fitting by convoluting the calculated spectrum with a 20 pm wide Gaussian curve. For the zero-strain measurement, the mode number m of the resonance closest to λ_c was estimated from Eq. (5.12) where the effective index $n_e(\rho, \lambda_c, 0)$ was calculated using a mode solver (film mode matching method in FimmWave by PhotonDesign [46]). This dip was followed over consecutive measurements. An accurate initial guess of $\langle n_e \rangle$ and

[1] E_i is the Young's modulus along axis i.
[2] ν_{ij} is the Poisson's ratio that corresponds to a contraction in direction j when an extension is applied in direction i.

$\langle n_g \rangle$ (thus the wavelengths of the resonance dips) is necessary for the Levenberg-Marquardt fitting algorithm [47]. Therefore, the resonance dips were first found using *findpeaks* [48] and from this $\langle n_e \rangle$ and $\langle n_g \rangle$ were estimated via Eq. (5.12). This initial estimate allows for automated fitting of the spectra. With this fitting, the free parameters in Eqs. (3.1)-(3.4) could be obtained, and λ_m was calculated from Eq. (5.12) with an accuracy much higher than the resolution bandwidth of the OSA.

3.4.3 Measurements

We characterized chips with the racetracks in the <110> crystalline direction and with the racetracks in the <100> direction. The measurements were repeated several times. First, the chip was manually placed in the setup. Then resonators with different widths of the straight waveguide were automatically measured. The strain of the racetrack was increased and decreased from 0 to approximately 275 microstrain, with 6 steps in each direction (see Fig. 3.2a). The transmittance spectrum was recorded for each applied strain, and the resonance position λ_m that started closest to λ_c was extracted. The effective group index $\langle n_g \rangle$ was also extracted from this spectrum. For each value of applied strain, the measured load L and the position of the linear stage Y were recorded. Per measurement set of increasing and decreasing strain, the resonance shift per displacement of the load cell, $\partial\lambda_m/\partial Y$, was obtained from a linear fit, and so was the relation between the displacement and the applied load, $\partial Y/\partial L$. We observed that both relations were indeed linear in this regime. The strain-induced resonance shift is then

$$\frac{\partial \lambda_m}{\partial S_z} = \frac{\partial \lambda_m}{\partial Y} \cdot \frac{\partial Y}{\partial L} \cdot \frac{\partial L}{\partial S_z}, \tag{3.17}$$

in which the first two terms on the right-hand-side are measured and the last term is calculated from Eq. (3.16).
The relation between the displacement of the load cell and the measured load can be interpreted as the resistance of the chip and setup to bending. The average value for the chip with the racetracks in the <110> direction is $\partial Y/\partial L = 0.128$ μm/mN and the average value for the chip with the racetracks in the <100> direction $\partial Y/\partial L = 0.135$ μm/mN.

3.4.4 Numerical mode solver

For the analysis of the measurements, we calculated the effective index at zero strain, $n_e(\rho, \lambda_c, 0)$ using the film mode matching method in FimmWave [46]. Also the effective group index $n_g(\rho)$ at λ_c was calculated using this mode solver. The track-averaged effective index $\langle n_e \rangle$ and group index $\langle n_g \rangle$ are then straightforward to calculate.

3.4.5 Measurement uncertainty analysis

The uncertainty in the measurements was estimated following the guidelines of Ref. [49]. The relative errors of the three terms on the right-hand-side of Eq. (3.17)

Table 3.1: Material properties, dimensions, and estimated uncertainties of mechanical setup

Quantity	Value	Uncertainty	
$E_z/(1-\nu_{xz}\nu_{zx})$, <110>	170 GPa[a]	4 GPa	2.5%[b]
$E_z/(1-\nu_{xz}\nu_{zx})$, <100>	141 GPa[a]	4 GPa	2.5%[b]
a_1	156 mm	0.3 mm	0.2%[c]
a_2	24 mm	0.03 mm	0.1%[d]
a_3	5 mm	0.03 mm	0.6%[d]
a_4	20 mm	0.03 mm	0.1%[d]
Chip W	24 mm	0.3 mm	1.2%[c]
Chip H	0.675 mm	0.01 mm	1.7%[e]
$\partial L/\partial S_z$, <110>	12.7 mN/μstrain	0.6 mN/μstrain	4.7%
$\partial L/\partial S_z$, <100>	10.5 mN/μstrain	0.5 mN/μstrain	4.7%

[a] From Ref. [41]
[b] Estimated.
[c] Measured with digital electronic calipers, maximum error 0.5 mm.
[d] Estimated fabrication uncertainty, maximum error 0.05 mm.
[e] Measured with digital electronic calipers, maximum error 0.02 mm.

are added quadratically, as they are independent. The chips with the racetrack resonators in the <110> and <100> directions were placed in the mechanical setup and measured 6 and 5 times, respectively.

$\partial\lambda_m/\partial Y$

The value for $\partial\lambda_m/\partial Y$ is averaged over the repetitive measurements, and the uncertainty is estimated as the standard deviation. The relative uncertainty did not significantly depend on the width of the waveguide, and the maximum relative uncertainty (of all widths) is used. The uncertainty for the chips with the waveguides in the <110> and <100> directions are 3.1% and 1.1%, respectively. The measurement-to-measurement difference mainly originated from repositioning the chip in the setup, which was done before each measurement. Repeating a measurement without repositioning the chip in the setup gives a measurement-to-measurement difference which is negligible. We could not attribute this difference to a slight tilt of the chip with respect to the setup (around the y-direction). We do not fully understand why the uncertainty in the <110> direction is higher, but the strong angle dependency of Poisson's ratio around the <110> direction may play a role. Also, we had to reassemble the setup between various <110> measurements, while the measurements of the <100> chip were performed consecutively in a mainly empty laboratory.

$\partial Y/\partial L$

The value of $\partial Y/\partial L$ did not significantly depend on the position of the chip in the setup. All measurements (for different widths of the waveguide, and repetitions of the measurements) are averaged to obtain $\partial Y/\partial L$. The statistical uncertainty (arising from random fluctuations) is estimated as the standard deviation, and the systematic uncertainty of the system (load cell, load cell voltage source, and A/D converter) is estimated as 3%. The standard deviation of the 30 measurements in the <110> direction is 2.8%, and the standard deviation of the 45 measurements in the <100> direction is 0.7%. This difference can be explained by the fact that we increased the integration time of the read-out of the load cell from 50 samples at 1 kHz for the <100> direction measurements to 1000 samples at 1 kHz for the <110> direction measurements. The output voltage of the load cell is a few mV, which required this longer integration time of our A/D converter (National Instruments USB-6251 DAQ). The uncertainties of $\partial Y/\partial L$ are thus 5.8% and 3.7% for the chips with the racetracks in the <110> and <100> directions, respectively.

$\partial L/\partial S_z$

The mechanics of the setup is described by Eq. (3.16). The material properties, dimensions, and uncertainties that are used in this equation are listed in Table 3.1. The uncertainty σ of a quantity whose uncertainty is estimated as a maximum deviation u is given by $\sigma = u/\sqrt{3}$ [49]. In the computation of the uncertainty of $\partial L/\partial S_z$, we have treated all uncertainties as independent and approximated the influence of all the uncertainties as linear.

Group index $\langle n_g \rangle$

We found that the track-averaged effective group index does not depend on the applied strain. Therefore all measurements of a device are averaged, and the uncertainty is estimated as the standard deviation. These where 78 and 65 measurements for the racetracks in the <110> direction and <100> directions, respectively. The relative uncertainty did not depend much on the width of the straight waveguide in the racetrack nor on the crystalline orientation, so that we have used the maximum of 0.03%.

Effective index $\langle n_e \rangle$

In the analysis of the measurements, we calculated the effective index with a numerical mode solver. We do not know the uncertainty, as it is mostly related to the difference between the simulated waveguide and the fabricated waveguide. Therefore, we estimated the uncertainty in the effective index as the difference between the measured effective group index $\langle n_g \rangle$ and the track-averaged group index as calculated with the same mode solver (see Fig. 3.4b).

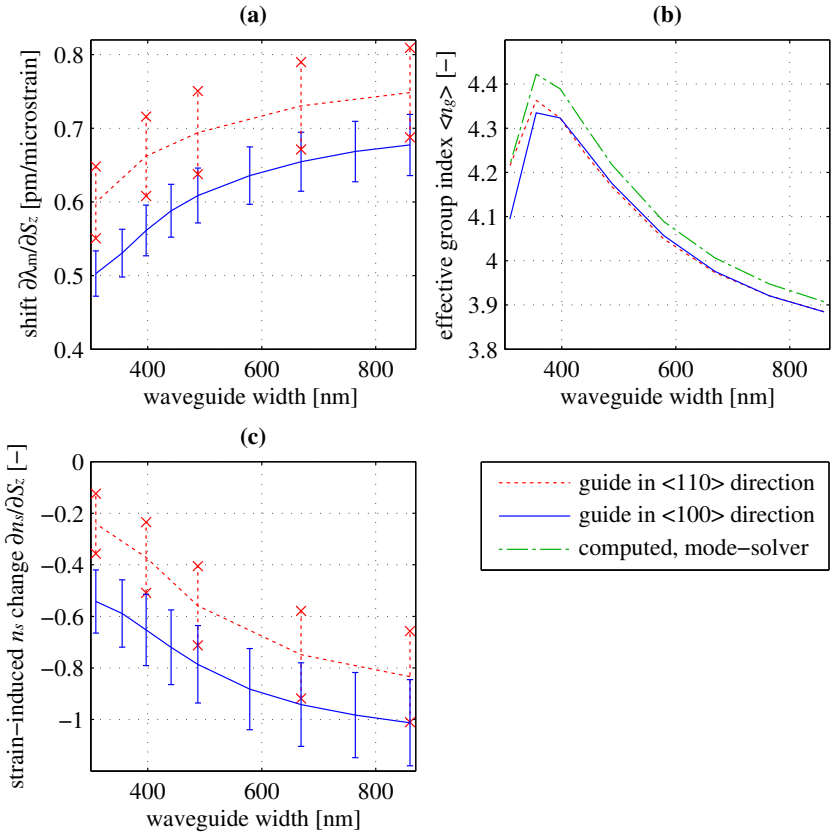

Figure 3.4: **(a)** Measured resonance shift per applied strain $\partial\lambda_m/\partial S_z$, with resonance wavelength λ_m and strain S_z. **(b)** Measured and calculated track-averaged effective group indices $\langle n_g \rangle$. Measured for racetracks in the <100> and in the <100> silicon crystalline directions. **(c)** Change in effective index of a straight waveguide, n_s, due to a strain, S_z, applied in the direction of the guide.

3.5 Characterization

We characterized two chips with long racetrack resonators; one chip with the resonators in the <110> silicon crystalline direction and one with the resonators in the <100> direction. A strain S_z was applied to the top surface of the chips, where the resonators are placed. The strain was increased to approximately 275 microstrain, and then decreased to zero strain in steps of approximately 45 microstrain. Per applied strain, the transmission spectrum of the resonator was recorded, as is shown in Figure 3.2a. The wavelength of the resonance dip which started closest to 1550 nm is extracted from each of the spectra, and plotted versus the applied strain in Figure 3.2b. The shift per applied strain $\partial\lambda_m/\partial S_z$ is obtained from a linear fit. This is done for racetracks with different widths, and the resonance shifts per strain are presented in Figure 3.4a. It can be seen that the racetracks in the <110> direction are slightly more sensitive than the tracks in the <100> direction, and that the resonators with wider waveguides are more sensitive to strain than the ones with narrower waveguides widths. The latter can be attributed to the dispersion in the waveguide, as shown in Sec. 3.6. The estimated uncertainties are with respect to the absolute value of λ_m/S_z, and a large part of the uncertainty is a systematic bias and equal for all measurements. Considering only the statistical (or random) uncertainties, we found that the racetracks in the <110> and <100> directions have a significantly different shift in resonance.
The track-averaged effective group indices $\langle n_g \rangle$ were also extracted from the spectra and are presented in Figure 3.4b. We also calculated the effective group index with the numerical mode solver. The calculated and measured track-averaged effective group indices agree within 3%.
The change in effective index due to strain, $\partial n_e/\partial S_z$, is calculated using Eq. (3.10). We measured the resonance shift $\partial\lambda_m/\partial S_z$ and the effective group index $\langle n_g \rangle$, and we calculated the effective index n_s of the straight waveguide with the numerical mode solver. The resulting $\partial n_s/\partial S_z$ is shown in Figure 3.4c.

3.6 Analysis

In this section, we interpret the measured shift and indicate the contributions of different physical effects: the elongation of the track, the change in effective index and the dispersion of the waveguide. Equation (3.13) shows how these effects shift the resonance wavelength. The effect of the elongation of the track (λ_c) and the effect of the change in effective index are added. The change in effective index $\partial n_s/\partial S_z$ is negative, so the two effects oppose each other. The dispersion of the waveguide, n_s/n_g, is smaller than unity, and thus damps the shift. Figure 3.5a presents $n_s/\langle n_g \rangle$, in which it can be seen that this damping is stronger for small waveguides. Figure 3.5b presents the resonance wavelength shift with dispersion excluded. The shift due to the change in the effective index increases (in magnitude) with increasing width of the guide. The higher resonance shift for wider waveguides $\partial\lambda_m/\partial S_z$ is thus due to the dispersion, and not due to the change in effective index of the waveguide.

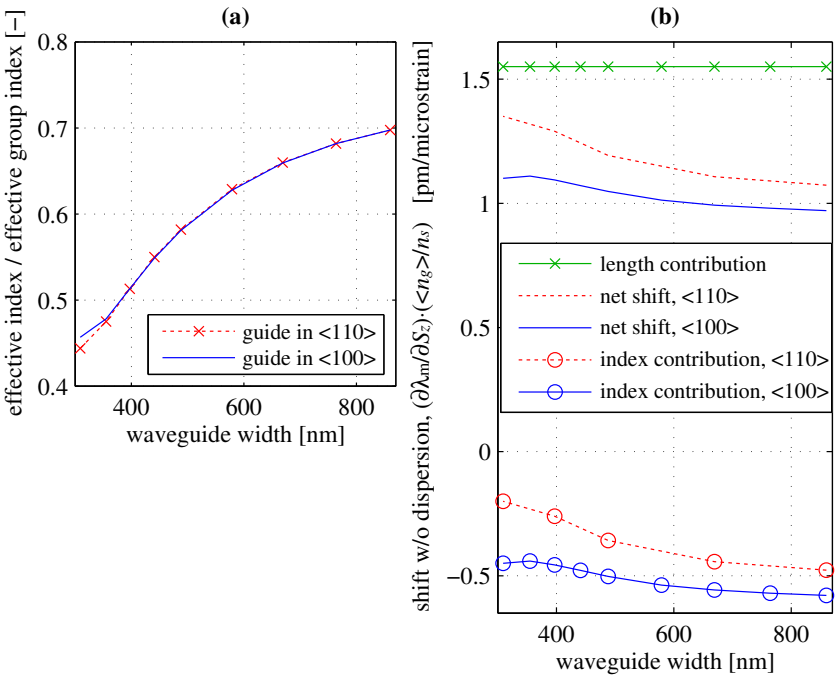

Figure 3.5: (a) Influence of dispersion on the strain-induced resonance shift, $n_s/\langle n_g \rangle$. Effective index n_s is calculated with a mode solver. Track-averaged effective group index $\langle n_g \rangle$ is measured. **(b)** The hypothetical strain-induced shift in resonance in which the dispersion is excluded. The two different contributions to this shift (track-length change and effective-index change) are shown. Results for the racetracks in the <110> and the <100> directions are shown

3.7 Conclusion

We measured the strain-induced shift of the resonances of optical racetrack resonators in silicon-on-insulator technology. For waveguides with a width of 400 nm, the resonance wavelength shift per applied strain is 0.57 pm/microstrain when the racetrack is parallel to the ⟨100⟩-direction of the silicon crystal, and 0.66 pm/microstrain when the racetrack is parallel to the ⟨110⟩-direction. We observed largest sensitivity for wider waveguides; a racetrack with 860 nm wide waveguides oriented in the ⟨110⟩-direction has a resonance shift of 0.75 pm/microstrain. We have studied elongations up to 275 microstrain, and observed a linear relation between the resonance wavelength and the applied strain.

The effect of the strain-induced increase in track circumference and the effect of the strain-induced change in waveguide effective index oppose each other. The effect of the strain-induced increase in circumference is about three times larger than the effect of the change in effective index. The strong dispersion in the sub-wavelength silicon waveguides lowers the change in wavelength shift approximately by a factor two. In fact, the lower dispersion of the wider waveguides is the reason that these devices are more sensitive.

This chapter addressed how micro-ring resonators transduce an applied strain into a shift of their optical resonance wavelengths. Sensor MEMS or MOEMS consist, next to the transducer, also of a mechanical structure that acts on the transducer and an interrogation system that reads the transducer. A variety of interrogation concepts exist for monitoring the shift in the resonances of optical resonators [50–56]. The detection limit of MOEMS sensors depends on the designs of the mechanical structure and the interrogation system. These designs are application specific as they depend, for example, on the bandwidth of the measured signal (e.g., Ref. [33] presents the design of an ultrasound sensor).
In this work, we have characterized a novel type of optical strain sensors which can be integrated in micro-electro-mechanical systems (MEMS). We believe these sensors open opportunities in different fields of applications such as in the medical, petrochemical, or oil&gas markets, by offering specific advantages such as high-speed readout over kilometer distances, integrated optical multiplexing, and small device size. Moreover, by removing the need for galvanic connections, susceptibility to electromagnetic disturbance is eliminated.

Chapter

4

Proof of concept of an optical micromachined ultrasound sensor

Abstract – With the increasing use of ultrasonography, especially in medical imaging, novel fabrication techniques together with novel sensor designs are needed to meet the requirements for future applications like three-dimensional intercardiac and intravascular imaging. These applications require arrays of many small elements to selectively record the sound waves coming from a certain direction. Here we present proof of concept of an optical micro-machined ultrasound sensor (OMUS) fabricated with a semi-industrial CMOS fabrication line. The sensor is based on integrated photonics, which allows for elements with small spatial footprint. We demonstrate that the first prototype is already capable of detecting pressures of 0.4 Pa, which matches the performance of the state of the art piezoelectric transducers while having a 65 times smaller spatial footprint. The sensor is compatible with MRI due to the lack of electronical wiring. Another important benefit of the use of integrated photonics is the easy interrogation of an array of elements. Hence, in future designs only two optical fibers are needed to interrogate an entire array, which minimizes the amount of connections of smart catheters. The demonstrated OMUS has potential applications in medical ultrasound imaging, non destructive testing as well as in flow sensing.

This chapter is based on the following publication:

S. M. Leinders, W. J. Westerveld, J. Pozo, P. L. M. J. van Neer, B. Snyder, P. O'Brien, H. P. Urbach, N. de Jong, and M. D. Verweij, "A sensitive optical micro-machined ultrasound sensor (OMUS) based on a silicon photonic ring resonator on an acoustical membrane," in *Scientific Reports*, vol.5, 2015

4.1 Introduction

The wide use of ultrasonography, especially in medical imaging, has resulted in the development of different types of ultrasound transducers such as piezo-electric transducers, micro-machined ultrasound transducers (MUTs) and optical ultrasound sensors. Conventional transducers are made of piezo-electric material and nowadays contain multiple piezo elements to form a one or two dimensional array. These arrays enable beam focusing and steering, and hence are able to scan the area or volume of interest and create real-time 2D or 3D images [1, 2]. The frequencies of the transducers are ranging from 1-20 MHz and typical bandwidths are 70-80% [57]. Recently, Xia *et al.* [58] presented a piezo-electric array of 5 mm $\times$ 5 mm containing 25 elements of 0.9 mm $\times$ 0.9 mm. This ultrasound array transducer is used in photoacoustic breast tomography and has a center frequency of 0.9 MHz and a bandwidth of 80%. The noise equivalent pressure is 0.5 Pa per single element. We shall use this element as reference to our sensor.

Because small diagnostic transducers are paramount for extending the possibilities of intravascular and transesophageal ultrasound, one of the goals in the development of piezo-electric transducers is miniaturization [1]. There are two main challenges in the fabrication of small arrays. The first challenge is to obtain the small elements. The conventional fabrication technique uses a diamond saw to divide a single piezo-electric slab into multiple elements [1]. The minimal distance between two neighboring elements is determined by the thickness of the dicing blade (minimal $\sim$10-15 μm), and advanced fabrication techniques like laser cutting are required when this distance should be decreased.

The second issue is related to the individual wiring of the elements, especially when a large number (order of thousands) of elements is needed [59–61]. Bonding techniques, in which wires are attached to each individual element, are too labor-intensive for arrays containing large amounts of elements. Hence, the use of flexible circuits or other complex techniques are required for the electrical interconnections. Moreover, dense electrical wiring generally brings the disadvantage of intrinsic susceptibility to electromagnetic interference and cross-talk [59, 61].

The mentioned production difficulties make that increasing miniaturization of conventional piezo-electric transducer arrays is intricate. To circumvent these difficulties, capacitive and piezo-electric micro-machined ultrasound sensors (CMUTs and PMUTs) are developed [62–64]. A MUT consists of a flexible membrane that is deformable by ultrasonic pressure waves. The micro-machining technology used for the fabrication of MUTs benefits from the developments in the integrated circuit (IC) technology, which allows for a relatively easy fabrication of complex transducer patterns, as well as the integration of accompanying electronic circuitry [65, 66]. However, these MUTs still have a high electrical impedance resulting in a low signal-to-noise ratio and, consequently, a low imaging depth. To obtain the imaging depth that is currently attained with piezo-electric arrays, the signal-to-noise ratio of MUTs should be improved [57, 63].

As far as the receive function is concerned, optical micro-sensors are another alternative for conventional piezo-electric transducers [67, 68]. These optical devices share the fabrication benefits of MUTs. An additional benefit of these

sensors is the lack of electrical wiring or matching circuits. The insensitiveness to electromagnetic interference makes optical devices also compatible with imaging systems such as MRI. In contrast to the previously described electrical transducers, optical devices are not reciprocal and require an external ultrasound source to transmit the sound waves. Ultrasonic optical fiber sensors are commercially available [69, 70]. However, planar optical circuits are needed to build a dense one or two dimensional array of ultrasound sensors. The group of Guo have reported on sensors that are based on a polymer ring resonator [67, 71, 72]. They manufactured a one dimensional array of four polymer micro-ring resonators (100 μm diameter) [72]. Their latest sensor has a noise-equivalent pressure (NEP) of 10.5 Pa for a bandwidth of 1-25 MHz [67]. The fabrication of these polymer photonic integrated circuits is performed with special polymer technology. Rosenthal *et al.* [73] fabricated optical ultrasound sensors in silicon, using standard silicon IC fabrication technology (CMOS). They reported on a sensor in silicon-on-insulator technology, based on the deformation of a π-phase-shift fiber Bragg grating (π-FBG) with a length of 250 μm. Currently, the optical modulation in this embedded ultrasound sensor is predominantly caused by the formation of surface acoustic waves. The sensor only has a response to incident pressure waves with an angle larger than 19° to the normal and can therefore not be used for diagnostic ultrasound, which has near normal incidence. Unlike CMUTs and PMUTs, neither of the optical sensors above employ a membrane.
Appreciating the mentioned benefits of both integrated optical sensors and micromachining technology, we fabricated a 'receiver-only' optical micro-machined ultrasound transducer (OMUS) with a membrane. In doing so we improved the sensitivity by a at least an order of magnitude. Our OMUS contains an optical micro-ring resonator that is integrated onto an acoustical membrane in a silicon chip. We are, to the best of our knowledge, the first to report the operation of such a sensor for ultrasonic frequencies. Photonic integrated circuits in silicon-on-insulator (SOI) technology have a high contrast in refractive index. Therefore, silicon micro-ring resonators can have diameters down to 5 μm without substantial radiation losses [74]. The small spatial footprint of integrated waveguides opens up the possibility to make sensors with sizes in the order of 10 μm, which is an order of magnitude smaller than the current state of the art. Moreover, it allows the addition of small passive optical multiplexers for the simultaneous read-out of many elements [75, 76]. Hence, the read-out of an entire array of elements can in principle be done with only two optical fibers.
In this chapter, we present the measurements of the performance of this novel type of OMUS and show the possibilities of this device as an ultrasound sensor, especially for medical applications.

4.2 Concept, design and fabrication

The OMUS consists of a waveguide and a photonic ring resonator that are integrated onto a membrane (Fig. 4.1a). When a broad spectrum of light is trans-

mitted through the waveguide, a part of the spectrum is coupled into the ring resonator by means of a directional coupler [77]. The transmitted spectrum at the output port of the waveguide shows dips at the optical resonance wavelengths λ_m of the ring resonator, given by

$$m\lambda_m = n_e l, \tag{4.1}$$

where m is an integer number, l the circumference of the ring and n_e its effective index of refraction. Incident acoustical pressure waves strain the membrane and hence the resonator. The induced strain in the resonator causes a shift in the optical resonance curves with respect to the undeformed state. The magnitude of this shift due to induced strain depends on three aspects: the amount of elongation of the optical resonator track, the change in effective index of refraction, and the change in dispersion of the material of the track [21, 78]. The shift in resonance is what we want to observe. To do so without using a dedicated detector, we transmit light, and hence measure the transmitted intensity, at one optical wavelength. This wavelength is chosen on one flank of the optical resonance curve of the undeformed resonator, such that a shift of the resonance curve directly translates into a modulation of the transmitted optical intensity, as is shown in Figure 4.1b. The intensity is measured using a photo diode.

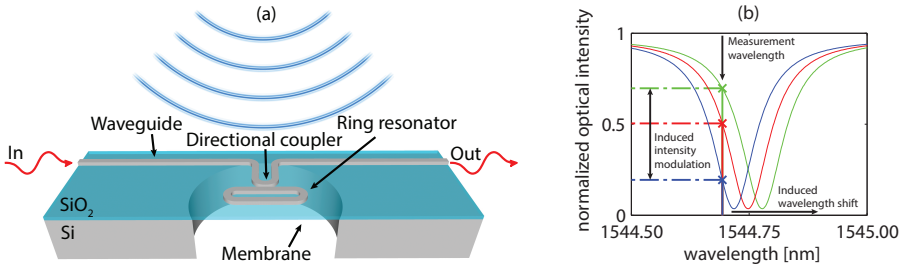

Figure 4.1: a) Sketch of the OMUS, showing the photonic micro-ring resonator on top of the membrane. b) Sketch of three intensity curves at the end of the waveguide, representing the different transmittances for different strain values of the photonic micro-ring resonator.

The design of the membrane is chosen such that it has a resonance frequency around 1 MHz. To determine the dimensions we use plate bending theory, because the deflection of the membrane is expected to be small compared to its height [79]. With this theory the resonance frequency of the freely moving membrane can be calculated analytically for specific boundary conditions. However, for medical diagnostic purposes the sensor will be submerged in water-like substances, and the predicted resonance frequency in air will shift downwards [20]. Therefore, we use a finite element method (COMSOL Multiphysics) to numerically determine the diameter and thickness of the membrane [80] that will give the desired resonance frequency. The membrane of the OMUS was designed as a 2.7 μm thick silicon

oxide slab with a diameter of 120 μm. It was created by taking silicon with a top layer of silicon dioxide, and etching a hole through the back of the silicon. To ensure a flat bottom surface of the membrane and a reproducible fabrication, all the silicon behind the membrane was etched. The dimensions of the waveguides and directional coupler determine the shape of the optical resonance dips. The shape of the ring resonator and its position on the membrane determine the shift in optical wavelength due to the deformation of the membrane. The steeper the flank of the optical resonances, the more sensitive the sensor. An optimization problem now arises, in that a long racetrack has a narrower resonance dip and therefore a higher sensitivity. However, the strain patterns of a statically deformed membrane showed that a short ring resonator located in the middle of the membrane results in the most strain per pressure. Based on the mechanical FEM analysis and the model in Ref [77], we chose a racetrack-shaped optical ring-resonator with a bending radius of 5 μm and 40 μm straight track. We use two directional couplers on opposite sides of the ring resonator with a 6 % coupling efficiency of optical power. For details on the design, we refer the reader to our previous work [10,81]. We use an out-of-plane grating coupler at each end of the waveguide to direct the light upwards out of the waveguides and into optical fibers.
We realized the sensor using the following procedure. First, the fine optical circuitry was fabricated using a semi-industrial CMOS fabrication line at IMEC (Leuven, Belgium) via the ePIXfab platform [82]. The resulting wafer-piece (die) contains 220 nm high and 400 nm wide silicon waveguides on top of a 2 μm thick silicon-dioxide layer on a 250 μm thick silicon substrate. A 0.5 μm thick silicon-dioxide cladding was deposited to isolate the waveguide from the water. Second, we etched the membrane (124 μm diameter) from the back of the die using deep reactive ion etching with sulfur hexafluoride (SF_6) as etchant and we used the silicon-dioxide layer as a well-defined etch-stop. A photograph of the membrane with photonic circuitry is shown in Fig 4.2. Third, we glued the chips on two 1 mm thick glass plates. The first plate contained a hole of 4 mm diameter, which was positioned behind the membrane. The second glass plate sealed the chip from the backside, ensuring that only air is present behind the membrane. Finally, we connected the optical fibers to the silicon photonic circuit, referred to as packaging. We developed a packaging method that is suitable for under-water usage. This involves attaching to the chip a Pyrex block in which the connecting optical fiber ended. The block had a polished angle facet with an evaporated aluminum coating to reflect light from the fiber into the grating coupler at the end of the waveguide [83].

4.3 Results

We have optically characterized the OMUS by measuring the transmittance of light. Moreover we performed acoustical measurements to measure the time responses to transmitted acoustical pulses with different frequencies. Finally we determined the bandwidth, sensitivity and noise equivalent pressure of the sensor.
The optical characterization starts by determining the shape of the optical reso-

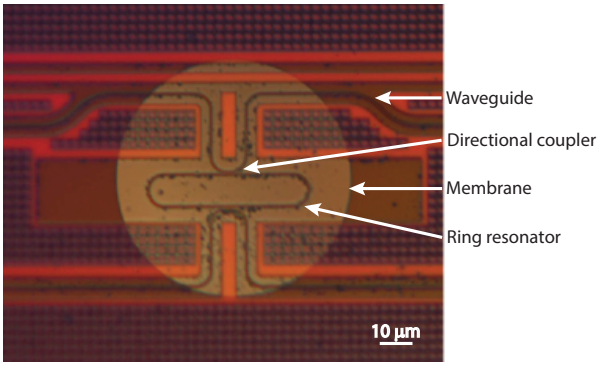

Figure 4.2: Microscopic image of an OMUS, showing a membrane with an optical resonator and two directional couplers. This OMUS has a circular membrane with a diameter of 78 μm and a thickness of 2.7 μm. The membrane is visible because it is illuminated from the back. The OMUS reported in this chapter has a larger membrane diameter of 124 μm.

nance curve of the ring resonator in a static situation, hence without deformation of the membrane. We measured the transmission $T(\lambda)$ from the input to the output of the OMUS by stepping through successive optical wavelengths. The intensity I at the output of the chip for a static situation is given by $I = T\,I_0$ with I_0 the maximum output intensity far away from the resonance dip. This is directly related to the maximum output power P_0, which currently is 10 μW (Fig 4.3a). The transmittance of the OMUS shows a dip at resonance of the ring resonator which has a FWHM of 100 pm. The transmittance of a membrane at rest is denoted by T_0 and is the initial transmittance of every acoustical measurement. When the membrane and hence the optical resonator is deformed, the transmittance of the ring resonator is shifted. We write the deformed transmittance $T(\lambda)$ in first order as $T(\lambda) \approx T_0(\lambda + \Delta\lambda)$, where $\Delta\lambda$ is the wavelength shift due to the deformation of the ring (see Fig 5.1b).
For the acoustical measurements we observe the time modulation of the output intensity at one particular optical wavelength λ_l set by the laser (indicated as measurement wavelength in Fig 5.1b). When an incident acoustical wave deforms the membrane and hence the resonator over time, the time dependent intensity at the output of the chip can be described as

$$I(\lambda_l, t) = T(\lambda_l) I_0 \approx T_0\left(\lambda_l + \Delta\lambda(t)\right) I_0, \tag{4.2}$$

with $\Delta\lambda(t)$ the ultrasound-induced optical wavelength shift. When we interrogate by measuring the intensity at one particular optical wavelength over time, the sensitivity of interrogation is determined by the gradient of the initial transmittance curve and hence is the largest when the measurement wavelength λ_l is at the point of largest gradient of the transmittance. To show this dependence, we applied an acoustical wave (described in section Materials and Methods) and measured the maximal output intensity swing versus the chosen measurement wavelength. The result is shown in Figure 4.3b (blue line). The curve shows equal sensitivity be-

tween the left and right side of the optical resonance dip (dashed black line) as is expected by the symmetry of the resonance dip. The maximal sensitivity is reached at around 1/3 from the bottom of the dip. We also determined the noise versus the chosen optical wavelength (red line) by measuring the intensity fluctuations in the absence of an incident acoustical wave. As is shown in the figure, the noise depends only slightly on the output intensity (dashed black line). Therefore, the signal-to-noise-ratio will mainly depend on the sensitivity curve. For every measurement we will hence use the optical wavelength that gives a maximal output intensity swing; this will be chosen on the left flank.

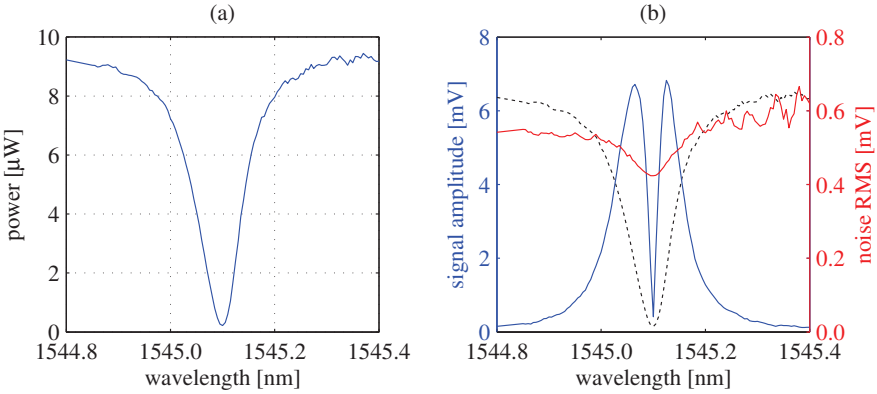

Figure 4.3: a) The measured transmittance versus optical wavelength, for a maximum output power P_0 of 10 μW. b) The measured output intensity swing of the OMUS (blue line), the RMS value of the noise in the output intensity (red line), and the transmittance (dashed black line; normalized for visibility), all versus the chosen optical wavelength of the laser.

After we determined a suitable optical wavelength for our measurements, we investigated the response of the OMUS to an acoustical Gaussian modulated sine wave (see Section Materials and Methods), being transmitted by an external ultrasound source. Two measured time traces of the output signal due to an incident acoustical wave are shown in Fig 4.4. The presented signals are an average of 500 individual signals. The upper time trace shows the response to a transmitted acoustical wave with a 0.42 MHz center frequency, which is below the acoustical resonance peak of the membrane. The second time trace shows the response to a transmitted acoustical wave around the resonance frequency of the membrane (f_0 = 0.77 MHz). The signal below the resonance frequency of the membrane resembles the transmitted acoustical pulse quite well, while there is a large acoustical ring-down time present in the signal around the acoustical resonance frequency of the OMUS.

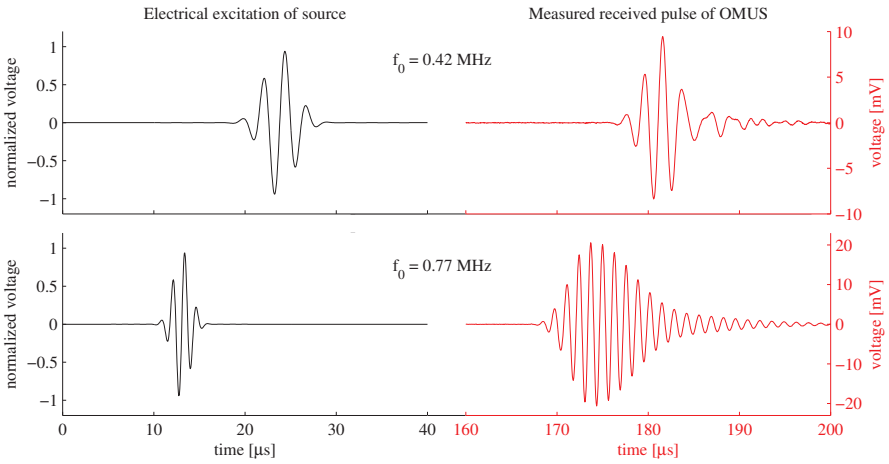

Figure 4.4: Time responses of the OMUS (right, red) for two transmitted acoustical pulses (left, black) with different center frequencies. The presented signals are an average of 500 individual signals.

The normalized transfer function of the OMUS is shown in Fig 4.5 and is obtained by sweeping the ultrasound frequency from 0.4 MHz to 1.4 MHz using narrow-band pulses. The -6 dB bandwidth of the OMUS is 19% and the center frequency is 0.76 MHz. The used maximum output power P_0 for these and subsequent measurements was 70 μW.

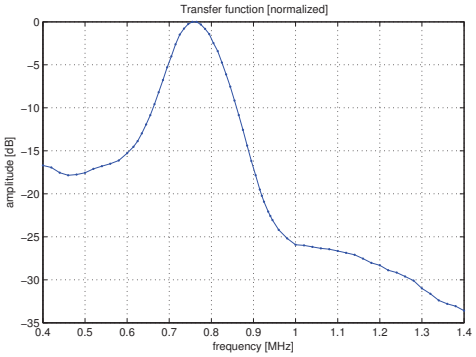

Figure 4.5: The normalized transfer function of the OMUS.

We determined the sensitivity and noise equivalent pressure of the OMUS for incident acoustic waves with a frequency that corresponds to the maximum of the transfer function (f_0 = 0.76 MHz). The measurement results are shown in Fig 4.6 which shows the amplitude of the detected signals versus the amplitude of the

exciting acoustical signal. For small deformations of the membrane, and hence for small optical wavelength shifts of the optical resonance, the sensor response is linear. The OMUS has a sensitivity of 2.1 mV/Pa for pressures up till approximately 150 Pa (determined with a linear fit). For higher pressures, the sensitivity curve starts to deviate from a linear behavior. This nonlinear response of the OMUS occurs because of the used detection system. With this system the dynamic range of the OMUS is determined by the width of the optical resonance curve. If the deformation of the membrane, and hence the shift in optical resonance is too large, the response of the OMUS is distorted. We determined a noise equivalent pressure (NEP) of 0.4 Pa by the intersection of the sensitivity curve and the RMS value of the measured output noise (0.8 mV). To transform the NEP value to an equivalent minimum detectable wavelength shift we use the derivative of equation (4.2) with respect to the wavelength. The minimum detectable wavelength shift $\Delta\lambda_{\text{noise}}$ is thus calculated from the RMS noise ΔI_{noise} as

$$\Delta\lambda_{\text{noise}} = \frac{\partial\lambda}{\partial I}\Delta I_{\text{noise}} = \frac{\partial\lambda}{\partial T}\frac{\Delta I_{\text{noise}}}{I_0}. \tag{4.3}$$

To determine $\partial\lambda/\partial T$, we use the derivative of the normalized transmittance (Fig 4.3a), resulting in $\partial T/\partial\lambda = 10.5\ \text{nm}^{-1}$. With measured values $I_0 = 69\ \mu\text{W}$ and $\Delta I_{\text{noise}} = 21$ nW, this results in $\Delta\lambda_{\text{noise}} = 29$ fm.

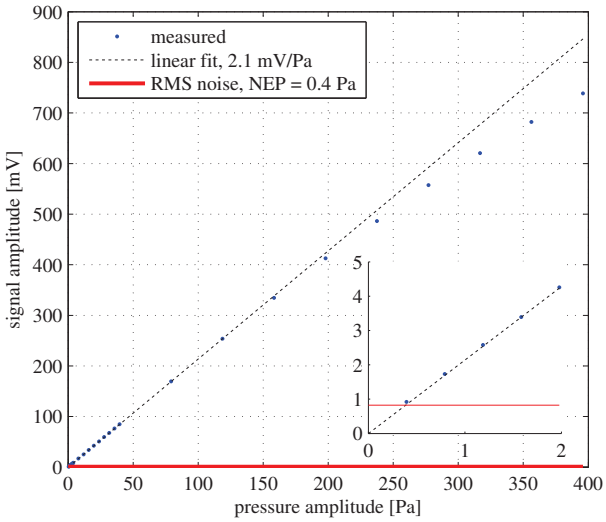

Figure 4.6: The measured amplitude of the OMUS output signal (blue points) versus the amplitude of the incident pressures, calibrated with a hydrophone. The sensitivity was obtained with a linear fit through the linear region of the system (dashed black line) and has a tangent of 2.1 mV/Pa. The red line is the RMS value of the measured output noise (0.8 mV). The crossing of the lines gives the NEP at 0.4 Pa. The results apply to the center frequency of the OMUS ($f_0 = 0.76$ MHz).

4.4 Discussion

The results demonstrate that we fabricated a very sensitive and small ultrasound sensor compared to the polymer ring resonators [67] and even state of the art piezo-electrical devices. This sensor can easily be repeated into an array of sensors by using waveguide gratings or echelle gratings [75]. These passive optical (de)multiplexers convert a broad spectrum into many wavelength channels and vice versa. When we use grating coupled ring resonators [76] only one of the many resonance peaks per ring resonator will be present in a wavelength channel, hence allowing to successively stack as many sensors as possible into the available spectrum. Underneath these parallel photonic waveguides with grating coupled ring resonators multiple membranes can be created using dry etching or other techniques [84]. A dense array of sensors is particularly beneficial in the field of intravascular ultrasound, where the outer dimensions of the catheter are restricted to 1 mm and every catheter can only be used once due to hygiene codes. This application will require integration with a separate source (e.g., a piezo-electric element) to form a hybrid transducer. Moreover, an increase of the acoustical center frequency to 15-20 MHz will be necessary, which in principle should be feasible through redimensioning the sensor. Another interesting field of application is photoacoustics where high SNR and a small bandwidth are needed [85].
In view of its small spatial footprint of 124 μm diameter, the question arises whether sensor is more prone to noise. This topic will be further adressed in Chapter 6. Nevertheless, the obtained detection limit, or NEP, of 0.4 Pa is better than the NEP of 0.5 Pa offered by the state of the art piezo-electrical device with a 65 times larger surface area.
To optimize our sensor as medical imaging device, there are a few aspects that can be improved. The most important one is addition of absorbing layers or other adjustments to the membrane to increase the bandwidth, which is now 4 times less than for conventional transducers. The resonance frequency of the current OMUS is comparable with the photo-acoustic breast tomography sensor, but needs to be increased for almost all other medical applications. This can be achieved by further reduction of the membrane diameter or by designing a different membrane shape.
Improvements can also be obtained in the dynamic range. With the current detection system, the dynamic range is limited. This could be drastically increased when we use a similar interrogator system as the one used by Rosenthal *et al* [68]. In their paper, coherence-restored pulse interferometry (CRPI) is introduced which enables them to track the location of an optical resonance peak or dip over time. In that case, the dynamic range will not be limited by the optical interrogation system.
Although further development is needed, with this first prototype we gave proof of the OMUS concept and demonstrated a very sensitive sensor that may form the basis of future ultrasound transducers.

4.5 Method

The optical path of the measurement set-up starts with a tunable laser (Agilent, 81940A) to generate the light. The light passes through an in-fiber isolator (Opto-link Cooration Ltd., OLISO-I-S155), in-fiber attenuator (Opto-link Corporation Ltd., OLVAO-MN-155-2TA) and an in-fiber polarization controller (Thorlabs, FPC560) and is then coupled into the chip. The polarization controller is required because the optical waveguide on the OMUS only accepts one polarization state. The other fiber of the chip is connected to a photo-receiver (Newport, Newfocus 1811-FC-AC).
The acoustical part of the set-up contains a 1 MHz ultrasound transducer (Olympus, Panametrics V314) as source, which is connected to an arbitrary waveform generator (Agilent, 33521A). All the equipment is connected to a computer and we use 16-bit AD-cards (Spectrum, M314142-exp) with a sampling rate up to 250 MSa/s to acquire all the data. The ultrasound source and OMUS are placed in a water basin on a fixed distance of 23.2 cm from each other. The temperature of the water basin is regulated within 0.1°C by a thermostat (Grant Instruments, GD120) and we use a needle hydrophone (1 mm, Precision Acoustics) to measure the pressure generated at the position of the OMUS.
Every series of measurements starts with a short scan of the optical transmission to determine the optical resonance wavelength. Then we step through the optical wavelengths of the laser, starting from a position halfway the flank, to find the optical wavelength with the highest sensitivity. At this optical wavelength, the successive measurements were performed, by transmitting different sound waves towards the chip. The transmitted acoustical pressure has the shape

$$p(t) = A \exp\left[-\left(\frac{t-\tau_d}{\frac{N}{2f_0}}\right)^2\right] \sin\left(2\pi f_0 \left[t-\tau_d\right]\right), \tag{4.4}$$

where p is the acoustical pressure as a function of time t, A is the amplitude of the acoustic wave, τ_d is a fixed time delay, N is half the number of sine periods that are roughly visible below the gaussian envelope, and f_0 is the center frequency of the sine. We determined the transfer function of the OMUS by transmitting narrow-band pulses (N=20) at subsequent acoustical frequencies, and adjusted the amplitude in such way that we compensated for the transfer function of the source, as to keep the emitted pressure the same for every acoustical frequency. We measured the sensitivity by altering the amplitude at a fixed frequency of $f_0 = 0.76$ MHz. The noise measurements were perfomed without a transmitted acoustical signal. We performed every measurement series twice, one with the OMUS and one with the hydrophone, in which the last series provided a reference for the pressure values at the surface of the OMUS.

Chapter

5

Characterization of the optical micro-machined ultrasound sensor

Abstract – The development of ultrasound sensors for real time 3D ultrasound imaging has focused on miniaturization and extension from single elements towards large dense arrays. We proposed an optical micro-machined ultrasound sensor as basis for such future arrays. To optimize the basis element for a specific application complete understanding of the element is needed. This chapter describes the characterization of the basis element. We show that the measured response to changes in temperature correspond to literature with sensitivities around 80 pm/K. We measured a stronger response of the sensor to static pressure than predicted by a finite element model. We already showed that the sensor was very sensitive to ultrasound with a noise equivalent pressure of 0.4 Pa. In this chapter we are able to show that this sensitivity is indeed induced by the membrane of the sensor. Furthermore we show that the resonance frequency of the sensor can be tuned with the diameter of the membrane and we show that similar membrane diameters result in similar responses, i.e. the sensor is reproducible.

This chapter is based on the following publication:

S. M. Leinders, W. J. Westerveld, J. Pozo, P. L. M. J. van Neer, K. W. A. van Dongen, H. P. Urbach, N. de Jong, and M. D. Verweij, "First measurements on a novel type of optical micro-machined ultrasound transducer (OMUT)," in *Proceedings IEEE International Ultrasonics Symposium*, pp. 2572-2575, Sep. 2014.

5.1 Introduction

Real-time 3D ultrasound imaging techniques require transducers that consist of dense arrays [4]. Applications like intravascular ultrasound (IVUS), endoscopic ultrasound (EUS) or image guidance based intra-operative ultrasound restrict the outer dimensions of the transducer [86–90]. Hence in the last decade the development of ultrasound sensors is focused on miniaturization and extension from single elements towards large dense arrays [1]. The conventional transducers are made of piezo-electric material. Miniaturization and fabrication of small dense arrays is challenging for these conventional transducers especially in the wiring of the individual elements [59, 61]. Therefore alternative sensors and fabrication methods are widely investigated [91–95]. We proposed an alternative ultrasound sensor fabricated with micro-machining techniques comparable to CMUTs and PMUTs but based on integrated photonics instead of piezo-electric material [21, 78, 96]. The applied integrated circuit fabrication technology (CMOS) allows for ease of production. Furthermore, the advantage of the use of integrated photonic circuitry is the possibility to design small spatial footprints of the sensor elements ($\sim$10 μm [74]). Other advantages are its insensitiveness to electromagnetic interference, high speed communication and a broad bandwidth for data transmission. We fabricated this optical micro-machined ultrasound sensor and provided proof of concept [96]. This sensor can be used as a basis for building large dense arrays but further development of this sensor towards any application first requires complete understanding of its behavior.
This chapter presents a full characterization of the sensor. We performed temperature measurements, static measurements and dynamic measurements. The temperature measurements and static measurements are compared to literature [97, 98]. Next to the literature, the static measurements also compared to a finite element model as well. The dynamic measurements show to what extend the membrane read-out of the sensor corresponds to the motion of the membrane.
This chapter is organized as follows: first we describe the working principle of the sensor and the devices used for the study, then we present the theory to determine the influence on the optical wavelength shift of the sensor due to temperature and due to a static load. The influence of a static load can be extended to an expected wavelength shift due to an ultrasound pressure wave. Next, we describe the method and measurement set-up, followed by the results. We end with the conclusions.

5.2 Working principle and device description

The working principle of the sensor as well as the fabrication process and design considerations are already described in Ref [96]. For convenience we sum up the most important aspects in this section.
The optical micro-machined ultrasound sensor consists of a waveguide and a photonic ring resonator that are integrated onto a membrane (Fig. 5.1a). When a broad light spectrum is transmitted through the waveguide, a part of the spectrum is coupled into the ring resonator by means of a directional coupler [77]. The trans-

mitted spectrum at the output port of the waveguide shows dips at the optical resonance wavelengths λ_m of the ring resonator, given by

$$m\lambda_m = n_e l, \tag{5.1}$$

where m is an integer number, l the circumference of the ring and n_e its effective index of refraction. Incident acoustical pressure waves strain the membrane and hence the resonator. The induced strain in the resonator causes a shift in the optical resonance curves with respect to the undeformed state. The shift in resonance is what we want to observe.
When we load the sensor in several steps, we can obtain a translation of the resonance dip from the wavelength shift in successive scans of the entire spectrum. This is indicated in Figure 5.1b by the three different spectra in blue, red and green, which correspond to different added loads. This scanning procedure can be used for static measurements, but is too slow for detection of the ultrasound waves without use of a dedicated detector. To determine fast optical wavelength shifts, we transmit light, and hence measure the transmitted intensity, at one optical wavelength. This wavelength is chosen on one flank of the optical resonance curve of the undeformed resonator (in this case the red curve), such that a shift of the resonance curve directly translates into a modulation of the transmitted optical intensity, as is shown in Figure 5.1b. The intensity is measured using a photo diode. We realized the sensor using the following procedure. First, the

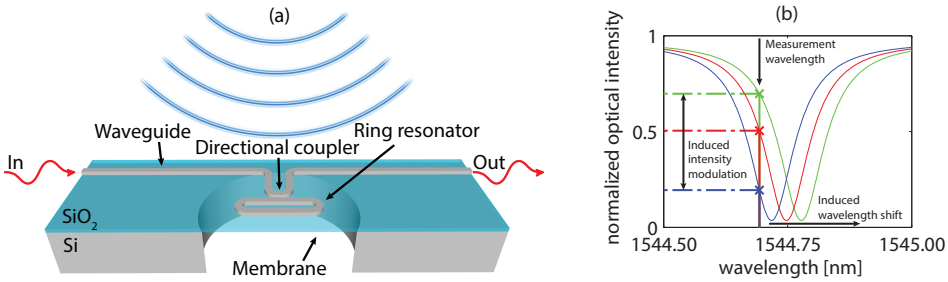

Figure 5.1: a) Sketch of the OMUS, showing the photonic micro-ring resonator on top of the membrane. b) Sketch of three intensity curves at the end of the waveguide, representing the different transmittances for different strain values of the photonic micro-ring resonator. Adapted from [96]

miniature optical circuitry was fabricated using a semi-industrial CMOS fabrication line at IMEC (Leuven, Belgium) via the ePIXfab platform [82]. The resulting wafer-piece (die) contains 220 nm high and 400 nm wide silicon waveguides on top of a 2 μm thick silicon-dioxide layer on a 250 μm thick silicon substrate. A 0.5 μm thick silicon-dioxide cladding was deposited to isolate the waveguide from the water. Second, we etched the membrane (124 μm diameter) from the back of the die using deep reactive ion etching with sulfur hexafluoride (SF_6) as etchant and we used the silicon-dioxide layer as a well-defined etch-stop.

The static and dynamic measurement set-ups require different sensors. Therefore, the sensors for the dynamic measurements were further processed. We glued those chips on a 1 mm thick glass plate. The plate contained a hole of 4 mm diameter, which was positioned behind the membrane. Finally, we connected optical fibers to the silicon photonic circuit of these sensors, which is referred to as packaging [83]. An overview of the used sensors is given in Table 5.1. The difference between the sensors is found in the post-processing of the device, diameter of the membrane and length of the optical ring resonator.

Table 5.1: Sensor description and use in different measurements. The first column list the sensor number, followed by the diameter of the membrane and race track (i.e. resonator) length. The glass layer indicates whether a glass layer is present or not. The last column indicates the measurements in which the device is used, where T is the temperature measurements, V is the vibrometer measurement and P is the pressure measurement.

Sensor	membrane diameter [μm]	racetrack length [μm]	glass layers	measurements
Chip 4	60	30	yes	T
Chip 11	124	40	yes	V,T
Chip 13	101	40	yes	V,T
Chip 16	104	40	no	P
Chip 17	63	30	no	P

5.3 Theory

This section describes the influence of temperature on the optical resonance and the physical relations between the deformation of the membrane and the expected optical resonance shift. We start with the dependence on temperature as this is independent of the mechanical deformation (Sec.5.3.1). Then we describe the deformation of the membrane. The membrane has an initial hollow position. When a pressure load is applied to the sensor, the membrane will deform further. This deformation induces (more) strain in the optical ring resonator, which causes a shift in the optical resonances. These different aspects are discussed below. First we discuss the initial condition of the membrane (Sec. 5.3.2). Second we discuss the relation between the pressure and deformation of the membrane (Sec. 5.3.3) and third we describe the expected optical wavelength shift due to this deformation (Sec 5.3.4).

5.3.1 Influence of temperature

Temperature influences the propagation of light through the silicon waveguide. The refractive index is dependent on temperature according to:

$$\beta(T) = \frac{1}{n}\frac{dn}{dT}, \tag{5.2}$$

with dn/dT being the thermo-optic coefficient [97, 99]. The change of refractive index is significant for silicon ($\beta = 1.79 \times 10^{-4}$/K) and is an order of magnitude lower for SiO_2. The thermal expansion coefficient is given by

$$\alpha(T) = \frac{1}{h}\frac{dh}{dT}, \tag{5.3}$$

with h being the sample thickness. The thermal expansion of Si measured around room temperature at 1530 nm wavelength is low ($\alpha = 2.58{\cdot}10^{-6}$/K) compared to the change of refractive index [99]. This means that the effect of the expansion of the cross-section of the waveguide is negligible compared to other effects. The change in the direction of propagation can give rise to noticeable spectrum changes. To determine the total effect on the silicon waveguide due to changes in temperature, the wavelength dispersion of the effective index has to be taken into account as well. A derivation of this formula is beyond the scope of this thesis, but is given by [100]

$$\lambda = \frac{L}{m}\left(1 - \left(\frac{L}{m}\right)\left(\frac{\partial n_{\text{eff}}}{\partial \lambda}\right)\right)^{-1}\left(\frac{\partial n_{\text{eff}}}{\partial \epsilon_c}\right) 2n_{\text{si}}\left(\frac{\partial n_{\text{si}}}{\partial T}\right)(T - T_0) + \frac{L}{m} n_{\text{eff}}(\lambda_0), \tag{5.4}$$

with ϵ_c the relative dielectric constant for the material that is changing with temperature, in this case the silicon waveguide.

5.3.2 Initial condition

It is known from literature that the fabrication process of thin films can cause residual stress [101–107]. In general is it difficult to determine the state of residual stress in a thin film because it depends on the specifics of the fabrication process and varies through the film thickness [103]. There are different processes that can contribute to the residual stress, but the main cause in our case is due to the difference in thermal expansion coefficients of the materials [105]. Although this difference is not important when the device is used, it is of importance when the CMOS structures are made at elevated temperatures. The silicondioxide is deposited onto a substrate of single-crystal silicon at these elevated temperatures. The wafer of our sensor is made with the smart cut technique [108]. Due to the different thermal expansion coefficients of silicon and silicon dioxide thermal stresses are induced in these materials during manufacture and remain there during the subsequent use of the devices. For thermal mismatch problems, the elastic strain needed to fit the film to the substrate is given by

$$\epsilon = -(\alpha_f - \alpha_s)(T - T_0) = -\Delta\alpha\Delta T, \tag{5.5}$$

where α_f and α_s are the linear thermal expansion coefficients of the film and substrate, respectively, T is the current temperature and T_0 is the initial temperature at which the film and substrate were in a stress-free state [101]. The varying values for the silicondioxide expansion coefficient in literature and the fact that thermal expansion coefficients in a thin film can differ from the bulk values make it difficult to predict the strain values present in the membrane [102,107]. The stress in a thin

film deposited on a substrate can be approximated in second order by a biaxial homogeneous stress superimposed on a linear biaxial stress gradient. The stress in the film is in this approximation biaxial at all points, but varies linearly from the top surface to the bottom surface [106]. Both compressive and tensile stresses can be present, but it is known that silicon dioxide resulting from a thermal oxidation of silicon is in a state of compression on the silicon surface [105]. When the membrane is created by locally removing the substrate, the internal stress in the membrane will relax and the device will deform [102, 106].

5.3.3 Deflection

The deflection of uniformly loaded plates is described depending on the size of the displacement. For small displacements, linear theory can be used. When the displacement is in the order of the thickness of the plate, large deflection theory is used. This theory assumes that the vertical displacement w is much larger than the lateral displacements u and v and that the normals to the undeformed middle surface remain the normals to the deformed middle surface [17, 109–112]. The governing differential equations or Kármán equations for the bending of a circular plate due to a load P are [111]

$$P = \frac{Eh^3}{12(1-\nu^2)}\nabla^4 w - \frac{h}{r}\frac{\partial\phi}{\partial r}\frac{\partial^2 w}{\partial r^2}, \tag{5.6}$$

$$\nabla^4\phi = -\frac{E}{r}\frac{\partial w}{\partial r}\frac{\partial^2 w}{\partial r^2}, \tag{5.7}$$

where E is the Young's modulus, ν is the Poisson ratio and ϕ is the Airy stress function. The biharmonic operator ∇^4 is given by

$$\nabla^4 = \left(\frac{\partial^2}{\partial r^2} + \frac{1}{r}\frac{\partial}{\partial r}\right)^2. \tag{5.8}$$

In case of very large deflection theory the strain relations contain extra terms compared to the linear theory, with second order dependence on both the u and w direction resulting in [17]

$$\epsilon_r = \frac{du}{dr} + \frac{1}{2}\left[\left(\frac{du}{dr}\right)^2 + \left(\frac{dw}{dr}\right)^2\right] \quad \text{and} \quad \epsilon_\theta = \frac{u}{r}, \tag{5.9}$$

where ϵ_r is strain in the radial direction, ϵ_θ is the strain in the tangential direction and u is the displacement in the radial direction. These strain relations can be extended with intrinsic strain [110, 111].
Next to the intrinsic strain our sensor has an initial displacement in the order of the thickness h of the membrane. In such case superposition of the initial condition and the deflection due to a load can not be applied [113]. Therefore we will use a finite element model to determine the amount of strain that is induced by the initial deformation and the pressure load together.
For dynamic measurements we assume that the deformation of the membrane at

its fundamental mode has a similar shape as the static loading. In that case the displacement in time is given by

$$\begin{aligned} w(t) &= w_{stat} + \Delta w(t), \\ &= w_{stat} + \frac{\partial w}{\partial P}\Delta P(t). \end{aligned} \tag{5.10}$$

So at the position of the static curve where the load matches the load of the water, the slope should match the displacement per load of the dynamic measurements.

5.3.4 Optical wavelength shift

We now determine the optical wavelength shift due to a certain strain at the position of the ring resonator. Equation 5.1 gives the dip position of the transmitted spectrum of the undeformed ring resonator. When strain S is applied these dips at the resonance wavelengths λ_m appear when the phase delay δ of one round trip through the ring is

$$\delta = \oint n_e(\rho, \lambda)\frac{2\pi}{\lambda}\mathrm{d}\rho = m2\pi, \tag{5.11}$$

or

$$m\lambda_m = \oint n_e(\rho, \lambda_m, S_z)\,(1 + S_\rho(\rho, S_z))\,\mathrm{d}\rho, \tag{5.12}$$

where z indicates the specific direction of the long sides of the racetrack resonator and ρ indicates the direction along the racetrack in general. The effective index of the waveguide depends on its mechanical deformation. Moreover, the local strain in the direction of the track S_ρ is taken into account by stretching each element $\mathrm{d}\rho$ to $(1 + S_\rho)\mathrm{d}\rho$. From previous strain measurements, we know that the optical wavelength shift is linear with respect to strain. We derived a formula of this shift in such way that it shows dependence on three different physical aspects [78]

$$\frac{\partial \lambda_m}{\partial S_z} = \underbrace{\frac{n_e}{n_g}}_{\text{dispersion}} \Big\langle \underbrace{\frac{\lambda_c}{n_e}\frac{\partial n_e}{\partial S_z}}_{\text{eff. index}} + \underbrace{\lambda_c \frac{\partial S_\rho}{\partial S_z}}_{\text{track-length}} \Big\rangle, \tag{5.13}$$

where n_g is the group index and λ_c is the resonance wavelength without deformation.

5.4 Description and numerical modeling parameters of the measurement set-up

The characterization of the sensor is performed with three different measurements; one set-up to determine the dependence on temperature (Sec. 5.4.3), one in which we measured the response due to a static pressure (Sec. 5.4.1) and one in which we measured the deflection of the membrane due to an incident acoustic wave with a simultaneous optical read-out of the sensor (Sec. 5.4.2). This section describes all measurement set-ups as well as the parameters that were used in the numerical FEM model (5.4.4).

5.4.1 Static measurement set-up description

As described in Section 5.2, we use unpackaged sensors for the pressure measurements. Therefore, we have to align two single optical fibers above the grating couplers to couple the light into the sensor. The optical path of this setup contains a tunable laser (Agilent, 81960A) to generate the light followed by an in-fiber polarization controller (Thorlabs, FPC560). This fiber ends at an translational stage which can be positioned above the sensor. The fiber at the other end of the sensor is connected to an optical power meter (Agilent, N7744A). The sensor is positioned on a chuck. Using a membrane vacuum pump we are able to decrease the pressure under the membrane. We measure the pressure with a calibrated pressure sensor (Vacuubrand, CVC 3000). The set-up is shown in Figure 5.2a. For every measurement series, we sweep the wavelength of the laser through 400 pm around the dip position and measure the mean dip position for a given pressure during 75 seconds.

5.4.2 Dynamic measurement set-up description

The basic equipment, used for the dynamic vibrometer measurements was similar to the setup used in Ref [96] (Fig. 5.4b). In the optical path of the measurement set-up we use a tunable laser (Agilent, 81940A) to generate the light. The light passes through an in-fiber isolator (Opto-link Cooration Ltd., OLISO-I-S155), an in-fiber attenuator (Opto-link Corporation Ltd., OLVAO-MN-155-2TA) and an in-fiber polarization controller (Thorlabs, FPC560), and is then coupled into the chip. The other fiber of the chip is connected to a photo-receiver (Newport, Newfocus 1811-FC-AC). The acoustical part of the set-up contains a 1 MHz ultrasound transducer (Olympus, Panametrics V314) as a source, which is connected to an arbitrary waveform generator (Agilent, 33521A). The ultrasound source is placed in a water basin on a fixed vertical distance of 10 cm below the sensor. The OMUS is attached to a hollow tube and positioned in such way that the sensor itself is submerged in water while the back of the tube is still above the water surface so only air is present behind the membrane. The ultrasound source and OMUS are positioned in line with a laser vibrometer (Polytec, OFV5000) that can measure the displacement of the OMUS. The vibrometer has a displacement card (Polytec, dd-300) that can measure displacements up to 150 nm with a resolution of 0.1 pm/$\sqrt{\text{Hz}}$ at a maximum sample frequency of 24 MHz. We use a 20x objective (f=200, M Plan Apo NIR) to focus on the center of the back of the membrane or on the back of the chip. All the equipment is connected to a computer and we use 16-bit AD-cards (Spectrum, M314142-exp) with a sampling rate up to 250 MSa/s to acquire all the data.
Every series of measurements starts with a short scan of the optical transmission spectrum to determine the optical resonance wavelength. Then we step through the optical wavelengths of the laser, starting from a position halfway the flank, to find the optical wavelength with the highest sensitivity. At this optical wavelength, the successive measurements were performed, by transmitting different

sound waves towards the chip. The transmitted acoustical pressure has the shape

$$p(t) = A \exp\left[-\left(\frac{t-\tau_d}{\frac{N}{f_0}}\right)^2\right] \sin\left(2\pi f_0\left[t-\tau_d\right]\right), \tag{5.14}$$

where p is the acoustical pressure as a function of time t, A is the amplitude of the acoustical wave, τ_d is a fixed time delay, N is the number of sine periods that are roughly visible below the gaussian envelope, and f_0 is the center frequency of the sine. We determined the transfer function of the OMUS by transmitting narrow-band pulses (N=30) at subsequent acoustical frequencies. We measured the sensitivity by altering the amplitude at a fixed frequency of $f_0 = 0.8$ MHz for Chip 11 and at $f_0 = 1.05$ MHz for Chip 13.

5.4.3 Temperature measurement set-up description

The optical equipment used for these measurements is exactly the same as the one used for the dynamic vibrometer measurements. Because the sensors are packaged, we can submerge them in the water basin. We position them in the middle of the basin and measure the temperature of the water with a calibrated analog thermometer that has a precision of 0.005°C. The water temperature is regulated with a thermostat (Grant Instruments, GD120) within 0.1°C. We vary the temperature with steps of 1°C and perform measurements when the temperature is stable.

5.4.4 Numerical modeling parameters and methodology

We numerically model our sensor as a membrane with clamped boundary conditions. We only model a quarter of the membrane thus employing the axisymmetric conditions. The membrane consist of three layers; first the 2 μ main SiO_2 layer, second the 0.22 μm optical Si layer, third the 0.5 μm SiO_2 cover layer. The Young's moduli are 70 GPa and 170 GPa for the SiO_2 layer and Si layer respectively. The Poisson ratio is 0.19 for SiO_2 and 0.27 for Si. The FEM model uses curved triangular finite rotation shell elements that can handle the expected deformations [114]. The pressure is increased from 0 to 7 MPa.
To determine the wavelength shift per strain (Eq. 5.13), we need to have estimates for the effective index, n_e, group index n_g, resonance wavelength λ_c and change in effective index due to strain $\frac{\partial n_e}{\partial S_z}$. We obtained these values for several long ring resonators and waveguides with different widths [78]. We use these results as estimate for the ring resonators. With an estimated effective index of 2.2, group index of 4.32, resonance wavelength of 1550 nm and a change in effective index $\frac{\partial n_s}{\partial S_z} = -0.72$ we get an optical wavelength shift due to strain of 0.55 pm/microstrain.

5.5 Results

We started the characterization of the OMUS by determining its dependence on temperature. Next we measured the response to a static load and compared this to the FEM model. We continued by measuring the membrane displacement as

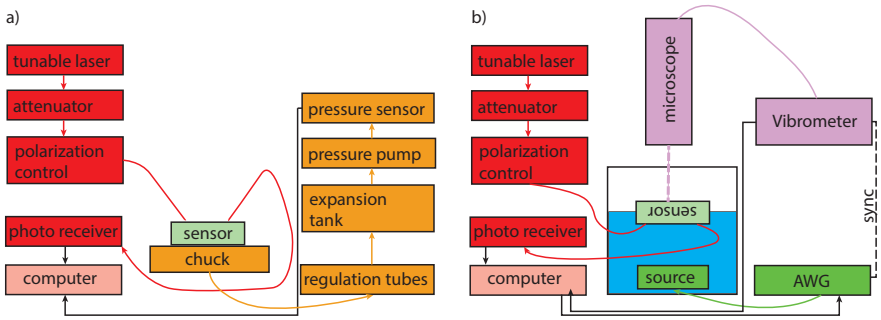

Figure 5.2: Two measurement setups to measure the influence of a) static pressure on the optical resonance shift and b) ultrasound pressure on the optical resonance shift.

well as the chip displacement due to an incident acoustical pressure wave. All measurement results are described below.

5.5.1 Temperature measurement results

The influence of temperature was first visualized in the transmission curve of the sensor. The local temperature is influenced by the transmit intensity of the laser. To show this, we determined the shape of the optical resonance curve by measuring the transmittance $T(\lambda)$ from the input to the output of the OMUT. The intensity I at the output of the chip for a static situation is given by $I = T\, I_0$ with I_0 the maximum output intensity far away from the resonance dip. This maximum output intensity I_0 is related to the maximum output power P_0 that we measure with the photo-receiver. We measured the transmittance by stepping through successive wavelengths with the laser for two different output powers. Figure 5.3 shows the transmittance for output powers P_0 of 10 μW and 60 μW. The low intensity curve (blue line) shows the expected symmetric resonance curve with a FWHM of 100 pm. The curve for higher power (red line) shows a different transmittance. The asymmetry of the resonance dip can be explained by the heating of the ring resonator due to the dissipation of light. Silicon has a strong thermo-optical effect and the resulting shift in resonance wavelength is about 80 pm/°C [97]. During the measurement we stepped through the successive wavelengths and therefore changed the amount of light in the ring, and thus the dissipation. On the left flank of the resonance dip, the amount of light in the ring resonator increases for increasing laser wavelength, resulting in a shift to the right of the resonance dip during the measurement sequence. On the right flank of the resonance dip, the amount of light for increasing laser wavelength decreases and the resonance dip thus shifts to the left. Therefore, with this measurement method, at relatively high power values the transmission curve is altered due to the heat generated by the laser source.

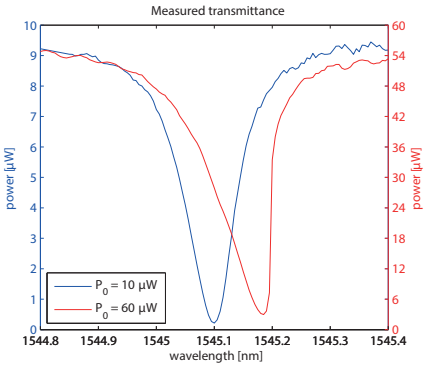

Figure 5.3: The measured transmittance versus optical wavelength, for an maximum output power P_0 of 10 μW (blue line) and 60 μW (red line).

To determine the thermo-optical effect more thoroughly we measured the optical wavelength shift of three sensors. The straight part of the racetrack of two resonators is 40 μm and one ring has a straight part of 30 μm. The temperature was varied from 23°C to 27°C in steps of 1°. At every temperature several measurements were performed. The measurement results of Chip 13 are similar to the other measurements and clearly show that all the measured temperature shifts are on a straight line (Fig. 5.4). The measured sensitivity of the optical wavelength shift per degree centigrade is 80.0°C, 82.5°C and 80.9°C for chip 4, chip 11 and chip 13 respectively. The coefficient of determination R^2 is 0.99 for all measurements and shows that the results are easily fitted to the linear regression [115]. The small difference between the three devices may have to do with small fabrication variations. The measurements correspond well with calculations and other measurements in literature where the optical wavelength shift varies between 70 pm/K to 90 pm/K for different waveguide widths [97].

5.5.2 Static measurement results

When we look at the initial condition of the membrane, it can be seen through a microscope that the membrane is in a hollow position. This initial displacement is confirmed with a white light interferometer (Bruker, ContourGT-K). The result of the latter is shown in Figure 5.5. Due to the rough surface of the device the interferometer measurement can only be used to get an estimate for this initial displacement, which is in the order of 4 μm.
We measured the optical wavelength shift of the membrane due to a static loading. The results are shown in Figure 5.6 and show a nonlinear response. The response is sensitive for small pressures and less sensitive for the higher pressures. The maximum wavelength shift is in the order of 200 pm. These results are similar to the measurement results of Hallynck [98]. They measured a similar curve in the response to the same pressure load with a maximal optical wavelength shift of 208 pm for a similar device with a rectangular membrane and a ring resonator.

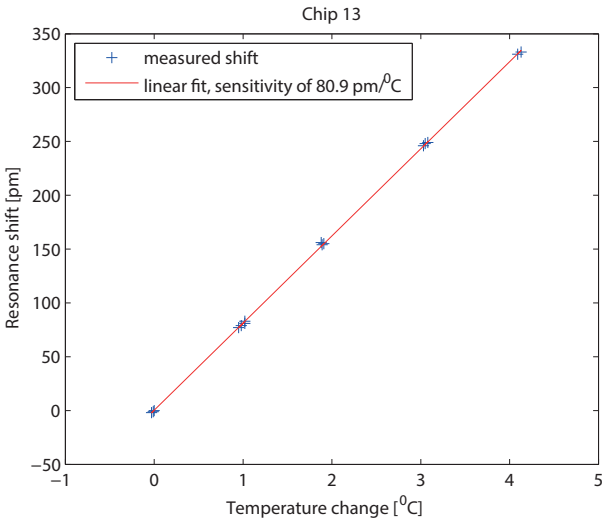

Figure 5.4: Measured optical wavelength shift change versus temperature change. The linear fit has a R^2 of 0.99.

We modeled the device to see whether we could fit the measurements and obtain the membrane displacement. Because we have no exact measurements of the initial deflection, we vary the initial strain in the model to obtain different initial deflections of the membrane. We modeled two cases, one in which the membrane has no initial strain or displacement and one in which the initial displacement of the membrane is obtained with an initial strain of 1 %. The results are shown in Figure 5.7 with on the left hand side the displacement of the membrane and on the right hand side the change in strain in the layer of the waveguide due to loading. We use the change in strain to determine the optical resonance shift due to loading, using the initial resonance wavelength as starting position. It is shown that an initial strain of 1% results in an initial displacement of 4.4 μm. Furthermore, it can be seen that the general trend for the displacement and strain becomes nonlinear, but that the pressure load needed for this non-linearity is much larger than the one used for the measurements. In the regime of interest both the displacement and strain are linear. The initial strain causes a change in sign of the strain in the top layer. Although the membrane is buckled due to the initial strain, there is still strain present in the entire membrane when there is no loading. We obtain -108 μstrain at 70 kPa with no initial strain and 48 μstrain at 70 kPa with an initial strain of 1%. When we use the conversion of 0.55 pm/μstrain we obtain an expected wavelength shift of -59 pm and 26 pm. These values are much lower than the shifts that we have measured. The sign of the measurements correspond to the model with no initial strain.

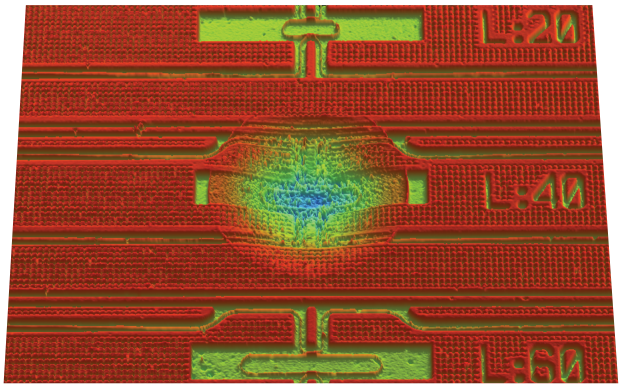

Figure 5.5: Interferometer measurement of the sensor. The color indicates the measured height of the sensor where a red color represents the flat surface and a blue color the maximum displacement. There are three different (isolated) ring resonators visible with straight lengths from 20 to 60 μm. The hollow membrane is clearly visible around the 40 μm ring resonator. The measurement contains too much noise to obtain accurate quantitative values of the displacement of the membrane.

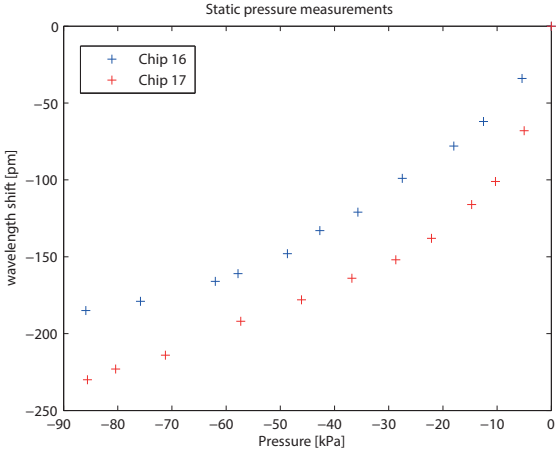

Figure 5.6: The optical induced wavelength shift due to pressure for two sensors, Chip 16 and Chip 17.

5.5.3 Dynamic measurement results

We first investigated whether the read-out of the ring resonator is only influenced by the deformation of the membrane. We obtained two time-traces simultaneously,

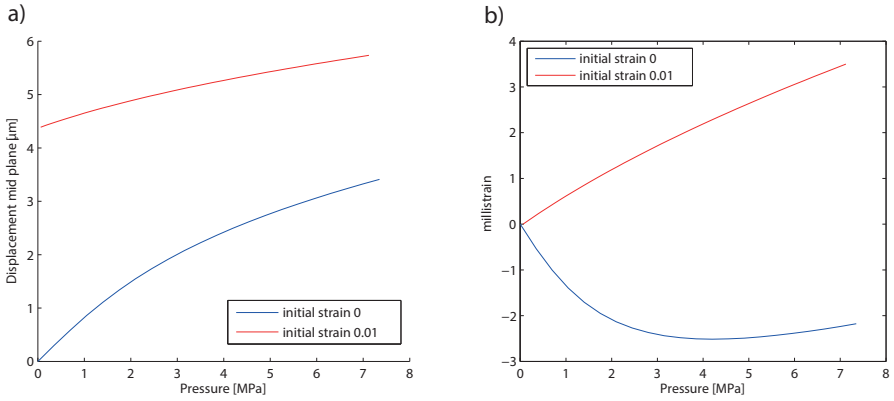

Figure 5.7: The modeling results for a membrane with no initial strain (blue) and an initial strain of 1% (red). The displacement in both cases is shown in a) and the corresponding strain difference (the initial strain with zero pressure subtracted) in b).

one by interrogating the sensor and one from the vibrometer that measures the displacement of the membrane. The time-traces of both signals are shown in Figure 5.8. It is clearly visible that both curves have the same response. The phase difference between the two signals is due to the coaxial wiring of the set-up and is dependent on frequency. When we excite the sensor at successive frequencies the transfer function can be determined. The transfer function of the membrane

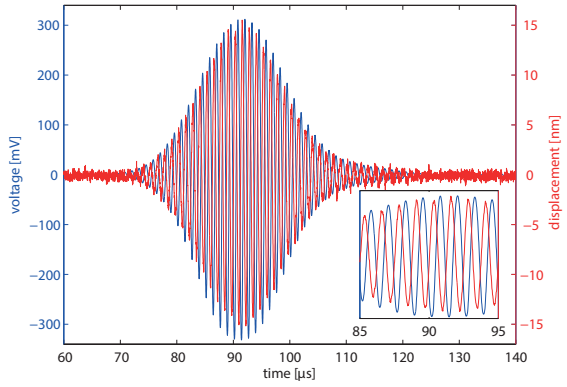

Figure 5.8: Two simultenous recorded timesignals are shown of Chip 11 transmitted with a center frequency of 0.8 MHz. One of the optical read-out of the OMUS (read) and one of the displacement of the membrane (blue). A zoom of both time traces is shown in the lower right corner.

displacement as well as the OMUS signal are shown in Figure 5.9 for two sensors. It is shown that Chip 11 has its resonance frequency at 0.8 MHz. This is comparable to the OMUS of Ref [96], which is a sensor with a similar membrane diameter (124 μm). Chip 13 has a higher resonance frequency of 1.05 MHz which is expected in view of the smaller membrane diameter of 100 μm. Clearly, the membrane displacements and the OMUS signal have almost the same transfer functions.

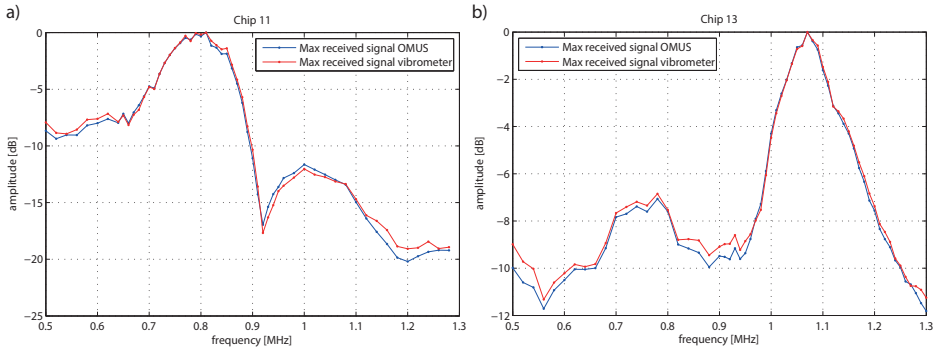

Figure 5.9: The transfer functions of the membrane and the sensor signal. a) the results for Chip 11 and b) the results for Chip 13. The signals are normalized with respect to the maximum of each function. These maxima correspond for Chip 11 to 270 mV (vibrometer signal) and 199 mV (OMUS signal) and for Chip 13 to 111 mV (vibrometer signal) and 172 mV (OMUS signal).

Next we determined the sensitivity of the OMUS, which is related to the membrane displacement for a given amplitude of the incident acoustical pressure wave. This is determined by transmitting acoustical pressure waves with increasing amplitude and center frequency f_0 of the sensor. The results are shown in Figure 5.10. For small deformations of the membrane, and hence for small optical wavelength shifts, the sensor response is linear. For higher pressures, the sensitivity curve starts to deviate from the linear curve. This nonlinear response of the OMUS occurs because of the used interrogator system. With this system the linear dynamic range of the OMUS is determined by the width and shape of the optical resonance curve. If the deformation of the membrane, and hence the shift in optical resonance is too large, the response of the OMUS is distorted. From the response of the vibrometer it can be seen that the displacement of the membrane is still linear for higher pressures.
The difference between the chip displacement (black line) and membrane displacement (red line) confirms that for both sensors only the membrane is significantly excited by the incident pressure wave. The optical resonance shift $\Delta\lambda$ (blue line)

is obtained from the intensity modulation ΔI of the photodiode according to

$$\Delta\lambda = \frac{\partial\lambda}{\partial T}\frac{\Delta I}{I_0}, \tag{5.15}$$

where $\partial\lambda/\partial T$ is determined from the derivative of the normalized transmittance T (Figure 5.1b). We obtained a derivative of $\partial T/\partial\lambda = 13.2\ \mathrm{nm}^{-1}$ for Chip 11 and $\partial T/\partial\lambda = 8.3\ \mathrm{nm}^{-1}$ for Chip 13 from the measured spectra. By dividing the optical resonance shift with the measured displacement we obtain a sensitivity of $2,1\frac{\mathrm{pm}}{\mathrm{nm}}$ (resonance shift over membrane displacement) for Chip 11 at 0.8 MHz and $1,6\frac{\mathrm{pm}}{\mathrm{nm}}$ for Chip 13 at 1.05 MHz.

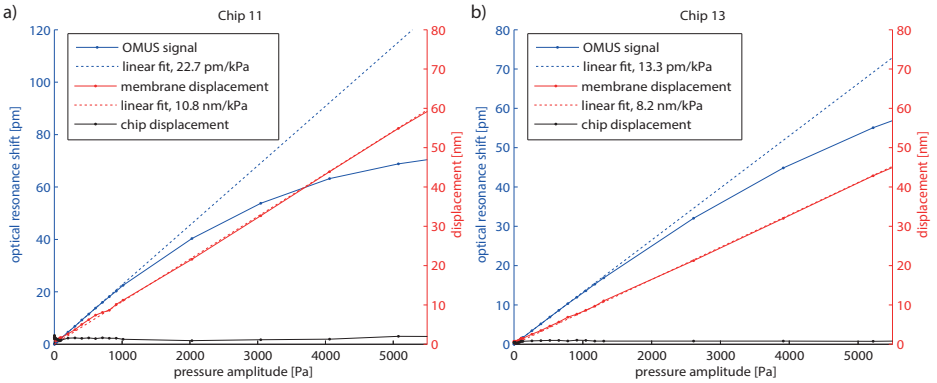

Figure 5.10: Measured optical wavelength shift (blue line), membrane displacement (red line) and chip displacement (black line). a) the results for Chip 11 and b) the results for Chip 13. We obtained the sensitivity of the OMUS signal by making a linear fit through the first measurement points (dashed blue line). The sensitivity of the displacement was determined by making a linear fit through the vibrometer data (dashed red line).

5.6 Discussion

We characterized the sensor by determining its response to temperature, a static loading and a pressure wave. We did this with three different measurements applied to several sensors. We showed that the OMUS is sensitive to changes in temperature. The response is linear and corresponds to calculated values and measured values in literature. However, we do not expect that temperature effects will influence our acoustical measurements, because the influence of temperature is a relatively slow effect (order of seconds) compared to the ultrasound measurements that take place in a short amount of time (order of microseconds). Furthermore, the displacements of the membrane are small and hence the differences in wavelength shifts are small. Therefore we will write the influence of temperature only

as an extra translation $\Delta\lambda_h$ of the low-power curve in Figure 5.3, and consider this translation to be constant during the ultrasound measurements.
We measured the initial position of the membrane and found that the membrane is buckled. The main reason of this buckling is strain due to the fabrication process. There are several methods known from literature that can avoid this internal strain, for instance by deposition of another film [116, 117] or by ion implantation [118]. Another solution is reported by Iwase *et al.* who adjusted the structure of the sensor in such way that it corrects for the buckling by design [119]. All these methods have consequences for the design of the membrane, which means that they influence the resonance frequency and possible sensitivity. This is important to take into account when the design needs to be optimized for an application as ultrasound sensor.
Optical ring-resonators have already been used to measure static loading with a linear response between the load and optical wavelength shift. The sensitivity of the sensor depends on the radius of the ring resonator as well as the thickness of the membrane [120]. The buckling of the membrane due to internal strain in the sensor seems to change the linear static behavior since we measured a non-linear response to a static pressure. We were not able to explain the measurement results of the static measurements with a finite element model: the non-linearity occurs at much higher loadings in the model as in the measurements. There are several aspects that need to be investigated further to find a possible explanation. First, the exact values of the initial displacement and material constants are unknown. This makes it difficult to build an exact model to fit our measurements. Second, the status of initial strain is unknown. We showed with the model that the amount of strain as well as the sign is completely different for a situation with no initial strain and one with initial strain. Third, the linear response of the ring resonator is only investigated for cases of pure bending, where in the situation of static loading, membrane strain is an important factor as well.
The stronger response of the device due to static loading may also be an explanation for its sensitivity to ultrasound. Due to the missing information of the static displacement of the membrane it is not yet possible to obtain a full description of the displacement of the sensor as described by Eq. 5.10. Instead, we are able to match the optical wavelength shift of the sensor due to pressure in a similar manner. The highest derivative of the static measurements is found at the beginning of the curve and has values in the order of 10 pm optical wavelength shift/kPa. These values are in the same order of magnitude as the linear fit of the vibrometer measurements. Because the sensors are barely submerged under water when the vibrometer measurements are performed, the static loading due to the water column is in the order of several pascals. Therefore the steep derivative of the strain measurements seems to match the sensitive response to ultrasound.
With the vibrometer measurements we are able to show that the response of the sensor is a result of the oscillating membrane. We conclude from the measurements that only the membrane is significantly oscillating due to the incident pressure wave and the back of the sensor is not. Hence the response of the ring resonator matches the response of the membrane. With the two devices that were fabricated for the vibrometer measurements we showed that the sensor is reproducible.

Chapter

6

Derivation of the acoustical noise pressure present at the surface of piston transducers

Abstract – In medical diagnostics, ultrasound devices are often used to image organs or tissue from positions inside the human body. Therefore it is paramount to design small and sensitive sensors. In search for miniature ultrasound sensors we developed an opto-mechanical micro-machined ultrasound sensor based on integrated photonics instead of piezo-electric material. To predict the lowest detectable pressure we wanted to determine the noise level of this sensor. Due to the lack of electrical circuits the noise of the sensor is only caused by two noise mechanisms; one is the molecular agitation in the medium hitting the surface of the sensor and the other the mechanical thermal noise induced in the sensor itself. The resulting acoustical noise is not well described in literature. Therefore this paper expands the existing knowledge of acoustical noise by analyzing both noise mechanisms. We show that in thermodynamic equilibrium the noise power delivered by the medium to the sensor indeed balances the noise power delivered by the sensor to the medium. Moreover we show that for sensors with vanishing aperture area, the noise pressure due to the molecular motion in the medium will reach a well-defined finite limit.

6.1 Introduction

The need of 3D real time images in medical ultrasound requires ultrasound transducers that consist of dense arrays of elements [4]. Next to the increasing amount of elements, developments of transducer design also involve further miniaturization by the introduction of micro-machining processes [1]. In search for miniature acoustic sensors we developed an opto-acoustical ultrasound sensor [96]. We showed that this sensor is very sensitive and can measure pressure levels down to 0.4 Pa. We wanted to determine the absolute noise floor and found that the noise floor was much smaller than predicted from calculations found in literature. The pressure noise in our sensor originates from intrinsic thermo-mechanical fluctuations in the sensor itself [121] and thermo-acoustical noise due to molecular agitation in the medium [122]. Gabrielson [123] reviews several techniques to calculate the mechanical thermal noise induced in micro-machined sensors. However, some aspects are missing in the literature. First of all, the noise due to molecular agitation in the medium is not explicitly derived. Second, the current description of the acoustical noise received by a transducer uses the specific acoustic impedance and is defined as the acoustic impedance of the medium (ρc) times the surface area of the transducer. When we use this specific acoustic impedance to determine the noise floor of our sensor, the noise blows up for sensors with a small aperture. Third, with noise calculations of conventional piezo-electric transducers this acoustical noise is only implicitly taken into account as a partial contribution to the total noise at the electrical output [1, 2]. Hence there is a need to derive a theory that describes the expected acoustical noise of these small non-electric sensors.

This paper presents a theory to determine the acoustical noise of a piston transducer. The theory is based on full thermodynamic equilibrium conditions, which means that the noise power produced by the sensor itself must equal the power produced by the medium. In this way are we able to cross-check the power delivered by both mechanisms. The theory shows that the noise level is not only dependent on the surface area of the transducer, but that a factor is needed to correct for the piston behavior of the transducer when the radius a of the transducer's surface is small compared to the wavelength λ (i.e., $a/\lambda < 0.3$). Furthermore is it shown that due to this factor the acoustical noise induced by the medium converges to a finite value for transducers with a vanishing surface area.

This paper is organized as follows: We derive the theory in Section 6.2, where we start the analysis with a short overview of the derivation that is needed to determine the noise pressure at the transducer surface. Next we derive the noise power and the noise pressure due to the sensor and the medium, and we conclude that section with a description of the noise pressure levels. We show simulation results that describe the dependence of the acoustical noise on the ratio a/λ of the piston surface for our sensor. In Section 6.3 we will compare these noise pressure to the noise levels that can be obtained with conventional piezo-electric transducers based on a finite element model. We finalize this paper with conclusions in Section 6.4.

6.2 Theory

When a system is in full thermodynamic equilibrium with its surroundings at temperature T, no net power can flow between the system and the surroundings (Fig. 6.1a) [124]. If the system contains a damping element, it means that there is a mechanism for mechanical dissipation in that system. In that case the fluctuation-dissipation theorem [125] states that there will be a component of mechanical fluctuation in that system that is directly related to the dissipation. As a result of this theorem any mechanical system, no matter how complex, that is in full thermodynamic equilibrium, can be analyzed for mechanical-thermal noise by adding a noise force generator alongside each damping element [123]. In the equation of motion of our sensor the oscillation of the membrane is approximated by piston motion. Therefore only one damping mechanism is present, which represents the internal mechanical resistance against the oscillation of the membrane. In an equivalent circuit this mechanical sensor can be described as a damper with mechanical resistance R_M and a parallel force generator both connected to the piston (Fig. 6.1b). On the other hand, if the system is in contact with a surrounding medium via a membrane, molecular agitation against the membrane will be a second cause of noise (Fig. 6.1c). This kind of noise can be analyzed in a similar manner as the electrical noise received by an antenna. Because the sensor is in thermal equilibrium with the medium, the total spectral power received by the sensor from the medium must equal the spectral power delivered by its internal noise force generator to the medium [126]. Based on this principle we are able to check the noise power generated by both mechanisms. Next, we determine the noise pressure at the surface of the transducer. We start the analysis by determining the amount of noise power produced by the force generator in the noisy mechanical resistor (Sec 6.2.1), and the noise power density present in the medium (Sec 6.2.2). We proceed by calculating the mechanical radiation impedance of the piston and its effective area in reception (Sec 6.2.3). Then we determine the maximum amount of noise power that is collected by the sensor (Sec 6.2.4) and finalize by deriving the noise pressure present at the surface of the sensor (Sec 6.2.5).

6.2.1 Energy generated by the sensor

When the sensor is in thermal equilibrium with its surroundings at an absolute temperature T, there are intrinsic thermodynamic fluctuations present, which are described by the force generator alongside the damper. The magnitude of the mean square displacement fluctuations can be solved from the equipartition theorem [127, Ch. 7.5] which states that each independent quadratic term in the total energy of the system corresponds to a degree of freedom with a mean fluctuation energy equal to $k_B T/2$ where $k_B = 1.38 \times 10^{-23}$[J/K] is the Boltzmann constant. To determine the thermal agitation of the sensor we follow the Nyquist reasoning [126] for thermal agitation of electric charge in electrical resistors, but in our case we take two mechanical dampers.
Consider two dampers, each with a mechanical resistance R_M and the same temperature T, connected as indicated in Figure 6.2. Due to thermal agitation of

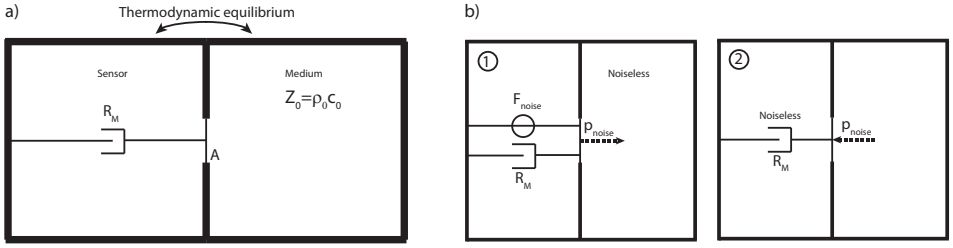

Figure 6.1: a) Sensor with a piston A and matched mechanical resistance R_M, in contact with a medium with impedance Z_0. The sensor and medium are contained in (large) cavities. The whole configuration is in full thermodynamic equilibrium at temperature T. The only thermodynamic connection between both sides is via the surface area A of the sensor. b) The system described for the two approaches; on the left (1) we consider the noise power produced by the intrinsic force generator and delivered to a noiseless medium and on the right (2) the noise power produced by the medium and received by the transducer with a noiseless mechanical resistance.

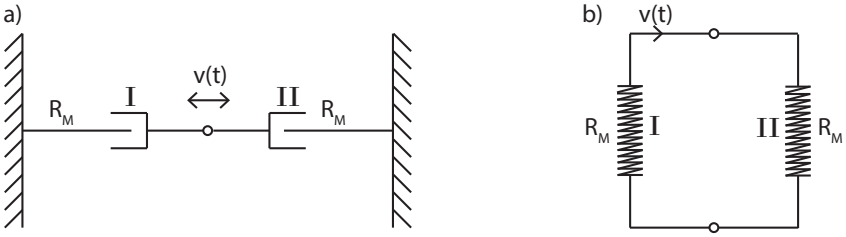

Figure 6.2: Scheme of two connected dampers I and II each with a mechanical resistance R_M. a) The mechanical network diagram of the two dampers fixed on one side and connected together on the other side. b) The equivalent network model.

damper 1 a force F generates a velocity v in damper 2. This velocity, obtained by dividing the force by 2 R_M, causes absorption of power in damper 2. This absorbed power is equal to the product of the mechanical resistance and the square of the velocity. So power is transferred from damper 1 to damper 2. In the same manner power is transferred from damper 2 to damper 1. Since the two dampers are at the same temperature it follows from the second law of thermodynamics that the power flowing in one direction is exactly equal to the power flowing in the other direction. This equilibrium condition holds for the power exchanged within any frequency band [126]. Hence the force is a universal function of frequency, mechanical resistance and temperature and of these variables only. To determine the form of this function we consider again the two dampers each of resistance R_M, but now connected via a long non-dissipative thin rod (Fig. 6.3). The length

of the rod is l, it has a density ρ, cross-section A and the velocity of propagation along the rod is defined as c. This rod has the same characteristic impedance $Z = R_M$ as the mechanical resistance so there is no reflection at either end of the rod. Let the absolute temperature of the system be T after thermal equilibrium has been established. We can describe the delivered power to the rod as two trains of energy traversing the rod. One train is traveling from left to right, being the power delivered by damper 1 and absorbed by damper 2. The other train is traveling in the reverse direction. At a certain instant after equilibrium has been established, we isolate the rod from the two dampers. Under these conditions there is complete reflection at the two ends of the rod and the energy which was on the rod at the time of isolation remains trapped. Now instead of describing the waves on the rod as two trains traveling in opposite directions we describe the rod as vibrating at its natural frequencies. The lowest frequency has a force node at each end and no intermediate nodes. The frequency corresponding to this mode of vibration is $c/2l$. The next higher natural frequency has a node at each end of the rod and one in the middle and is described by $2c/2l$. In this way there are natural frequencies at $3c/2l$, $4c/2l$, etc. Consider a frequency range extending from f cycles per second to $f + \Delta f$ cycles per second, i.e. a frequency range of width Δf. The number of modes of vibration, or degrees of freedom, lying within this range may be taken to be $2l\Delta f/c$, provided l is taken sufficiently large to make this expression a great number. Under this condition it is permissible to speak of the average energy per degree of freedom as a definite quantity. To each degree of freedom there corresponds an energy equal to $k_B T$ on the average, on the basis of the equipartition law: $1/2k_B T$ for the open-ended modes and $1/2k_B T$ for the fixed-ended modes. The total energy of the vibrations within the frequency interval Δf is then seen to be $2lk_B T\Delta f/c$. But since there is no reflection this is the energy within that frequency interval which was transferred from the two dampers to the rod during the time of transit l/c. The average power, transferred from each damper to the rod within the frequency interval Δf during the time interval l/c is therefore $k_B T\Delta f$. Therefore the maximal power that the sensor can deliver to the medium is

$$P_{\text{sens}} = k_B T\Delta f. \tag{6.1}$$

6.2.2 Energy present in the medium

In this analysis we want to determine the noise power density present in the medium. In the present case, the cavity is assumed to contain liquid with impedance Z_0 as indicated in Figure 6.1. The energy present in this cavity is determined by the thermal motion of the particles of the fluid. There are two types of atomic motion present in a liquid: phonon motion and diffusional motion [128]. The phonon motion consist of one longitudinal mode and may contain two transverse modes. Whether these transverse modes are present or not depend on the solid-like ability of liquids to support shear waves. This is indicated by the Frenkel frequency ω_F that is minimally needed to support those waves. The second atomic motion is the diffusional motion which happens when an atom is jumping between two equilibrium positions. Taking all possible motions into account, the

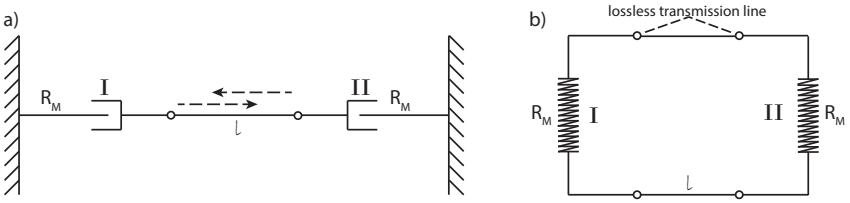

Figure 6.3: Scheme of two connected dampers with a mechanical resistance R_M and a long thin rod. a) The mechanical diagram of the two dampers fixed on one side and connected via a thin rod on the other side. b) The equivalent electrical network model. The rod translates to a lossless transmission line.

total energy present in the liquid can be described as

$$E = K_l + P_l + K_s(\omega > \omega_F) + P_s(\omega > \omega_F) + K_d + P_d, \tag{6.2}$$

where K is the kinetic energy and P the potential energy [128]. The subscripts define the three different motions with l the longitudinal mode, s the shear modes and d the diffusing atoms. This energy equation can be simplified because the energy of the diffusional motion is so low that it can be omitted. Furthermore, the frequency range of ultrasound sensors is much lower than the Frenkel frequency of water ($\sim 10^{11}$ Hz at 150 MPa) [128], which allows us to omit the shear phonons as well. Hence the only relevant energy left in the liquid is the longitudinal mode of phonon motion. The energy of the longitudinal mode in a liquid contains the same energy as a longitudinal mode in solid state physics [128–130]. Because the energy of longitudinal modes in solid state physics have been extensively described [131–133], we will assume that we can use this description to determine the energy in the medium. A practical justification for this assumption may be found in the abundant use of finite element and finite difference models for computing acoustic wave fields. In these models we use regular discrete grids to describe the wave propagation through a fluid. These models are thoroughly validated for frequencies in the MHz range. We see no reason to doubt that for computing noise in the same frequency range it is equally allowed to replace wave propagation through the continuous fluid medium by wave propagation through a regular grid. The latter is exactly what is considered in solid state physics.
The energy in the medium can be obtained via the vibrational modes of the corresponding system of particles. Similar to the description of the energy trapped in the rod, we will use standing waves as sums of traveling waves to describe the vibrational modes. The simplest system grid contains cubic cells with sides L. Whereas the traveling waves have positive and negative wave-vectors to describe their behavior, the standing waves consist of a superposition of two opposite traveling waves and can thus be described by only the positive wave-vectors [131]. Therefore the mode spectrum is represented in an octant of the three-dimensional $\vec{k}$-space as a simple cubic lattice with sides π/L. The wave-vector $\vec{k}$ is given by $\vec{k} = \hat{i}k_x + \hat{j}k_y + \hat{l}k_z$. The distance from each point to the origin is proportional to

the resonant frequency of the mode. The number of standing wave states inside a volume element $d^3\vec{k}$ in this octant of k-space is

$$\rho_s(\vec{k})d^3\vec{k} = \left(\frac{L}{\pi}\right)^3 d^3\vec{k} = \frac{V}{\pi^3}d^3\vec{k}, \tag{6.3}$$

where $V = L^3$ is the volume of the cubic cell and $\rho_s(\vec{k})$ is the density of states for standing waves in a three-dimensional crystal [131]. If we introduce spherical coordinates (θ, ϕ, k) and the number of standing wave states in a spherical shell between k and $k + dk$ we obtain

$$\rho_s(\theta,\phi,k)k^2\sin\theta dk d\theta d\phi \quad = \quad \frac{V}{8\pi^3}k^2\sin\theta dk d\theta d\phi = \frac{V}{8\pi^3}k^2 dk d\Omega, \tag{6.4}$$

where the factor $1/8$ is present to correct for the fact that the density is given for the entire space while in Eq.6.3 only positive k values were allowed. Moreover, $d\Omega = \sin\theta d\theta d\phi$ is the solid angle enclosed by θ and $\theta + d\theta$, and ϕ and $\phi + d\phi$.
The elementary vibrational disturbance of a lattice of atoms that uniformly oscillates at a single frequency is called a phonon in the quantum mechanical description. The quantum of energy of a phonon of frequency f is hf, where $h = 6.626 \times 10^{-34}$ [Js] is Planck's constant. The total energy of a particular vibrational mode is a multiplication of the average number of phonons per mode and the energy per phonon. The average number of phonons $\langle n\rangle$ per mode at temperature T is described by the Bose-Einstein factor as [131]

$$\langle n\rangle = \frac{1}{e^{(\frac{hf}{k_BT})} - 1}. \tag{6.5}$$

Therefore, the average energy per mode is given by

$$\langle \mathcal{E}\rangle = \langle n\rangle hf = \frac{hf}{e^{(\frac{hf}{k_BT})} - 1}. \tag{6.6}$$

With the known mode density of the system and the average energy per mode we are able to determine the total energy density of the system. The energy density (energy per unit volume) dU per solid angle in a band between k and $k + dk$ is given by the average energy per mode times the number of modes per solid angle and per unit volume as

$$dU(\theta,\phi,k) \quad = \quad \frac{hf}{e^{(\frac{hf}{k_BT})} - 1}\frac{k^2}{8\pi^3}dk. \tag{6.7}$$

We assume that $hf/k_BT \ll 1$ which is valid for frequencies below the GHz range. With this assumption the exponential $e^x = 1 + x/1! + x^2/2! + ...$ can be approximated as $e^{hf/k_BT} \approx 1 + hf/k_BT$. So below 1 GHz the energy density flowing within the cavity between f and $f + df$ is

$$dU(\theta,\phi,k) \approx k_BT\frac{k^2}{8\pi^3}dk. \tag{6.8}$$

The intensity per solid angle of the modes in a band dk is

$$d\vec{I}(\theta,\phi,k) = c_0 dU(\theta,\phi)\vec{e}_r = c_0 k_B T \frac{k^2}{8\pi^3} dk\vec{e}_r, \tag{6.9}$$

where $\vec{e}_r = \frac{\vec{k}}{|\vec{k}|}$ is the direction of the wave and c_0 is the speed of sound in the medium. We like to express dP with dependence on frequency f instead of k. Because $k = 2\pi f/c_0$, we obtain for the intensity

$$d\vec{I}(\theta,\phi,f) = k_B T \frac{f^2}{c_0^2} df\vec{e}_r = \frac{k_B T}{\lambda^2} df\vec{e}_r. \tag{6.10}$$

To describe the sound intensity that is produced by the medium we want to introduce the term loudness L. This loudness (in $\mathrm{Wm^{-2}sr^{-1}Hz^{-1}}$) is the spectral power density produced per solid angle and is thus given by

$$L(\theta,\phi,f) \quad = \quad \frac{k_B T}{\lambda^2}. \tag{6.11}$$

6.2.3 Radiated power from a piston

The connection between the mechanical resistor and the medium is made by the surface area of the sensor in the rigid baffle that separates both cavities in Figure 6.2. This connection has influence on the amount of energy that can travel from one side of the cavity towards the other side. From the mechanical resistor's side towards the medium this is indicated by the mechanical radiation impedance and from the medium towards the sensor this is indicated by an effective area of the surface. The formulation of both the mechanical radiation impedance and the effective area of the surface will be derived in this section.
When we have a piston surface S in a rigid baffle at $z = 0$, the energy that radiates into the medium can be determined by the Rayleigh integral. The pressure at constant frequency at any position (x, y, z) in the medium is given by

$$\hat{p} = \frac{-i\omega\rho}{2\pi} \iint_S \hat{v}_n(x_s, y_s) \frac{e^{ikR}}{R} dx_s dy_s, \tag{6.12}$$

where the hat indicates the complex amplitude of the quantity, $R = \sqrt{(x-x_S)^2 + (y-y_S)^2 + z^2}$, with x, y and z the coordinates in cartesian space with z directed perpendicular to the baffle. The subscript s denotes the source coordinates. The uniform normal velocity of the surface is denoted by v_n. We use the acoustic energy flux or acoustic intensity $\vec{I} = p\vec{v}$ to determine the time average power in the far field radiated from the source as [134]

$$P_{\mathrm{av}} = \iint_S \vec{I}_{\mathrm{av}} \cdot \vec{n}_{\mathrm{out}} dS, \tag{6.13}$$

where $\vec{n}_{\mathrm{out}}$ indicates the normal vector of the surface S. When we write the pressure p as $p = \mathrm{Re}\left\{\hat{p}e^{-i\omega t}\right\}$ and the velocity as $\vec{v} = \mathrm{Re}\left\{\vec{\hat{v}}e^{-i\omega t}\right\}$, the average product is given by

$$(p\vec{v})_{\mathrm{av}} = \frac{1}{2}\mathrm{Re}\left\{\hat{p}\vec{\hat{v}}^*\right\}. \tag{6.14}$$

Hence, the time average of the acoustic energy flux $\vec{I}_{\mathrm{av}}$ is given by

$$\vec{I}_{\mathrm{av}} = \frac{1}{2}\mathrm{Re}\left\{\hat{p}\vec{\hat{v}}^{*}\right\}. \tag{6.15}$$

We can now calculate the average power in the far field as

$$\begin{aligned} P_{\mathrm{av}} &= \frac{1}{2}\mathrm{Re}\left\{\iint_S \hat{v}_n^{*}\hat{p}dS\right\}, \\ &= \frac{|\hat{v}_n|^2}{2}\mathrm{Re}\left\{\frac{-i\omega\rho}{2\pi}\iint_S\iint_S \frac{e^{ikR}}{R}dx_s dy_s dxdy\right\}, \\ &= \frac{|\hat{v}_n|^2}{2}\mathrm{Re}\left\{Z_{\mathrm{m,rad}}\right\}, \end{aligned} \tag{6.16}$$

where $Z_{\mathrm{m,rad}}$ is the mechanical radiation impedance [134]. The radiation impedance is defined as the force $\hat{F}_z$ divided by the normal velocity $\hat{v}_n$. For a piston this is similar to the area integral of the specific radiation impedance $\hat{p}/\hat{v}_n$. The quadruple integral can be solved for a baffled circular piston resulting in a mechanical radiation impedance of

$$\begin{aligned} Z_{\mathrm{m,rad}} &= \frac{-i\omega\rho}{2\pi}\iint_S\iint_S \frac{e^{ikR}}{R}dx_s dy_s dxdy, \\ &= \pi a^2 Z_0\left[R_1(2ka) - iX_1(2ka)\right], \end{aligned} \tag{6.17}$$

with

$$R_1(2ka) = 1 - \frac{2J_1(2ka)}{2ka}, \quad X_1(2ka) = \frac{2H_1(2ka)}{2ka}. \tag{6.18}$$

The $J_1(\eta)$ and $H_1(\eta)$ are the Bessel function and the Struve function of first order [134] and a is the radius of the piston. So the radiated power from a circular piston with area $A = \pi a^2$ in a rigid baffle results in

$$P_{\mathrm{av}} = \frac{|\hat{v}_n|^2}{2}AZ_0R_1(2ka). \tag{6.19}$$

The radiated power can also be obtained from the maximum intensity $I_{\max}$ and the normalized radiation pattern $P_n(\theta,\phi)$ of the circular piston as

$$P_{\mathrm{av}} = \int_0^{2\pi}\int_0^{\pi/2} I_{\max}P_n(\theta,\phi)r^2\sin\theta d\theta d\phi. \tag{6.20}$$

The maximum intensity in the far field is given by

$$I_{\max} = \frac{1}{2}\mathrm{Re}\left\{\hat{p}_{FF}\hat{v}_{FF}^{*}\right\} = \frac{|\hat{p}_{FF}|^2}{2Z_0}. \tag{6.21}$$

For the pressure in the far field we can state that $z \gg x_S$ and $z \gg y_S$. Therefore Eq.(6.12) can be approximated as

$$\begin{aligned} \hat{p}_{FF} &= \frac{-i\omega\rho}{2\pi}\hat{v}_n\iint_S \frac{e^{ikz}}{z}dx_s dy_s, \\ &= \frac{-i\omega\rho Ae^{ikz}}{2\pi z}\hat{v}_n. \end{aligned} \tag{6.22}$$

We are only interested in the modulus of the field, which results in

$$|\hat{p}_{FF}| = \frac{Z_0 A}{\lambda z}|\hat{v}_n|. \tag{6.23}$$

When we substitute Eq.(6.23) and Eq.(6.21) into Eq.(6.20), we obtain for the radiated power

$$P_{\text{av}} = \frac{Z_0 A^2}{2\lambda^2}|\hat{v}_n|^2\Omega_A, \tag{6.24}$$

where

$$\Omega_A = \int_0^{2\pi}\int_0^{\pi/2} P_n(\theta,\phi)\sin\theta d\theta d\phi, \tag{6.25}$$

is known as the beam solid angle of the piston and is the integral over the normalized radiation pattern. Both calculated radiated powers in Eq.(6.19) and Eq.(6.24) should be the same and by equating we are able to find a relationship between the effective area of the piston, the wavelength and the radiation pattern as

$$\lambda^2 = A_{\text{eff}}\Omega_A, \tag{6.26}$$

where

$$A_{\text{eff}} = \frac{A}{R_1}. \tag{6.27}$$

The validity of this relationship can also be shown mathematically by solving the integral of the beam solid angle. With use of the far field approximation the pressure can be expressed in the form of an outgoing spherical wave and nonuniform directivity $D(\theta,\phi)$ according to

$$\hat{p} \approx D(\theta,\phi)\frac{e^{ikr}}{r}, \tag{6.28}$$

where

$$D(\theta,\phi) = \frac{i\omega\rho}{2\pi}\iint_S \hat{v}_n(x_s,y_s)e^{-k\vec{x}_s\cdot\vec{e}_r}dx_s dy_s, \tag{6.29}$$

and contains the two-dimensional Fourier transform of $\hat{v}_n(x_s,y_s)$. For a circular piston, $D(\theta,\phi)$ is only dependent on θ as [134]

$$D(\theta) = \frac{-i\rho c\hat{v}_n ka^2}{2}\frac{2J_1(ka\sin\theta)}{ka\sin\theta}. \tag{6.30}$$

Hence the normalized radiation pattern is given by

$$P_n(\theta,\phi) = \frac{|D(\theta,\phi)|^2}{\max\{|D(\theta,\phi)|^2\}} = \frac{2J_1(ka\sin\theta)}{ka\sin\theta}. \tag{6.31}$$

Therefore the effective area can be calculated with Eq.(6.26) using this relationship for the directivity

$$A_{\text{eff}} = \frac{\lambda^2}{2\pi\int_0^{\pi/2}\left[\frac{2J_1(ka\sin\theta)}{ka\sin\theta}\right]^2\sin\theta d\theta}. \tag{6.32}$$

This integral can be solved

$$\int_0^{\pi/2} \left[\frac{2J_1(ka\sin\theta)}{ka\sin\theta}\right]^2 \sin\theta d\theta = \frac{2ka - 2J_1(2ka)}{(ka)^3}, \tag{6.33}$$

which, in view of Eq.(6.18), results in

$$\begin{aligned} A_{\text{eff}} &= \frac{\lambda^2 (ka)^3}{2\pi\left[2ka - 2J_1(2ka)\right]} \\ &= \pi a^2 \frac{2ka}{2ka - 2J_1(2ka)} \\ &= \frac{A}{R_1(2ka)}. \end{aligned} \tag{6.34}$$

This confirms the validity of Eq.(6.27) for the specific case of a circular piston.

6.2.4 Energy collected by the sensor

In this section we want to determine the power that is maximally delivered by the medium to the sensor. The maximum delivered power to the surface area of the sensor is given by [135, 136]

$$P_{\text{med}} = \int_f^{f+\Delta f} A_{\text{eff}} \int_0^{2\pi}\int_0^{\pi/2} L(\theta,\phi,f) P_n(\theta,\phi)\sin\theta d\theta d\phi df. \tag{6.35}$$

Using Eqs.(6.11),(6.26) and (6.25) we obtain for the maximum delivered power

$$\begin{aligned} P_{\text{med}} &= \int_f^{f+\Delta f} \frac{\lambda^2}{\Omega_A}\frac{k_B T}{\lambda^2} \int_0^{2\pi}\int_0^{\pi/2} P_n(\theta,\phi)\sin\theta d\theta d\phi df, \\ &= k_B T \Delta f. \end{aligned} \tag{6.36}$$

We already mentioned that when the sensor is in full thermodynamic equilibrium with the medium the powers produced by the sensor and by the medium should be the same. We just determined the maximum power produced by the medium and collected by the sensor as $k_B T\Delta f$. We already determined the maximum power produced by mechanical resistor of the sensor as $k_B T\Delta f$ (Eq. (6.1)). So these two powers are indeed equal.

6.2.5 Noise induced pressure at the sensor

We use the derived maximum noise power generated by the sensor and by the medium to determine the noise pressure generated at the transducer surface. We draw two equivalent circuits corresponding to the two different noise mechanisms. The circuit containing the Nyquist spectral power produced by the mechanical resistor is shown in Figure 6.4a. It contains the mechanical impedance of the noiseless damper, the noise pressure source due to the force generator and the mechanical radiation impedance of the piston. The maximum noise power is delivered

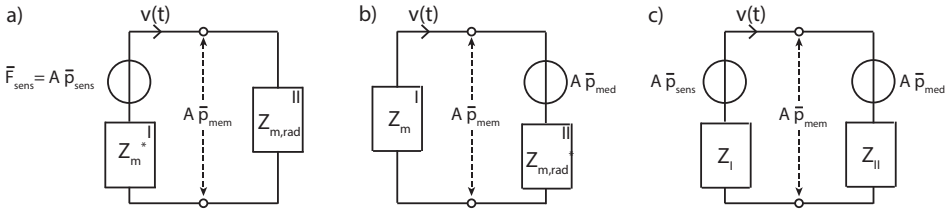

Figure 6.4: Equivalent circuit for a) a noisy transducer, b) a noisy medium, c) a realistic situation with a noisy transducer and a noisy medium. In this figure, all impedances are assumed noiseless.

when there is ideal coupling between the sensor and the medium, i.e. $Z_{\mathrm{m,rad}} = Z_m^*$. Based on this coupling we are able to determine the noise pressure source with use of the known power delivered to $Z_{\mathrm{m,rad}}$. This dissipated power is $k_B T \Delta f$ (Sec 6.2) and is equal to P_{II}. From this equation we can determine the noise source pressure $\bar{p}_{\mathrm{sens}}$ due to the sensor itself as

$$P_{\mathrm{sens}} = k_B T \Delta f = \frac{A^2 \bar{p}_{\mathrm{mem}}^2}{\mathrm{Re}\{Z_{\mathrm{m}}\}} = \frac{A^2 \bar{p}_{\mathrm{sens}}^2}{4\mathrm{Re}\{Z_{\mathrm{m}}\}} \tag{6.37}$$

$$\bar{p}_{\mathrm{sens}} = \frac{\sqrt{4 k_B T \Delta f \mathrm{Re}\{Z_{\mathrm{m}}\}}}{A}. \tag{6.38}$$

Here a bar is used to indicate the RMS value of a quantity.
The second equivalent circuit is shown in Figure 6.4b and contains the maximum radiation noise power delivered by the medium. Similar to the derivation above, the noise source pressure $\bar{p}_{\mathrm{med}}$ due to the medium is found as

$$P_{\mathrm{med}} = k_B T \Delta f = \frac{A^2 \bar{p}_{\mathrm{mem}}^2}{\mathrm{Re}\{Z_{\mathrm{m,rad}}\}} = \frac{A^2 \bar{p}_{\mathrm{med}}^2}{4\mathrm{Re}\{Z_{\mathrm{m,rad}}\}} \tag{6.39}$$

$$\bar{p}_{\mathrm{med}} = \frac{\sqrt{4 k_B T \Delta f \mathrm{Re}\{Z_{\mathrm{m,rad}}\}}}{A}, = \frac{\sqrt{4 k_B T Z_0 A R_1 \Delta f}}{A}. \tag{6.40}$$

The factor R_1 for piston motion is the main difference between our relation for the noise pressure of the medium and the method in the literature that just uses the specific acoustic impedance Z_0 of the medium. The influence of this factor is shown in Figure 6.5 where the noise pressure $\bar{p}_{\mathrm{med}}/\sqrt{\Delta f}$ is plotted against ka of our sensor. It is shown that both methods converge to the same value for elements with large ka values. This means that for transducer elements with $ka > 2$ the specific impedance can be used to determine the noise floor. When we have transducer elements with $ka < 1.9$ or $a/\lambda < 0.3$, both methods differ significantly. The method without factor R_1 goes to infinity while the method with the factor R_1

converges. The limiting value can be calculated with the expansion series of the Bessel function as [134]

$$J_1(\eta) = \frac{\eta/2}{(1!)^2} - \frac{2(\eta/2)^3}{(2!)^2} + \frac{3(\eta/2)^5}{(3!)^2} - \cdots \tag{6.41}$$

When we substitute Eq.(6.41) into Eq.(6.18) we obtain

$$R_1(2ka) = \frac{(2ka)^2}{4 \cdot 2} - \frac{(2ka)^4}{6 \cdot 4^2 \cdot 2} + \frac{(2ka)^6}{8 \cdot 6^2 \cdot 4^2 \cdot 2} - \cdots \tag{6.42}$$

For a circular piston with $ka \to 0$ the noise source pressure $\bar{p}_{\text{med}}$ converges to 0.3 mPa/$\sqrt{\text{Hz}}$.

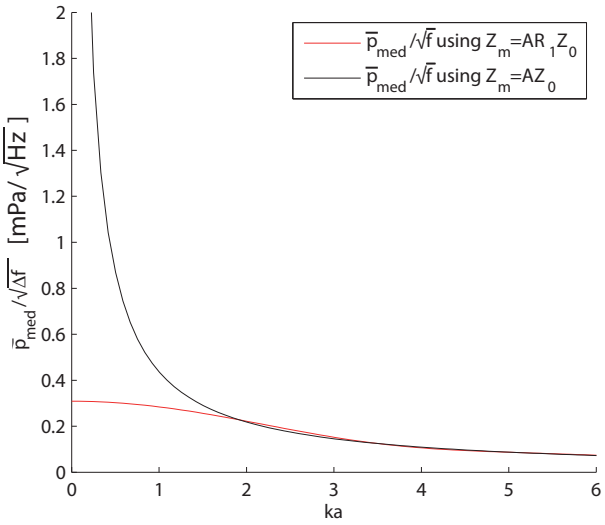

Figure 6.5: The noise source pressure $\bar{p}_{\text{med}}/\sqrt{\Delta f}$ versus ka for circular sensors with k the wavenumber and a the radius of the sensor. The black curve is the noise pressure based on the impedance of water and the surface area of the sensor while the red curve is calculated with use of an extra factor R_1 that corrects for the radiation behavior of the piston.

In reality, noise is caused by both the medium and the sensor itself. The equivalent circuit of a real case is shown in Figure 6.4c. Because the noise sources are uncorrelated we can not add the pressures but need to add the corresponding powers in the circuit. Hence the pressure at the surface $\bar{p}_{\text{med}}$ of the transducer is given by

$$\bar{p}_{\text{mem}} = \sqrt{\left(\frac{\bar{p}_{\text{sens}}|Z_{II}|}{|Z_I + Z_{II}|}\right)^2 + \left(\frac{\bar{p}_{\text{med}}|Z_I|}{|Z_I + Z_{II}|}\right)^2}, \tag{6.43}$$

$$= \frac{\sqrt{4k_B T \Delta f}}{A}\sqrt{\frac{R_I|Z_{II}|^2}{|Z_I + Z_{II}|^2} + \frac{R_{II}|Z_I|^2}{|Z_I + Z_{II}|^2}}. \tag{6.44}$$

The real and imaginary parts of Z_I follow from the construction of the sensor, and the real and imaginary parts of Z_{II} follow from Eqs. 6.17 and 6.18. Depending on the relative magnitude of Z_I, we can distinguish the following cases:

- If $|Z_I| \gg |Z_{II}|$ we have a very stiff transducer, and this wil result in

$$\bar{p}_{\text{mem}} = \bar{p}_{\text{med}}. \tag{6.45}$$

  In this case the noise from the medium is dominant.

- If $|Z_I| \ll |Z_{II}|$ we have a very compliant transducer, and this will give

$$\bar{p}_{\text{mem}} = \bar{p}_{\text{sens}}. \tag{6.46}$$

  In this case the noise from the sensor is dominant. If $ka < 1$, then $|Z_I| \ll |Z_{II}|$ implies that $R_I \ll R_{II}$, and we will have

$$\bar{p}_{\text{sens}} \ll \bar{p}_{\text{med}}. \tag{6.47}$$

To summarize, $\bar{p}_{\text{med}}$ can be regarded as the upper limit of the total acoustical noise of a sensor.

6.3 Piezo-electric model

With the derived theory we are able to investigate the contribution of the acoustical noise due to the medium to the total noise of a piezo-electric ultrasound transducer. We made a finite element model that can be used to calculate the expected noise floor and mechanical radiation impedance. This section first describes the model (Sec. 6.3.1) and then presents the results (Sec.6.3.2).

6.3.1 Model description

We made a 2D and 3D finite element model in PZFlex (Weidlinger Associates, UK). The 2D model is made to determine the electrical impedance of the transducer and to determine the sensitivity as there is no significant difference compared to the 3D model while having a much faster calculation time. The 3D model is used to calculate the mechanical radiation impedance. The geometry of the transducer is similar in both models and will be described first. The piezo-electric element is optimized for a resonance frequency around 0.8 MHz, which is comparable to one of our opto-acoustical sensors. The transducer has a square surface with a similar area as the circular sensor. The width x_{width} of the square element is each time calculated as $x_{\text{width}} = \sqrt{a^2\pi}$, with a the radius of the circular sensor. In the 2D model there is an option to scale the electrode in such way that a square element is obtained. The design of the transducer is similar to the one used in Ref [92] except for the backing layer which is changed into an electrical conducting glue. The stack of the transducer starts with a 120 μm backing layer followed by a 1.6 mm piezo-electric layer and a 350 μm matching layer. The width of the entire stack x_{width} is each time varied and runs from 85 μm to 2.54 mm corresponding

to a ka of 0.2 to 6 respectively. The transducer is loaded with water or void.
For the electrical impedance we first determine the resonance frequency of the transducer by excitation of the piezo-electric element with a 90 ns pulse. With this short pulse we are able to excite all frequencies of interest. At resonance we determine the electrical impedance. We need to determine the sensitivity of the transducer to be able to translate the electrical impedance to a noise pressure. We transmit a 3-cycle sinusoid acoustical plane wave with center frequency of 1 MHz through the water and measure the induced voltage on the electrode of the sensor. We divide the peak to peak value of the voltage by the peak to peak value of the pressure at the surface of the transducer to find the sensitivity.
The mechanical radiation impedance is obtained with the 3D model. We used the method of Ref. [137] and excite the transducer with a 3-cycle sinusoid with 1 MHz center frequency. We compute the average pressure and the average velocity over the surface of the transducer. The modulus of the maximum of the average pressure divided by the maximum of the average velocity is computed. We calculate the relative radiation impedance by dividing this modulus by the specific acoustic impedance of water, which is 1.5 MRayl.

6.3.2 Modeling results

First we determined the electrical impedance of the transducer for several ka values by changing the width of the transducer. We modeled two cases; an unloaded transducer and a water loaded transducer. The difference in the electrical impedance between the two models is the addition of a contribution due to the acoustic radiation impedance. The results are shown in Figure 6.6a. It can be seen that the curves are quite similar. At higher ka values ($ka > 2$) the electrical impedance has the same order of magnitude and for lower ka values ($ka \leq 2$) the electrical impedance with air loading is a little bit lower than the electrical impedance of the water loaded transducer. It can also be seen that the electrical impedance goes to infinity for small ka numbers.
We also determined the relative radiation impedance in a 3D model. Figure 6.6b shows the modeling results compared to the analytical relative radiation impedance where we plotted $|Z_{\mathrm{m,rad}}/\pi a^2 Z_0|$ for the analytical radiation impedance and performed the same corrections for the modeling results. The curves are rather similar. One difference between the two curves may be explained by the fact that the analytical radiation impedance is obtained for a circular piston while the surface element of the model is rectangular. Another explanation for the higher value is the fact that the element is not positioned in a rigid baffle, as is the case in the analytical solution, but has a void next to it. The last comment that can be made about the higher values for larger ka is the fact that ideal piston motion is no longer occuring. In the regime where $ka > 1.6$ piston motion is no longer guaranteed as can be seen in the motion pattern of the model. For the larger ka values second and even third order vibrations of the surface are visible.
We are able to determine the noise pressure of the transducer based on the electrical impedance when we know its sensitivity. We can use the Johnson-Nyquist noise

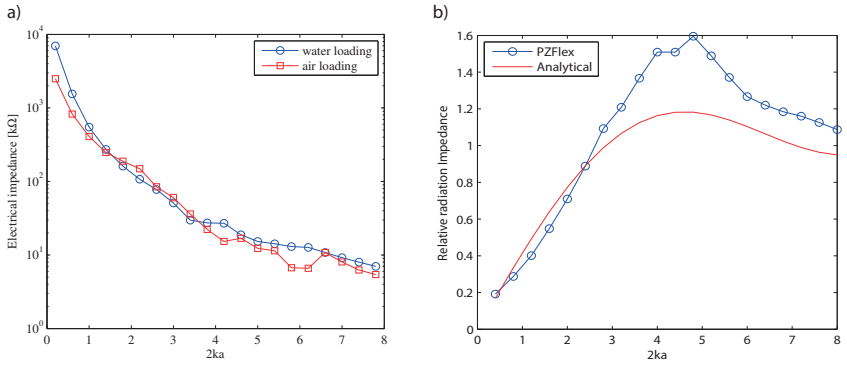

Figure 6.6: The electrical impedances of a piezo-electric transducer for different ka values. a) The electrical impedance for a water loaded (blue) and air loaded (red) transducer. b) The acoustical relative radiation impedance of the transducer with in blue the modeling results of a square element and in red the analytical solution of a circular piston. Both curves show the absolute relative radiation impedance and are corrected for the surface area of the element and the specific acoustic impedance of water.

of a resistor which will result in noise voltages of

$$V_{\text{noise}} = \sqrt{4k_B T R}, \tag{6.48}$$

where $R = \text{Re}\{Z_{\text{elec}}\}$. With the sensitivity of the transducer in volts per pascal we can determine the equivalent noise pressure. We determined the sensitivity and the results for $ka \leq 2$ are listed in Table 6.1. It can be seen that the sensitivity has a maximum when $ka = 1.4 - 1.6$. The resulting noise pressures $\bar{p}_{\text{mem}}/\sqrt{\Delta f}$ for a piezo-electric transducer are shown in Figure 6.7. The curve shows higher equivalent pressure values than the sensor noise pressure which is estimated at $\bar{p}_{\text{med}}$ because we assume that a PZT transducer is relatively stiff. The differences in Figure 6.7 are expected because of the extra electrical noise in the PZT transducer. Furthermore, the trend seems similar to the curve where the specific acoustic impedance Z_0 is used without R_1 which hence goes to infinity.

6.4 Discussion

In this paper we derived the acoustical noise pressure at the surface of a transducer. We showed that for smaller elements an extra factor is needed to take radiation effects into account. This factor ensures that for sensors with element areas with a $ka < 2$ the medium noise converges. For a sensor with a circular surface the limit of the noise pressure due to molecular agitation in the fluid is 0.3 mPa/$\sqrt{\text{Hz}}$. This means that from the total noise level of our sensor with $ka < 1$ and a bandwidth of 1 MHz, a maximum of 0.3 Pa is noise that can be assigned to noise contributions

Table 6.1: Modeling results of a piezo-electric transducer. The first column list the ka value of the transducer, the second and third column list the electrical impedance of the loaded and unloaded transducer respectively and the last column contains the sensitivity values.

ka	impedance with water $k\Omega$	impedance with air $k\Omega$	sensitivity μV/Pa
0.2	6980	2496	27
0.4	1550	825	40
0.6	550	408	51
0.8	272	248	58
1.0	162	189	64
1.2	107	149	68
1.4	78	85	72
1.6	51	60	72
1.8	30	36	71
2.0	27	22	66

from the medium and from the mechanical system of the sensor.
Although this theory is different from the acoustical literature its derivation is partially similar to the one used in radio astronomy. In radio astronomy antennas are used to detect signals from outside the atmosphere of the earth to study celestial objects at the radio frequencies. Noise is an important factor in this field and we followed the same methodology to derive the theory. Based on thermodynamic equilibrium noise contributions of the antenna and environment are determined and matched. Because antennas often have no clear physical area they use the effective area as measure for the effectiveness of the antenna. We used the effective area in the same manner to take piston motion into account which influences the effectiveness of the surface element.
It is clear that the derived noise level is of importance for mechanical sensors without electrical noise. To relate the noise pressure of mechanical sensors to noise pressures of sensors with an electrical system we modeled a PZT-transducer with thickness mode vibrations. The results suggest that the contribution from electrical noise in small piezo-electric transducers is dominant. It is also shown that when the corresponding noise pressures are obtained, the electrical impedance yields a trend similar to the acoustical impedance without the R_1 factor, but with higher values.
We may conclude from the noise pressure curve of piezo-electric transducers that there is no use in building piezo-electric sensors with $ka < 1$ as the noise pressure level goes rapidly up due to the increase of the dominant electrical impedance. An advantage of opto-mechanical transducers is that these devices are still able to detect low noise pressures while having surface elements with very low ka values.

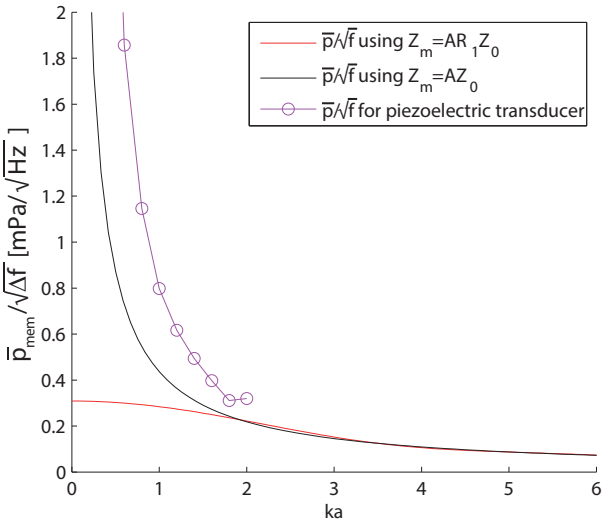

Figure 6.7: The noise pressure levels versus ka of the example PZT transducer. The black curve shows the acoustical noise pressure from the medium, as based on the impedance of the water and surface area of the sensor; the red curve is the acoustical noise pressure calculated with use of an extra factor R_1 that corrects for piston motion and the margenta curve is the total noise pressure obtained with the finite element model. This noise pressure is based on the electrical impedance of the transducer and hence contains the electrical noise and the acoustical noise. The sensitivity of the transducer is used to determine the corresponding noise pressure.

Chapter

7

Conclusions and discussion

We demonstrated that silicon micro-ring resonators are sensitive to strain and when they are integrated on an acoustical membrane can be used to sense ultrasound. In this thesis we mainly focused on the use of this sensor in medical applications, but the sensor can also be optimized for other applications such as the oil and gas markets. In medical procedures it is an advantage that the sensor is not susceptible to electromagnetic disturbance and hence can be used in combination with MRI. An other important benefit is the safety during medical procedures. Because the sensor is not electrically driven, safety concerns like high voltages or leakage currents are not present. A main benefit in the fabrication process of the sensor is the use of CMOS technologies that allow for ease of production and do not pose design limitations on the device.
In this section we will discuss the feasibility (Sec. 7.1) and prospects (Sec. 7.2, Sec. 7.3) of this ultrasound sensor in medical diagnostics. We will also discuss the use as temperature sensor (Sec. 7.4) and static pressure sensor (Sec. 7.5). We finalize this Chapter with a discussion about the noise pressure levels of small sensors (Sec. 7.6).

7.1 Feasibility of the sensor

We designed, fabricated and characterized an ultrasound sensor that is based on integrated photonics. The prototype consist of a 220 nm high silicon photonic ring-resonator (spatial footprint: 10 μm by 50 μm) integrated on an acoustically tuned silicon dioxide circular membrane (124 μm diameter, 2.5 μm thick). The ultrasound sensor has a resonance frequency of 0.76 MHz with a -6 dB bandwidth of 20 %. The noise equivalent pressure of 0.4 Pa is slightly better than the state-of-the-art ultrasound transducers with the same resonance frequency, while these

have a 65 times larger spatial footprint (Sec. 4.3). The vibrometer measurements (Sec. 5.5.3) show that the optical intensity modulation corresponds with the oscillation of the membrane and that there is no significant oscillation present in the silicon chip. Furthermore it is shown that the fabrication process is reproducible, hence a second sensor with similar membrane diameter will have a similar resonance frequency.
The sensor is interrogated by use of a laser and a photoreceiver. The wavelength of the laser is chosen such that it is positioned on the flank of a resonance dip of the ring resonator. In this way, a shift in optical resonance translates into a modulation of the light intensity at that particular wavelength. The noise equivalent pressure of 0.4 Pa corresponds to a minimal detectable wavelength shift of 29 fm. As this is the first prototype there is a lot of room for improvement of the sensor for each specific application. The most important adjustment, needed for almost every application, is addition of absorbing layers or other adjustments to the membrane to increase the bandwidth. Improvement of the bandwidth directly means that the Q-factor of the sensor has to be decreased, i.e. the increase in bandwidth is at the cost of its sensitivity. But there is also room to increase the sensitivity of the sensor. As a first step, the ring resonator can be optimized to the strain distribution of the membrane. One can think of racetracks positioned in a smaller area in the center with on average higher strain values or on the opposite by using larger rings exactly positioned on the edge of the membrane. Furthermore it is possible to enhance the induced strain in the membrane by optimizing the design of the membrane itself. By locally adding or removing layers of the membrane it may be possible to design a shape that contains areas that act as a mechanical strain amplifier.
When the application allows a lower sensitivity than the current 0.4 Pa, there is also the option of increasing the bandwidth by using the frequencies below the resonance frequency of the sensor. The curve of the transfer function (Fig. 4.5) is much flatter below the resonance frequency, resulting in a broader bandwidth. With a value of -17 dB this corresponds to a noise level of 2.8 Pa.
The resonance frequency of the current OMUS is comparable with that of the photo-acoustic breast tomography sensor used as comparison in Chapter 4, but needs to be increased for almost all other medical applications. This can be achieved by further reduction of the membrane diameter. Reducing the radius of the membrane results in an increase of the resonance frequency as is shown in Sec. 2.2.2 for a membrane diameter of 100 μm with the higher resonance frequency of 1.05 MHz. Other options to increase the resonance frequency are an stiffer membrane or different membrane shape.
The dynamic range of the OMUS is limited to low pressures as is shown in Figure 4.6 by the deviation from the linear curve. The vibrometer measurements show that this limitation is due to the interrogator and not due to a nonlinear response of the membrane (Sec. 5.5.3). Hence the dynamic range of the sensor could be drastically increased when we use a similar interrogator system as the one used by Rosenthal *et al* [68], where the resonance dip is tracked instead of the intensity modulations at a single wavelength.
We can conclude that the OMUS is applicable as ultrasound sensor. Even while

this sensor is not optimized for a specific application, but designed to be comparable to models and to assess robustness with fabrication, it is already very sensitive with a noise equivalent pressure of 0.4 Pa. The sensor can easily be improved for a specific application and has enough options as described above to implement these improvements.

7.2 Matrix probe

There are two medical imaging applications where the OMUS has most added value in view of the design requirements of the probe. The first application is TransEsophageal Echocardiography (TEE) in which the heart is imaged with a probe located inside the esophagus. In ideal situations the probe is inserted via the nose, which limits the volume of the head of the probe to around 1 cm^3 [138]. The second application is Intravascular Ultrasound (IVUS) where an ultrasound probe mounted on a catheter is inserted into the coronary artery to image the artery wall and determine the amount of atheromatous plaque. In this case the outer diameter of the probe is limited to 1 mm [139].
In both cases the spatial footprint of the probe is limited, while a dense matrix array is required to obtain real-time 3D images [4]. There are many different ways to design such an array, but Raghunathan *et al.* [138] show that a matrix design with a good radiation pattern and fast acquisition options consist of a few transmit elements, located in the middle of the array, and many receiver elements around. By repeating one sensor of the OMUS we should be able to build a very sensitive matrix sensor with high potential for imaging applications in IVUS and TEE. With TEE we have the option to build this array of sensors as TEE probe and transmit the acoustical pulse from the outside with a conventional ultrasound transducer. The other option, which is also needed for IVUS, is to integrate a few piezoelectric elements on the chip to transmit the beam.
The array should contain an incoming bus waveguide with passive optical demultiplexers that convert the wide spectrum of each bus waveguide into many small spectrum channels. We can obtain the spectrum for each ring resonator with grating couplers [76]. These grating coupled ring resonators allow coupling of only one particular resonance peak per ring. The spectrum of the outgoing bus waveguide is created with a multiplexer that successively stacks the modulated spectra of as many sensors as possible back into the available wide spectrum. The membranes positioned underneath the ring resonators can be created using dry etching or other techniques [84]. The current interrogator system should be changed into one that is capable of tracking the different resonant dips of all the successive ring resonators. Hence the ideal interrogator is capable to interrogate one or more channels where each channel contains several peaks. Technobis (Alkmaar, The Netherlands) already fabricated an interrogator named the LadyGator that is capable of simultaneously interrogating 6 channels with a resolution of 1 fm wavelength shift and maximum interrogation speed of 2 MHz.
When we have an array of sensors we are able to solve the limited bandwidth of the current sensor by designing membranes with successive resonance frequencies

as is done in some pMUT designs [62, 140, 141].
Although the integrated photonics and membranes are small enough to meet the design requirements of a possible matrix array, the current packaging is not. It is possible to package the chip with use of a fiber facet connected directly to the waveguide that fits the outer dimensions for IVUS, as is shown by Rosenthal *et al.* [68].

7.3 Photoacoustics

Another interesting field of application is photoacoustics. Not only can photoacoustics be used to image, but it can also provide functional information in the form of blood oxygenation, blood flow and temperature [142,143]. It combines the high-contrast and spectroscopic-based specificity of optical imaging with the high spatial resolution of ultrasound imaging, and has a greater penetration depth than purely optical imaging modalities [143]. With this technique tissue is irradiated with short light pulses. Due to the transient thermo-elastic expansion of the irradiated tissue, wideband ultrasonic waves are generated. The frequency range of photoacoustic waves is inversely proportional to the dimensions of the absorbing volume. The local optical energy deposition is wavelength dependent due to the wavelength dependent absorption coefficient of tissue and determines the magnitude of the wave. The photoacoustic waves hence contain physiologically specific information which is not present in normal ultrasound images. Due to the ANSI standards [144] only a limited amount of energy can be deposited in the human body, which results in a maximum inducible pressure. This is different from ultrasound images where the pressure of the acoustic wave is set by the transducer. Normal pressure with photoacoustics are in the order of kPa due to an increase in temperature in the range of mK [5, 145]. This pressure can be easily detected with our sensor.
Only the addition of a light source is required to use our OMUS for photoacoustic imaging. Polymer ring resonators as well as a Fabry-Perot optical interferometers have already been tested for future use in photoacoustics [146, 147]. They both use external sources and illuminate the object from a different position than the sensor. In some imaging systems this light source is separated from the sensing device [143], but for other applications like intravascular photoacoustics we need to integrate the light source with the sensor. The absorption spectrum of the tissue of interest has its wavelength between 400 nm and 1300 nm for lipid, collagen and elastin [145]. Therefore the silicon waveguide can not be used as light source because it only supports propagation of light waves with wavelengths around 1.55 μm [15]. Hence an additional fiber is needed to radiate the light. From the integration of an optical fiber and a state-of-the-art IVUS transducer [142,148,149] it can be concludedd that it is possible to integrate our sensor with a light source in the same manner.

7.4 Temperature sensor

We studied the response of the sensor to temperature. This behavior is well described in literature and our measurements show similar results. The optical waveguide is very sensitive to temperature changes with an optical wavelength shift around 80 pm/°C. With its linear temperature response, the sensor can be used for accurate measurements of changes in temperature.
The sensitivity to temperature changes may be of interest in the field of hyperthermia therapy where specific parts of the body are heated to kill or damage tumor tissue or to make this more susceptible to ionizing radiation or chemotherapy [150, 151]. When ultrasound is used to monitor the temperature, our sensor can be used, next to the imaging, for extra local measurement of the temperature at the position of the sensor. Because the temperature during treatment changes slowly compared to the fast ultrasound waves, the slow translation of the resonance dip can be used to determine the change in temperature and the fast modulation on this translation can be applied to image ultrasound pressure waves.

7.5 Strain sensor and pressure sensor

We studied the effect of pure bending on the optical racetrack resonators. We found that three different physical aspects have influence on the final shift in resonance wavelength: elongation of the waveguide, change in effective index of the waveguide, and dispersion. The effect of the strain-induced increase in track circumference and the effect of the strain-induced change in waveguide effective index oppose each other, where the first effect is three times larger than the latter. The strong dispersion in silicon sub-wavelength waveguides (400 nm by 220 nm) accounts for a decrease in sensitivity of about a factor two. The shift in resonance wavelength per applied strain is dependent on the width of the waveguide and the orientation of the silicon crystal and varies between 0.5 and 0.75 pm/microstrain for infrared light around 1550 nm wavelength. We have studied elongations up to 275 microstrain, and observed a linear relation between the resonance wavelength and the applied strain, which makes the silicon racetrack resonators suitable as strain sensors.
With the knowledge of this linear behavior we investigated the response of the sensor to a static loading. Therefore we created a membrane around one of the racetrack resonators. This membrane changed the circumstances of the measurements completely. First, the case of pure bending has changed into an applied strain due to deformation of the membrane under static loading. This means that the strain is present in the radial direction of the membrane and hence is no longer aligned with the direction of the racetrack. Second, we found that the chip has internal strain. A part of this strain is released by the initial deformation of the membrane. With the static measurements, we showed that these two effects have a major influence on the measurement results as they describe a non-linear response to the applied pressure. Hence our sensor is at this moment less suited as pressure sensor. We know from literature that linear responses can be obtained when thicker membranes are used [120, 152].

7.6 Noise pressure level of sensors with a small spatial footprint

We wanted to determine the absolute noise floor of our newly developed optical micro-machined ultrasound sensor. We already measured a noise pressure of 0.4 Pa and found that this is a much lower value than the theoretical noise pressure levels obtained from literature, which go to infinity when the radius of the membrane goes to zero. Therefore we derived a theory to determine the acoustical noise for sensors with a small spatial footprint. With this theory we showed that the acoustical noise pressure levels of all sensors converge for a vanishing aperture. The difference between our theory and the one described in literature is an extra factor that accounts for the radiation effects of the surface.
When we calculate the acoustical noise floor for our sensor using a bandwidth of 20%, we obtain a maximum pressure level of 0.13 Pa that can be assigned to noise contributions from the medium and from the sensor itself. This means that with our first sensor design we are already able to measure a pressure level that is very close to the pressure level of internal noise contribution values from the sensor and surroundings. With further optimization of the interrogating system it may be possible to reach this acoustical noise contribution level.
We also showed that the acoustical noise pressure level can never be obtained with a piezo-electric sensor with similar ka values as the electrical impedance goes to infinity when the aperture becomes zero, i.e. $ka \rightarrow 0$. As a result these optical micro-machined sensors can uniquely be used to detect pressure waves using apertures with a small diameter compared to the wavelength of the pressure wave.

Bibliography

[1] T. L. Szabo, *Diagnostic ultrasound imaging: inside out*, 2nd ed. Academic Press, 2014.

[2] R. Cobbold, *Foundations of Biomedical Ultrasound*. USA, New York: Oxford Univ. Press, 2007.

[3] W. D. O'Brien Jr, "Assessing the risks for modern diagnostic ultrasound imaging," *Japanese journal of applied physics*, vol. 37, no. part 1, pp. 2781–2788, 1998.

[4] A. Fenster, D. B. Downey, and H. N. Cardinal, "Three-dimensional ultrasound imaging," *Physics in medicine and biology*, vol. 46, no. 5, p. R67, 2001.

[5] P. Khuri-Yakub, Ö. Oralkan, and A. Nikoozadeh, "Innovations in ultrasound instrumentation for image guidance," in *Intraoperative Imaging and Image-Guided Therapy*. Springer, 2014, pp. 163–171.

[6] (2017, March) New 3d/4d ultrasound provides detailed images of fetuses. Women's Care, obstetrics & gynecology. [Online]. Available: https://www.womenscare.com/news/new-3d4d-ultrasound-provides-detailed-images-of-fetuses/

[7] (2017, March) Two cases of acute myocarditis with multiple intracardiac thrombi: the role of hypercoagulable state. Heart Views. [Online]. Available: http://www.heartviews.org/article.asp?issn=1995-705X;year=2014;volume=15;issue=1;spage=22;epage=25;aulast=Atas

[8] (2017, March) Necrotic core thickness and positive arterial remodeling index:emergent biomechanical factors for evaluating the risk of plaque rupture. Americal Journal of physiology, heart and circulatory physiology. [Online]. Available: http://ajpheart.physiology.org/content/295/2/H717

[9] (2017, March) Medical physics - ultrasound. Andrew Simmons 11B. [Online]. Available: http://www.genesis.net.au/~ajs/projects/medical_physics/ultrasound/

[10] W. Westerveld, "Silicon photonic micro-ring resonators to sense strain and ultrasound," 2014.

[11] F. Idachaba, D. U. Ike, and O. Hope, "Future trends in fiber optics communication," in *World Congress on Engineering London July*, 2014.

[12] (2016, June) The history of the integrated circuit. Nobelprize.org. Nobel Media AB. [Online]. Available: http://www.nobelprize.org/educational/physics/integrated_circuit/history/index.html

[13] D. J. Griffiths, *Introduction to Electrodynamics*, third, international ed. New Jersey: Preice-Hall Inernational, Inc, 1999.

[14] W. J. Westerveld, S. M. Leinders, K. W. van Dongen, H. P. Urbach, and M. Yousefi, "Extension of marcatili's analytical approach for rectangular silicon optical waveguides," *Journal of Lightwave Technology*, vol. 30, no. 14, pp. 2388–2401, 2012.

[15] W. Bogaerts, "Nanofotonische golfgeleiders en fotonische kristallen in silicium-op-isolator," Ph.D. dissertation, Ghent University, 2004.

[16] A. Yariv, "Universal relations for coupling of optical power between microresonators and dielectric waveguides," *Electronics Letters*, vol. 36, no. 4, pp. 321–322, 2000. DOI:10.1049/el:20000340

[17] S. Timoshenko, S. Woinowsky-Krieger, and S. Woinowsky-Krieger, *Theory of plates and shells*. McGraw-hill New York, 1959, vol. 2.

[18] K. F. Graff, *Wave motion in elastic solids*. Oxford university press, 1975.

[19] A. W. Leissa, *Vibrations of plates*. Scientific and Technical Information Division, Office of technology utilization, national aeronautics and space administration, 1969.

[20] M. KWAK, "Vibration of circular membranes in contact with water," *Journal of sound and vibration*, vol. 178, no. 5, pp. 688–690, 1994.

[21] W. J. Westerveld, J. Pozo, P. J. Harmsma, R. Schmits, E. Tabak, T. C. van den Dool, S. M. Leinders, K. W. A. van Dongen, H. P. Urbach, and M. Yousefi, "Characterization of a photonic strain sensor in silicon-on-insulator technology," *Optics Letters*, vol. 37, pp. 479–481, Feb 2012.

[22] A. A. Barlian, W.-T. Park, J. Mallon, A. Rastegar, and B. Pruitt, "Review: Semiconductor piezoresistance for microsystems," *Proceedings of the IEEE*, vol. 97, no. 3, pp. 513–552, Mar. 2009. DOI:10.1109/JPROC.2009.2013612

[23] P. Muralt and J. Baborowski, "Micromachined ultrasonic transducers and acoustic sensors based on piezoelectric thin films," *Journal of Electroceramics*, vol. 12, no. 1-2, pp. 101–108, 2004.

[24] P. Dumon, W. Bogaerts, A. Tchelnokov, J.-M. Fedeli, and R. Baets, "Silicon nanophotonics," *Future Fab International*, vol. 25, pp. 29–36, Apr. 2008.

[25] J. Pozo, P. Kumar, D. M. R. Lo Cascio, A. Khanna, P. Dumon, D. Delbeke, R. Baets, M. Fournier, J.-M. Fedeli, L. Fulbert, L. Zimmermann, B. Tillack, H. Tian, T. Aalto, P. O"Brien, D. Deptuck, J. Xu, X. Zhang, and D. Gale, "Essential: Epixfab services specifically targeting (sme) industrial takeup of advanced silicon photonics," in *Transparent Optical Networks (ICTON), 2012 14th International Conference on*, 2012, pp. 1–3. DOI:10.1109/ICTON.2012.6254391

[26] D. Taillaert, W. Van Paepegem, J. Vlekken, and R. Baets, "A thin foil optical strain gage based on silicon-on-insulator microresonators," in *Proc. SPIE*, vol. 6619, 2007, p. 661914. DOI:10.1117/12.738412

[27] W. J. Westerveld, J. Pozo, P. J. Harmsma, R. Schmits, E. Tabak, T. C. van den Dool, S. M. Leinders, K. W. van Dongen, H. P. Urbach, and M. Yousefi, "Characterization of a photonic strain sensor in silicon-on-insulator technology," *Optics Letters*, vol. 37, no. 4, pp. 479–481, Feb. 2012. DOI:10.1364/OL.37.000479

[28] X. Zhao, J. M. Tsai, H. Cai, X. M. Ji, J. Zhou, M. H. Bao, Y. P. Huang, D. L. Kwong, and A. Q. Liu, "A nano-opto-mechanical pressure sensor via ring resonator," *Optics Express*, vol. 20, no. 8, pp. 8535–8542, Apr. 2012. DOI:10.1364/OE.20.008535

[29] E. Hallynck and P. Bienstman, "Integrated optical pressure sensors in silicon-on-insulator," *Photonics Journal, IEEE*, vol. 4, no. 2, pp. 443–450, Apr. 2012. DOI:10.1109/JPHOT.2012.2189614

[30] S. M. C. Abdulla, P. J. Harmsma, R. A. Nieuwland, J. Pozo, M. Lemmen, H. Sadeghian, J. H. van den Berg, P. Bodis, and P. Buskens, "Soi based mechano-optical pressure sensor using a folded microring resonator," in *Proc. 9th Nanomechanical sensing workshop, NMC 2012*, Mumbai, India, Jun. 2012, pp. 80–81.

[31] C. D. Liapis, K. Balzer, F. Benedetti-Valentini, and J. Fernandes e Fernandes, *Vascular Surgery*, ser. European Manual of Medicine. Berlin: Springer, 2007.

[32] C. L. de Korte, H. H. G. Hansen, and A. F. W. van der Steen, "Vascular ultrasound for atherosclerosis imaging," *Interface Focus*, vol. 1, no. 4, pp. 565–575, 2011. DOI:10.1098/rsfs.2011.0024

[33] S. M. Leinders, W. J. Westerveld, J. Pozo, H. P. Urbach, N. de Jong, and M. D. Verweij, "Membrane design of an all-optical ultrasound receiver," in *Proc. IEEE International Ultrasonics Symposium*, Jul. 2012.

[34] C. W. Wong, P. T. Rakich, S. G. Johnson, M. Qi, H. I. Smith, E. P. Ippen, L. C. Kimerling, Y. Jeon, G. Barbastathis, and S.-G. Kim, "Strain-tunable silicon photonic band gap microcavities in optical waveguides," *Applied Physics Letters*, vol. 84, no. 8, pp. 1242–1244, 2004. DOI:http://dx.doi.org/10.1063/1.1649803

[35] B. T. Tung, H. M. Nguyen, D. V. Dao, S. Rogge, H. W. M. Salemink, and S. Sugiyama, "Strain sensitive effect in a triangular lattice photonic crystal hole-modified nanocavity," *Sensors Journal, IEEE*, vol. 11, no. 11, pp. 2657–2663, 2011. DOI:10.1109/JSEN.2011.2157122

[36] W. N. Ye, D.-X. Xu, S. Janz, P. Cheben, M.-J. Picard, B. Lamontagne, and N. G. Tarr, "Birefringence control using stress engineering in silicon-on-insulator (soi) waveguides," *Lightwave Technology, Journal of*, vol. 23, no. 3, pp. 1308–1318, 2005. DOI:10.1109/JLT.2005.843518

[37] L. Fan, L. T. Varghese, Y. Xuan, J. Wang, B. Niu, and M. Qi, "Direct fabrication of silicon photonic devices on a flexible platform and its application for strain sensing," *Optics Express*, vol. 20, no. 18, pp. 20 564–20 575, 2012. DOI:10.1364/OE.20.020564

[38] R. S. Jacobsen, K. N. Andersen, P. I. Borel, J. Fage-Pedersen, L. H. Frandsen, O. Hansen, M. Kristensen, A. V. Lavrinenko, G. Moulin, H. Ou, C. Peucheret, B. Zsigri, and A. Bjarklev, "Strained silicon as a new electro-optic material," *Nature*, vol. 441, pp. 199–202, 2006. DOI:10.1038/nature04706

[39] M. Cazzanelli, F. Bianco, E. Borga, G. Pucker, M. Ghulinyan, E. Degoli, E. Luppi, V. Véniard, S. Ossicini, D. Modotto, S. Wabnitz, R. Pierobon, and L. Pavesi, "Second-harmonic generation in silicon waveguides strained by silicon nitride," *Nature Materials*, vol. 84, pp. 148–154, 2012. DOI:10.1038/nmat3200

[40] J. Cai, Y. Ishikawa, and K. Wada, "Strain induced bandgap and refractive index variation of silicon," *Optics Express*, vol. 21, no. 6, pp. 7162–7170, Mar. 2013.

[41] M. A. Hopcroft, W. D. Nix, and T. W. Kenny, "What is the young's modulus of silicon?" *Microelectromechanical Systems, Journal of*, vol. 19, no. 2, pp. 229–238, 2010. DOI:10.1109/JMEMS.2009.2039697

[42] J. M. Gere and S. P. Timoshenko, *Mechanics of Materials*, 4th SI ed. London: Stanley Thornes, 1999.

[43] S. P. Timoshenko and S. Woinowsky-Krieger, *Theory of Plates and Shells*, 2nd Reissued ed. New York: McGraw-Hill, 1987.

[44] D. Taillaert, W. Bogaerts, P. Bienstman, T. Krauss, P. van Daele, I. Moerman, S. Verstuyft, K. de Mesel, and R. Baets, "An out-of-plane grating coupler for efficient butt-coupling between compact planar waveguides and single-mode fibers," *IEEE Journal of Quantum Electronics*, vol. 38, no. 7, pp. 949–955, Jul. 2002.

[45] W. J. Westerveld, H. P. Urbach, and M. Yousefi, "Optimized 3-d simulation method for modeling out-of-plane radiation in silicon photonic integrated circuits," *Quantum Electronics, IEEE Journal of*, vol. 47, no. 5, pp. 561–568, May 2011. DOI:10.1109/JQE.2010.2099645

[46] Photon Design (Oxford, UK). (2012, Sep.) Fimmwave, a powerful waveguide mode solver. [Online]. Available: http://www.photond.com/products/fimmwave.htm

[47] J. J. Moré, "The levenberg-marquardt algorithm: Implementation and theory," in *Numerical Analysis*, ser. Lecture Notes in Mathematics, G. Watson, Ed. Springer Berlin Heidelberg, 1978, vol. 630, pp. 105–116. DOI:10.1007/BFb0067700

[48] T. O'Haver. (2012, Sep.) Findpeaks matlab function by Tom O'Haver. [Online]. Available: http://terpconnect.umd.edu/~toh/

[49] S. E. Angad Gaur and E. Lagendijk, "Inleiding practicum technische natuurwetenschappen," Reader, Delft University of Technology, Faculty of Applied Sciences, Delft, The Netherlands, 2002, follows the Guide to the Expression of Uncertainty in Measurement (ISO/IEC Guide 98:1993).

[50] P. J. Harmsma, H. Sadeghian, S. M. C. Abdulla, and R. A. Nieuwland, "Wavelength noise in ring resonator sensors," in *Proceedings Symposium IEEE Photonics Society Benelux Chapter*, Mons, 2012.

[51] P. J. Harmsma, J.-P. Staats, D. M. R. Lo Cascio, and L. K. Cheng, "Three-port interferometer in silicon-on-insulator for wavelength monitoring and displacement measurement," in *Lasers and Electro-Optics Europe (CLEO EUROPE/EQEC), 2011 Conference on and 12th European Quantum Electronics Conference*, M unchen, 2011. DOI:10.1109/CLEOE.2011.5943282

[52] C. Mesaritakis, A. Argyris, E. Grivas, A. Kapsalis, and D. Syvridis, "Adaptive interrogation for fast optical sensing based on cascaded micro-ring resonators," *Sensors Journal, IEEE*, vol. 11, no. 7, pp. 1595–1601, 2011. DOI:10.1109/JSEN.2010.2086057

[53] N. Yebo, W. Bogaerts, Z. Hens, and R. Baets, "On-chip arrayed waveguide grating interrogated silicon-on-insulator microring resonator-based gas sensor," *Photonics Technology Letters, IEEE*, vol. 23, no. 20, pp. 1505–1507, 2011. DOI:10.1109/LPT.2011.2162825

[54] J. Song, L. Wang, L. Jin, X. Xia, Q. Kou, S. Bouchoule, and J.-J. He, "Intensity-interrogated sensor based on cascaded fabry-perot laser and microring resonator," *Lightwave Technology, Journal of*, vol. 30, no. 17, pp. 2901–2906, 2012. DOI:10.1109/JLT.2012.2209401

[55] T. Claes, W. Bogaerts, and P. Bienstman, "Vernier-cascade label-free biosensor with integrated arrayed waveguide grating for wavelength interrogation with low-cost broadband source," *Optics Letters*, vol. 36, no. 17, pp. 3320–3322, Sep. 2011. DOI:10.1364/OL.36.003320

[56] L. Jin, M. Li, and J.-J. He, "Optical waveguide double-ring sensor using intensity interrogation with a low-cost broadband source," *Optics Letters*, vol. 36, no. 7, pp. 1128–1130, Apr. 2011. DOI:10.1364/OL.36.001128

[57] D. Mills, "Medical imaging with capacitive micromachined ultrasound transducer (cmut) arrays," in *Ultrasonics Symposium, 2004 IEEE*, vol. 1, Aug 2004, pp. 384–390 Vol.1. DOI:10.1109/ULTSYM.2004.1417744

[58] W. Xia, D. Piras, J. C. van Hespen, S. Van Veldhoven, C. Prins, T. G. van Leeuwen, W. Steenbergen, and S. Manohar, "An optimized ultrasound detector for photoacoustic breast tomography," *Medical physics*, vol. 40, no. 3, p. 032901, 2013.

[59] C. Liu, F. Djuth, Q. Zhou, and K. Shung, "Micromachining techniques in developing high-frequency piezoelectric composite ultrasonic array transducers," *Ultrasonics, Ferroelectrics and Frequency Control, IEEE Transactions on*, vol. 60, no. 12, pp. 2615–2625, Dec 2013. DOI:10.1109/TUFFC.2013.2860

[60] T. Ritter, T. R. Shrout, R. Tutwiler, and K. Shung, "A 30-mhz piezocomposite ultrasound array for medical imaging applications," *Ultrasonics, Ferroelectrics and Frequency Control, IEEE Transactions on*, vol. 49, no. 2, pp. 217–230, Feb 2002. DOI:10.1109/58.985706

[61] G. van Dijk, E. Alles, and K. van Dongen, "A casting-based fabrication process for a high-frequency piezo-electric linear array," in *Ultrasonics Symposium (IUS), 2012 IEEE International*, Oct 2012, pp. 1822–1825. DOI:10.1109/ULTSYM.2012.0457

[62] D. E. Dausch, J. B. Castellucci, D. R. Chou, and O. T. von Ramm, "Piezoelectric micromachined ultrasound transducer (pmut) arrays for 3d imaging probes," in *Ultrasonics Symposium, 2006. IEEE.* IEEE, 2006, pp. 934–937.

[63] G. Caliano, R. Carotenuto, E. Cianci, V. Foglietti, A. Caronti, A. Iula, and M. Pappalardo, "Design, fabrication and characterization of a capacitive micromachined ultrasonic probe for medical imaging," *Ultrasonics, Ferroelectrics and Frequency Control, IEEE Transactions on*, vol. 52, no. 12, pp. 2259–2269, 2005.

[64] O. Oralkan, A. Ergun, J. Johnson, M. Karaman, U. Demirci, K. Kaviani, T. Lee, and B. Khuri-Yakub, "Capacitive micromachined ultrasonic transducers: next-generation arrays for acoustic imaging?" *Ultrasonics, Ferroelectrics and Frequency Control, IEEE Transactions on*, vol. 49, no. 11, pp. 1596–1610, 2002. DOI:10.1109/TUFFC.2002.1049742

[65] F. Akasheh, T. Myers, J. D. Fraser, S. Bose, and A. Bandyopadhyay, "Development of piezoelectric micromachined ultrasonic transducers," *Sensors and Actuators A: Physical*, vol. 111, no. 2, pp. 275–287, 2004.

[66] Y.-F. Wang, T.-L. L. Ren, Y. C. Yang, H. Chen, C.-J. Zhou, L.-G. Wang, and L.-T. T. Liu, "High-density pmut array for 3-d ultrasonic imaging based on reverse-bonding structure," in *Micro Electro Mechanical Systems (MEMS), 2011 IEEE 24th International Conference on*. IEEE, 2011, pp. 1035–1038.

[67] T. Ling, S.-L. Chen, and L. J. Guo, "High-sensitivity and wide-directivity ultrasound detection using high q polymer microring resonators," *Applied physics letters*, vol. 98, no. 20, pp. 204 103–204 103, 2011.

[68] A. Rosenthal, S. Kellnberger, D. Bozhko, A. Chekkoury, M. Omar, D. Razansky, and V. Ntziachristos, "Sensitive interferometric detection of ultrasound for minimally invasive clinical imaging applications," *Laser & Photonics Reviews*, 2014.

[69] P. Morris, A. Hurrell, A. Shaw, E. Zhang, and P. Beard, "A fabry–pérot fiber-optic ultrasonic hydrophone for the simultaneous measurement of temperature and acoustic pressure," *The Journal of the Acoustical Society of America*, vol. 125, no. 6, pp. 3611–3622, 2009.

[70] G. Wild and S. Hinckley, "Acousto-ultrasonic optical fiber sensors: Overview and state-of-the-art," *Sensors Journal, IEEE*, vol. 8, no. 7, pp. 1184–1193, July 2008. DOI:10.1109/JSEN.2008.926894

[71] S.-W. Huang, S.-L. Chen, T. Ling, A. Maxwell, M. ODonnell, L. Jay Guo, and S. Ashkenazi, "Low-noise wideband ultrasound detection using polymer microring resonators," *Applied Physics Letters*, vol. 92, no. 19, pp. 193 509–193 509–3, May 2008. DOI:10.1063/1.2929379

[72] A. Maxwell, S.-W. Huang, T. Ling, J.-S. Kim, S. Ashkenazi, and L. Jay Guo, "Polymer microring resonators for high-frequency ultrasound detection and imaging," *Selected Topics in Quantum Electronics, IEEE Journal of*, vol. 14, no. 1, pp. 191–197, 2008. DOI:10.1109/JSTQE.2007.914047

[73] A. Rosenthal, M. Omar, H. Estrada, S. Kellnberger, D. Razansky, and V. Ntziachristos, "Embedded ultrasound sensor in a silicon-on-insulator photonic platform," *Applied Physics Letters*, vol. 104, no. 2, pp. 021 116–021 116–4, Jan 2014. DOI:10.1063/1.4860983

[74] W. Bogaerts, P. De Heyn, T. Van Vaerenbergh, K. De Vos, S. Kumar Selvaraja, T. Claes, P. Dumon, P. Bienstman, D. Van Thourhout, and R. Baets,

"Silicon microring resonators," *Laser & Photonics Reviews*, vol. 6, no. 1, pp. 47–73, 2012.

[75] W. Bogaerts, S. Selvaraja, P. Dumon, J. Brouckaert, K. De Vos, D. Van Thourhout, and R. Baets, "Silicon-on-insulator spectral filters fabricated with cmos technology," *Selected Topics in Quantum Electronics, IEEE Journal of*, vol. 16, no. 1, pp. 33–44, Jan 2010. DOI:10.1109/JSTQE.2009.2039680

[76] W. Shi, X. Wang, W. Zhang, H. Yun, C. Lin, L. Chrostowski, and N. A. F. Jaeger, "Grating-coupled silicon microring resonators," *Applied Physics Letters*, vol. 100, no. 12, pp. 121 118–121 118–4, Mar 2012. DOI:10.1063/1.3696082

[77] A. Yariv, "Universal relations for coupling of optical power between microresonators and dielectric waveguides," *Electronics Letters*, vol. 36, no. 4, pp. 321–322, Feb 2000. DOI:10.1049/el:20000340

[78] W. Westerveld, S. Leinders, P. Muilwijk, J. Pozo, T. van den Dool, M. Verweij, M. Yousefi, and H. Urbach, "Characterization of integrated optical strain sensors based on silicon waveguides," *Selected Topics in Quantum Electronics, IEEE Journal of*, vol. 20, no. 4, pp. 1–10, July 2014. DOI:10.1109/JSTQE.2013.2289992

[79] S. Timoshenko and S. Woinowsky-Krieger, *Theory of Plates and Shells, 2nd edn.* McGraw-Hill, 1987.

[80] S. Leinders, W. Westerveld, J. Pozo, P. van Neer, K. van Dongen, H. Urbach, N. de Jong, and M. Verweij, "Membrane design of an all-optical ultrasound receiver," in *Ultrasonics Symposium (IUS), 2013 IEEE International*, 2013, pp. 2175–2178.

[81] W. Westerveld, J. Pozo, S. Leinders, M. Yousefi, and H. Urbach, "Demonstration of large coupling-induced phase delay in silicon directional crosscouplers," *Selected Topics in Quantum Electronics, IEEE Journal of*, vol. 20, no. 4, pp. 1–6, July 2014. DOI:10.1109/JSTQE.2013.2292874

[82] J. Pozo, P. Kumar, D. Lo Cascio, A. Khanna, P. Dumon, D. Delbeke, R. Baets, M. Fournier, J.-M. Fedeli, L. Fulbert, L. Zimmermann, B. Tillack, H. Tian, T. Aalto, P. O' Brien, D. Deptuck, J. Xu, X. Zhang, and D. Gale, "Essential : Epixfab services specifically targeting (sme) industrial takeup of advanced silicon photonics," in *14th International Conference on Transparant Optical Networks (ICTON 2012) (invited), United Kingdom*, 2012, p. Mo.B3.5. DOI:10.1109/ICTON.2012.6254391

[83] B. Snyder and P. O'Brien, "Packaging process for grating-coupled silicon photonic waveguides using angle-polished fibers," *Components, Packaging and Manufacturing Technology, IEEE Transactions on*, vol. 3, no. 6, pp. 954–959, June 2013. DOI:10.1109/TCPMT.2012.2237052

[84] Y. Yang, H. Tian, Y.-F. Wang, Y. Shu, C.-J. Zhou, H. Sun, C.-H. Zhang, H. Chen, and T.-L. Ren, "An ultra-high element density pmut array with low crosstalk for 3-d medical imaging," *Sensors*, vol. 13, no. 8, pp. 9624–9634, 2013.

[85] H. F. Zhang, K. Maslov, G. Stoica, and L. V. Wang, "Functional photoacoustic microscopy for high-resolution and noninvasive in vivo imaging," *Nature biotechnology*, vol. 24, no. 7, pp. 848–851, 2006.

[86] F. Jolesz, *Intraoperative imaging and image-guided therapy*. Springer Science & Business Media, 2014.

[87] G. Unsgaard, O. Rygh, T. Selbekk, T. Müller, F. Kolstad, F. Lindseth, and T. N. Hernes, "Intra-operative 3d ultrasound in neurosurgery," *Acta neurochirurgica*, vol. 148, no. 3, pp. 235–253, 2006.

[88] C. Liu, Yanyan, L. Sun, Y. Chen, J. Dai, and W. Qiu, "A novel high-frequency endoscopic ultrasound system for colorectal cancer diagnosis," in *2013 IEEE International Ultrasonics Symposium (IUS)*, July 2013, pp. 2045–2048. DOI:10.1109/ULTSYM.2013.0522

[89] G. Gurun, P. Hasler, and F. L. Degertekin, "A 1.5-mm diameter single-chip cmos front-end system with transmit-receive capability for cmut-on-cmos forward-looking ivus," in *2011 IEEE International Ultrasonics Symposium*, Oct 2011, pp. 478–481. DOI:10.1109/ULTSYM.2011.0115

[90] T. Ma, M. Yu, Z. Chen, C. Fei, K. K. Shung, and Q. Zhou, "Multi-frequency intravascular ultrasound (ivus) imaging," *IEEE Transactions on Ultrasonics, Ferroelectrics, and Frequency Control*, vol. 62, no. 1, pp. 97–107, January 2015. DOI:10.1109/TUFFC.2014.006679

[91] M. Pekař, W. Dittmer, N. Mihajlović, G. van Soest, and N. de Jong, "Frequency agility of collapse-mode capacitive micromachined ultrasonic transducer," *Ieee Transactions on ultrasonics, ferroelectrics and frequency control*, vol. accepted, 2016.

[92] C. Chen, S. B. Raghunathan, Z. Yu, M. Shabanimotlagh, Z. Chen, Z. y. Chang, S. Blaak, C. Prins, J. Ponte, E. Noothout, H. J. Vos, J. G. Bosch, M. D. Verweij, N. de Jong, and M. A. P. Pertijs, "A prototype pzt matrix transducer with low-power integrated receive asic for 3-d transesophageal echocardiography," *IEEE Transactions on Ultrasonics, Ferroelectrics, and Frequency Control*, vol. 63, no. 1, pp. 47–59, Jan 2016. DOI:10.1109/TUFFC.2015.2496580

[93] Y. Lu, H. Y. Tang, S. Fung, B. E. Boser, and D. A. Horsley, "Pulse-echo ultrasound imaging using an aln piezoelectric micromachined ultrasonic transducer array with transmit beam-forming," *Journal of Microelectromechanical Systems*, vol. 25, no. 1, pp. 179–187, Feb 2016. DOI:10.1109/JMEMS.2015.2503336

[94] Y. Hou, J. s. Kim, S. w. Huang, S. Ashkenazi, L. J. Guo, and M. O'Donnell, "Characterization of a broadband all-optical ultrasound transducer-from optical and acoustical properties to imaging," *IEEE Transactions on Ultrasonics, Ferroelectrics, and Frequency Control*, vol. 55, no. 8, pp. 1867–1877, August 2008. DOI:10.1109/TUFFC.2008.870

[95] C. D. Herickhoff, E. D. Light, P. D. Wolf, S. W. Smith, G. A. Grant, and G. W. Britz, "Dual-mode intracranial catheters for minimally-invasive neuro-oncology feasibility study," in *2009 IEEE International Ultrasonics Symposium*, Sept 2009, pp. 1012–1015. DOI:10.1109/ULTSYM.2009.5441798

[96] S. Leinders, W. Westerveld, J. Pozo, P. van Neer, B. Snyder, P. O'Brien, H. Urbach, N. de Jong, and M. Verweij, "A sensitive optical micro-machined ultrasound sensor (omus) based on a silicon photonic ring resonator on an acoustical membrane," *Scientific reports*, vol. 5, 2015.

[97] P. Dumon, G. Priem, L. R. Nunes, W. Bogaerts, D. Van Thourhout, P. Bienstman, T. K. Liang, M. Tsuchiya, P. Jaenen, S. Beckx *et al.*, "Linear and nonlinear nanophotonic devices based on silicon-on-insulator wire waveguides," *Japanese journal of applied physics*, vol. 45, no. 8S, p. 6589, 2006.

[98] E. Hallynck and P. Bienstman, "Integrated optical pressure sensors in silicon-on-insulator," *Photonics Journal, IEEE*, vol. 4, no. 2, pp. 443–450, 2012.

[99] J. McCaulley, V. Donnelly, M. Vernon, and I. Taha, "Temperature dependence of the near-infrared refractive index of silicon, gallium arsenide, and indium phosphide," *Phys. Rev. B*, vol. 49, pp. 7408–7417, Mar 1994. [Online]. Available: http://link.aps.org/doi/10.1103/PhysRevB.49.7408. DOI:10.1103/PhysRevB.49.7408

[100] T. Baehr-Jones, M. Hochberg, C. Walker, E. Chan, D. Koshinz, W. Krug, and A. Scherer, "Analysis of the tuning sensitivity of silicon-on-insulator optical ring resonators," *J. Lightwave Technol.*, vol. 23, no. 12, p. 4215, Dec 2005. [Online]. Available: http://jlt.osa.org/abstract.cfm?URI=jlt-23-12-4215

[101] W. D. Nix, "Mechanical properties of thin films," *Metallurgical and Materials Transactions A*, vol. 20, no. 11, pp. 2217–2245, 1989.

[102] J. Laconte, D. Flandre, and J. P. Raskin, "Thin dielectric films stress extraction," *Micromachined Thin-Film Sensors for SOI-CMOS Co-Integration*, pp. 47–103, 2006.

[103] W. Fang and J. A. Wickert, "Determining mean and gradient residual stresses in thin films using micromachined cantilevers," *Journal of Micromechanics and Microengineering*, vol. 6, no. 3, p. 301, 1996.

[104] W. Fang and J. Wickert, "Post buckling of micromachined beams," *Journal of Micromechanics and Microengineering*, vol. 4, no. 3, p. 116, 1994.

[105] R. Jaccodine and W. Schlegel, "Measurement of strains at si-sio2 interface," *Journal of Applied Physics*, vol. 37, no. 6, pp. 2429–2434, 1966.

[106] S. Greek and N. Chitica, "Deflection of surface-micromachined devices due to internal, homogeneous or gradient stresses," *Sensors and Actuators A: Physical*, vol. 78, no. 1, pp. 1–7, 1999.

[107] H. Tada, A. E. Kumpel, R. E. Lathrop, J. B. Slanina, P. Nieva, P. Zavracky, I. N. Miaoulis, and P. Y. Wong, "Thermal expansion coefficient of polycrystalline silicon and silicon dioxide thin films at high temperatures," *Journal of Applied Physics*, vol. 87, no. 9, pp. 4189–4193, 2000.

[108] X.-Q. Feng and Y. Huang, "Mechanics of smart-cut® technology," *International journal of solids and structures*, vol. 41, no. 16, pp. 4299–4320, 2004.

[109] E. Reissner, "On finite deflections of circular plates," *Proceedings of symposia in applied mathematics*, vol. 1, pp. 213–219, 1949.

[110] J. Voorthuyzen and P. Bergveld, "The influence of tensile forces on the deflection of circular diaphragms in pressure sensors," *Sensors and Actuators*, vol. 6, no. 3, pp. 201–213, 1984.

[111] W. P. Eaton, F. Bitsie, J. H. Smith, and D. W. Plummer, "A new analytical solution for diaphragm deflection and its application to a surface micromachined pressure sensor," in *International Conference on Modeling and Simulation, MSM*, 1999.

[112] Y. Su, K.-S. Chen, D. Roberts, and S. M. Spearing, "Large deflection analysis of a pre-stressed annular plate with a rigid boss under axisymmetric loading," *Journal of Micromechanics and Microengineering*, vol. 11, no. 6, p. 645, 2001.

[113] S. P. Timoshenko and J. M. Gere, *Theory of elastic stability*. Courier Corporation, 2009.

[114] F. Van Keulen and J. Booij, "Refined consistent formulation of a curved triangular finite rotation shell element," *International journal for numerical methods in engineering*, vol. 39, no. 16, pp. 2803–2820, 1996.

[115] D. F. M, *A modern introduction to probability and statistics: understanding why and how*. Springer Science & Business Media, 2005.

[116] Y.-H. Min and Y.-K. Kim, "Modeling, design, fabrication and measurement of a single layer polysilicon micromirror with initial curvature compensation," *Sensors and Actuators A: Physical*, vol. 78, no. 1, pp. 8–17, 1999.

[117] J. Camassel and A. Tiberj, "Strain effects in device processing of silicon-on-insulator materials," *Applied surface science*, vol. 212, pp. 742–748, 2003.

[118] T. G. Bifano, H. T. Johnson, P. Bierden, and R. K. Mali, "Elimination of stress-induced curvature in thin-film structures," *Microelectromechanical Systems, Journal of*, vol. 11, no. 5, pp. 592–597, 2002.

[119] E. Iwase, P.-C. Hui, D. Woolf, A. W. Rodriguez, S. G. Johnson, F. Capasso, and M. Lončar, "Control of buckling in large micromembranes using engineered support structures," *Journal of Micromechanics and Microengineering*, vol. 22, no. 6, p. 065028, 2012.

[120] X. Zhao, J. Tsai, H. Cai, X. Ji, J. Zhou, M. Bao, Y. Huang, D. L. Kwong, and A. Q. Liu, "A nano-opto-mechanical pressure sensor via ring resonator," *Optics express*, vol. 20, no. 8, pp. 8535–8542, 2012.

[121] W. F. Brown Jr, "Thermal fluctuations of a single-domain particle," *Journal of Applied Physics*, vol. 34, no. 4, pp. 1319–1320, 1963.

[122] J. B. Johnson, "Thermal agitation of electricity in conductors," *Phys. Rev.*, vol. 32, pp. 97–109, Jul 1928. [Online]. Available: http://link.aps.org/doi/10.1103/PhysRev.32.97. DOI:10.1103/PhysRev.32.97

[123] B. Gabrielson, "Mechanical–thermal noise in acoustic and vibration sensors," *IEEE Trans Electron Devices*, vol. 40, pp. 903–9, 1993.

[124] P. W. Bridgman, "Note on the principle of detailed balancing," *Phys. Rev.*, vol. 31, pp. 101–102, Jan 1928. [Online]. Available: http://link.aps.org/doi/10.1103/PhysRev.31.101. DOI:10.1103/PhysRev.31.101

[125] H. B. Callen and T. A. Welton, "Irreversibility and generalized noise," *Phys. Rev.*, vol. 83, pp. 34–40, Jul 1951. [Online]. Available: http://link.aps.org/doi/10.1103/PhysRev.83.34. DOI:10.1103/PhysRev.83.34

[126] H. Nyquist, "Thermal agitation of electric charge in conductors," *Phys. Rev.*, vol. 32, pp. 110–113, Jul 1928. [Online]. Available: http://link.aps.org/doi/10.1103/PhysRev.32.110. DOI:10.1103/PhysRev.32.110

[127] F. Reif, *Fundamentals of statistical and thermal physics*. McGraw-Hill,New-York, 1965.

[128] D. Bolmatov, V. Brazhkin, and K. Trachenko, "The phonon theory of liquid thermodynamics," *Scientific reports*, vol. 2, 2012.

[129] J. Frenkel, *Kinetic theory of liquids*. Oxford University Press, 1946.

[130] C. Kittel, "Interpretation of the thermal conductivity of glasses," *Phys. Rev.*, vol. 75, pp. 972–974, Mar 1949. [Online]. Available: http://link.aps.org/doi/10.1103/PhysRev.75.972. DOI:10.1103/PhysRev.75.972

[131] J. R. Hook and H. E. Hall, *Solid State Physics*, 2nd ed. John Wiley and Sons Ltd, 2000.

[132] C. Kittel and H. Kroemer, *Thermal physics*, 2nd ed. Macmillan, 1980.

[133] C. Kittel, *Introduction to solid state physics*, 4th ed. Wiley, 2005.

[134] A. Pierce, *Acoustics: An Introduction to Its Physical Principles and Applications*. Acoustical Society of America, 1989. [Online]. Available: https://books.google.nl/books?id=D8GqhULfKfAC

[135] D. Fleischer, "Power pattern, gain, directivity, effective aperture and stray factor of apraxos," 2003.

[136] J. D. Kraus, "Radio astronomy," *New York: McGraw-Hill, 1966*, vol. 1, 1966.

[137] J. Janjic, M. Shabanimotlagh, G. van Soest, A. van der Steen, N. de Jong, and M. Verweij, "Improving the performance of a 1d ultrasound transducer array by subdicing," 2016.

[138] S. Raghunathan, D. Bera, C. Chen, S. Blaak, C. Prins, M. A. Pertijs, J. G. Bosch, N. de Jong, and M. Verweij, "Design of a miniature ultrasound probe for 3d transesophageal echocardiography," in *Ultrasonics Symposium (IUS), 2014 IEEE International*. IEEE, 2014, pp. 2091–2094.

[139] E. J. Alles, G. J. van Dijk, A. F. W. van der Steen, A. Gisolf, and K. W. A. van Dongen, "An axial array for three-dimensional intravascular ultrasound," in *2012 IEEE International Ultrasonics Symposium*, Oct 2012, pp. 1153–1156. DOI:10.1109/ULTSYM.2012.0287

[140] D. E. Dausch, K. H. Gilchrist, J. R. Carlson, J. B. Castellucci, D. R. Chou, and O. T. von Ramm, "Improved pulse-echo imaging performance for flexure-mode pmut arrays," in *2010 IEEE International Ultrasonics Symposium*, Oct 2010, pp. 451–454. DOI:10.1109/ULTSYM.2010.5935826

[141] A. Hajati, D. Latev, D. Gardner, A. Hajati, D. Imai, M. Torrey, and M. Schoeppler, "Three-dimensional micro electromechanical system piezoelectric ultrasound transducer," *Applied Physics Letters*, vol. 101, no. 25, p. 253101, 2012.

[142] D. Yeager, Y.-S. Chen, S. Litovsky, and S. Emelianov, "Intravascular photoacoustics for image-guidance and temperature monitoring during plasmonic photothermal therapy of atherosclerotic plaques: a feasibility study," *Theranostics*, vol. 4, no. 1, p. 36, 2014.

[143] P. Beard, "Biomedical photoacoustic imaging," *Interface focus*, vol. 1, no. 4, pp. 602–631, 2011.

[144] L. institute of America, *American National Standard for Safe Use of Lasers ANSI Z136.1-2000*. American National Standards Institute, Inc., 2000.

[145] L. V. Wang and S. Hu, "Photoacoustic tomography: in vivo imaging from organelles to organs," *Science*, vol. 335, no. 6075, pp. 1458–1462, 2012.

[146] C. Zhang, S. L. Chen, T. Ling, and L. J. Guo, "Imprinted polymer microrings as high-performance ultrasound detectors in photoacoustic imaging," *Journal of Lightwave Technology*, vol. 33, no. 20, pp. 4318–4328, Oct 2015. DOI:10.1109/JLT.2015.2466661

[147] S. Park, J. Eom, and B. H. Lee, "Photoacoustic signal measurement using thin film fabry-perot optical interferometer for photoacoustic microscopy," in *SENSORS, 2015 IEEE*, Nov 2015, pp. 1–3. DOI:10.1109/ICSENS.2015.7370317

[148] K. Jansen, G. van Soest, and A. F. van der Steen, "Intravascular photoacoustic imaging: a new tool for vulnerable plaque identification," *Ultrasound in medicine & biology*, vol. 40, no. 6, pp. 1037–1048, 2014.

[149] W. Qiu, Y. Chen, X. Li, Y. Yu, W. F. Cheng, F. K. Tsang, Q. Zhou, K. K. Shung, J. Dai, and L. Sun, "An open system for intravascular ultrasound imaging," *IEEE Transactions on Ultrasonics, Ferroelectrics, and Frequency Control*, vol. 59, no. 10, October 2012. DOI:10.1109/TUFFC.2012.2446

[150] M. N. C. Aziz, M. I. M. Salim, A. A. Wahab, and N. A. Manaf, "A feasibility study of ultrasound as a monitoring method for hyperthermia therapy," in *2015 IEEE Student Conference on Research and Development (SCOReD)*, Dec 2015, pp. 407–411. DOI:10.1109/SCORED.2015.7449366

[151] M. G. Ruano and A. E. Ruano, "Towards ultrasound hyperthermia safe treatments using computational intelligence techniques," in *2016 IEEE International Symposium on Medical Measurements and Applications (MeMeA)*, May 2016, pp. 1–6. DOI:10.1109/MeMeA.2016.7533814

[152] S. Abdulla, P. J. Harmsma, R. Nieuwland, J. Pozo, M. Lemmen, H. Sadeghian, J. van den Berg, P. Bodis, and P. Buskens, "Soi based mechano-optical pressure sensor using a folded microring resonator," in *Proc. 9th Nanomechanical sensing workshop (NMC)*, Bombay, India, Jun 2012, pp. 80–81.

Dankwoord

Met dit dankwoord wordt echt het laatste stuk van mijn proefschrift geschreven. Ik kan gelukkig met een goed gevoel terugkijken op deze jaren en ik kan zeker concluderen dat ik ontzettend veel heb geleerd en ben uitgedaagd om tot dit eindresultaat te komen. Dit geldt niet alleen voor het inhoudelijke werk en de praktische uitvoering, maar ook zeker voor alle samenwerking en organisatie die er (nodig) is geweest rondom het onderzoek. Er zijn daarom heel veel personen die in meer of in mindere mate hebben bijgedragen aan dit resultaat en die wil ik daarvoor graag nog bedanken!

Dit onderzoeksproject is voortgekomen uit een idee van Wouter Westerveld en is gehonoreerd door het IOP Photonic Devices programma van het NL agentschap van het ministerie van economische zaken waar ik hen zeer erkentelijk voor ben. Ik ben mijn onderzoek gestart bij Koen van Dongen in de groep Acoustical Wavefield Imaging waar ik hem voor wil bedanken. Met de focus van mijn onderzoek op de nieuwe ultrageluidsensor is mijn begeleiding over gegaan naar Martin Verweij (co-promotor) met ondersteuning van Nico de Jong (promotor) en Paul Urbach (promotor).
Martin, ik ben zeer blij met de manier waarop je mij hebt begeleid. Ik vind je oprechtheid en de directheid waarmee je een gesprek aan gaat zeer prettig. Daarnaast waardeer ik de manier waarop je mensen uitdaagt om verder te zoeken of een probleem op te lossen.
Nico, je bent erg toegankelijk en je bent nauw betrokken geweest bij mijn onderzoek. Ik heb met name je enthousiasme, praktische benadering en input vanuit de medische hoek zeer gewaardeerd.
Paul, je ondersteuning aan het project en de discussies die wij met name in het begin van het onderzoek hebben gehad waren zeer waardevol.

Martin, Nico en Paul, bedankt voor jullie begeleiding.

Tot en met de werking van het prototype heb ik zeer intensief samengewerkt met Wouter Westerveld (Optics Research Group / TNO). Wouter, bedankt voor de leuke samenwerking. Wij vulden elkaar goed aan in het onderzoek. Ik kijk met veel plezier terug op het ontwerpen en maken van het prototype, alle (inhoudelijke) discussies en de vele uren in het lab. Daarnaast zal ik het moment nooit vegeten dat we het prototype voor het eerst in het water stopten en daadwerkelijk een signaal kregen, wat we uiteindelijke gevierd hebben met één of andere stoffige fles wodka in een inmiddels volledig verlaten natuurkunde gebouw.
Wouter werd vanuit TNO begeleid door Mirvais Yousefi en later door Jose Pozo. Kenmerkend is hun enthousiasme, positieve energie voor het project en nuttige commentaar. Peter Harmsma, Remco Nieuwland, Shahina Chakkalakkal en Dario Lo Cascio hebben mij met name ondersteund in de optische metingen en ik wil hen allen bedanken.
De Optics Research groep was de derde werkplek van ons project. Ik wil graag nog Nandini Bhattacharya, Silvania Pereira, Yvonne van Aalst, Roland Horsten en Thim Zuidwijk speciaal noemen en bedanken voor hun betrokkenheid bij het onderzoek en het feit dat ik bij hen ook altijd terecht kon.

Voor het maken van de sensor en de verschillende meetopstellingen wil ik ook graag nog een aantal personen bedanken;
Hans van den Berg (TNO) voor zijn werk aan de sensor met het maken van onder andere de membranen, Pieter O'Brien en Brad Snyder voor het maken van de 'packaging' van de sensor, Aad Poot en Jan de Looff voor het maken van onderdelen van de meetopstelling, Rob Luttjeboer en Tjitte-Jelte Peters voor het gebruik van de clean-room waar de vibrometer metingen zijn uitgevoerd en Patrick van Holst voor zijn hulp met de white light interferometer.

Het maken van goede en betrouwbare mechanische modellen voor onze sensor bleek erg lastig. Ik ben daarom veel dank verschuldigd aan Prof. dr. ir. Fred van Keulen en ir. Rob Dedden voor hun hulp daarin. Zij hebben hun algoritme gebruikt om de rek in de sensor door te rekenen onder verschillende belasting en verschillende begin situaties (Hfd 5.5.2). Met het loskoppelen van de verschillende effecten en de discussies daarover, zijn we dichter bij een volledig model van onze sensor gekomen dat hopelijk in toekomstig onderzoek nog kan worden uitgebreid.

Ik wil de samenwerking met de Biomedical Engineering groep van het Erasmus MC ook graag noemen. Ik kon daar makkelijk binnen lopen voor feedback op de mogelijke medische toepassingen. Daarnaast heb ik redelijk wat meetapparatuur "tijdelijk" van hen geleend.
Paul van Neer en Sandra Blaak wil ik graag bedanken voor hun vriendschap en hulp. Paul, ik ben erg blij met de tijd die jij vanuit je enthousiasme in ons project hebt gestoken met onder andere het uitvoeren van een 'vrijdagmiddag experiment' om te zien of het idee haalbaar was. Daarnaast waardeer ik het zeer dat je zo makkelijk je kennis met me wilde delen.

Sandra, ik waardeer je openheid, het enthousiasme waarmee je PZFlex hebt geïntroduceerd en alle 'rook' momenten op de conferenties.

Ik heb met veel plezier deel uit gemaakt van de groep Acoustical Wavefield Imaging en ik wil daarom iedereen in onze groep bedanken. Ik heb met name een nauwe band gehad met mijn mede- PhD's/PostDoc's van medical acoustics en kamergenoten. Libertario Demi, Erwin Alles, Neslihan Özmen, Sivian Bensdorp, Maysam Shabanimotlagh, Shreyas Raghunathan en Rik Vos, alle inhoudelijke discussies, maar vooral ook voor alle onzinnige discussies, idiote ideeën, uitstapjes en spelletjes darts en basketbal in de kamer hebben er voor gezorgd dat ik met veel plezier mijn onderzoek heb kunnen doen.
Shreyas, ik wil je ook nog specifiek bedanken voor het modelleren van een piëzo-elektrisch element. Jouw resultaten hebben het mogelijk gemaakt om de ruis van een piëzo-elektrisch element te kunnen vergelijken met de ruis van onze sensor (Hfd 6.3.2).
Henry den Bok en Edo Bergsma, door jullie hulp werden al mijn software en hardware problemen, waar ik met grote regelmaat mee te maken had, snel opgelost. Naast jullie technische advies heb ik de gesprekken bij de koffie ook altijd zeer gewaardeerd.
Gerrit van Dijk en Emile Noothout, dankzij jullie expertise en hulp is het mogelijk geweest om de sensoren 'meetklaar' te maken en de meetopstellingen te bouwen. Jullie zijn tegenpolen wat betreft de organisatie van het lab, maar ik heb met jullie beide zeer fijn samengewerkt en de gesprekken en adviezen zeer gewaardeerd.
Margaret van Fessem, door je openheid, nieuwsgierigheid en luisterend oor is er een vriendschap ontstaan gedurende mijn onderzoek. Ik kijk met plezier terug op de gesprekken tijdens de lunch die met name door jouw genuanceerde mening voor vernieuwende inzichten zorgden. Ik heb naast je administratieve hulp ook je organisatie van alle groepsuitjes, kerstborrels, International dinners en alle andere activiteiten zeer gewaardeerd.

Tenslotte wil ik graag mijn familie en schoonfamlie bedanken. Hugo en Marianne, fantastisch hoe jullie mij hebben bijgestaan. Pap, Mam, Marieke, Laurens, Gerard, Bart en Daantje, gedurende het onderzoek zijn er verschillende momenten geweest waarop ik opnieuw mijn richting moest bepalen. Het is dan heel fijn om te weten dat ik altijd op jullie kan terugvallen voor steun en advies.
Bram, ik ben blij met het geluk dat we samen hebben met de komst van Mare en Tjeerd en ik ben je heel dankbaar voor de manier waarop jij mij altijd ondersteunt.

About the author

Suzanne M. Leinders was born in The Hague, the Netherlands on November 15, 1983. She followed secondary school (Gymnasium) at Christelijk Gymnasium Sorghvliet (The Hague, the Netherlands) and graduated in 2002. She went to Delft University of Technology to study Applied Physics. She interrupted her studies for a year in 2005 to take a full-time position as orchestra commissioner in the board of Krashna Musika. After this year she continued her studies in combination with a position in the board of Delft Challenge as skipper of a sailing team. Se sailed several sailing regattas including the Tour the France à la voile in 2007 and 2008. After this experience she focused on her studies and started the master programme. During her master she went for an internship at Philips (Eindhoven, the Netherlands) to measure on the skin and skin structures using 3D Polarization sensitive optical coherence tomography. Her M.Sc. graduation project was a collaboration between the Daniel den Hoed kliniek and the department of radiation science & technology. The project focused on the possible gain in adaptive radiotherapy for liver stereotactic body radiation therapy (SBRT) compared with the clinical protocol. She received her Master degree in 2010. After her graduation she was employed as a scientific researcher at the Daniel den Hoed kliniek to publish on her graduation work. In march 2011, she started her Ph.D. research on the design, fabrication and validation of an ultrasound sensor based on integrated photonics. This research led to this Thesis.

Publications of the author

Papers in preparation

- S. M. Leinders, N. de Jong, and M. D. Verweij, "Acoustical noise for sensor with a small spatial footprint," in preparation
- S. M. Leinders, W. J. Westerveld, P. L. M. J. van Neer, H. P. Urbach, N. de Jong, and M. D. Verweij, "Characterization of an optical micro-machined ultrasound sensor (OMUS) based on a silicon photonic ring resonator on an acoustical membrane," in preparation

Journal publications

- S. M. Leinders, W. J. Westerveld, J. Pozo, P. L. M. J. van Neer, B. Snyder, P. O'Brien, H. P. Urbach, N. de Jong, and M. D. Verweij, "A sensitive optical micro-machined ultrasound sensor (OMUS) based on a silicon photonic ring resonator on an acoustical membrane," *Scientific Reports*, vol. 5, 2015, DOI:10.1038/srep.14328
- W. J. Westerveld, J. Pozo, S. M. Leinders, M. Yousefi, and H. P. Urbach, "Demonstration of large coupling-induced phase delay in silicon directional cross-couplers," *IEEE Journal of Selected Topics in Quantum Electronics*, vol. 20, no. 4, 2014, DOI:10.1109/JSTQE.2013.2292874
- W. J. Westerveld, S. M. Leinders, P. M. Muilwijk, J. Pozo, T. C. van den Dool, M. D. Verweij, M. Yousefi, and H. P. Urbach, "Characterization of integrated optical strain sensors based on silicon waveguides," *IEEE Journal of Selected Topics in Quantum Electronics*, vol. 20, no. 4, 2014, DOI:10.1109/JSTQE.2013.2289992

- W. J. Westerveld, S. M. Leinders, K. W. A. van Dongen, H. P. Urbach, and M. Yousefi, "Extension of Marcatili's analytical approach for rectangular silicon optical waveguides," *Journal of Lightwave Technology*, vol. 30, no. 14, pp. 2388–2401, 2012. DOI:10.1109/JLT.2012.2199464

- W. J. Westerveld, J. Pozo, P. J. Harmsma, R. Schmits, E. Tabak, T. C. van den Dool, S. M. Leinders, K. W. A. van Dongen, H. P. Urbach, and M. Yousefi, "Characterization of a photonic strain sensor in silicon-on-insulator technology," *Optics Letters*, vol. 37, no. 4, pp. 479–481, Feb 2012. DOI:10.1364/OL.37.000479

- S. M. Leinders, S. Breedveld, A. Méndez Romero, D. Schaart, Y. Seppenwoolde, and B. J. M. Heijmen, "Adaptive Liver Stereotactic Body Radiation Therapy: Automated Daily Plan Reoptimization Prevents Dose Delivery Degradation Caused by Anatomy Deformations," *International Journal of Radiation Oncology, Biology, Physics*, vol. 87. no. 5, pp.1016–1021, 2013. DOI:S0360-3016(13)02965-9

Proceedings

- S. M. Leinders, W. J. Westerveld, J. Pozo, P. L. M. J. van Neer, K. W. A. van Dongen, H. P. Urbach, N. de Jong, and M. D. Verweij, "First measurements on a novel type of optical micro-machined ultrasound transducer (OMUT)," in *Proceedings IEEE International Ultrasonics Symposium*, Chicago, Sep. 2014, pp. 2572–2575.

- S. M. Leinders, W. J. Westerveld, J. Pozo, P. L. M. J. van Neer, K. W. A. van Dongen, H. P. Urbach, N. de Jong, and M. D. Verweij, "Membrane design of an all-optical ultrasound receiver," in *Proceedings IEEE International Ultrasonics Symposium*, Prague, Jul. 2013, pp. 2175–2178.

Conference contributions

- S. M. Leinders, N. de Jong, and M. D. Verweij, "Acoustical noise for sensor with a small spatial footprint," in *The Journal of the Acoustical Society of America*, Honolulu, November 2016,

- S. M. Leinders, W. J. Westerveld *(presenting)*,"Sensitive optical micro-machined ultrasound sensors based on a silicon photonic ring resonator on an acoustical membrane," in *EMN Meeting on Photonics*, Barcelona, Spain, September 2016 *(invited)*

- S. M. Leinders, W. J. Westerveld, J. Pozo, P. L. M. J. van Neer, H. P. Urbach, N. de Jong, and M. D. Verweij,"Design and characterization of a sensitive optical micro-machined ultrasound transducer," in *The Journal of the Acoustical Society of America*, Pittsburgh, May 2015, vol 137. no. 4, pp. 2426–2426

- W. J. Westerveld, J. Pozo, S. M. Leinders, M. Yousefi, and H. P. Urbach, "Characterization of silicon micro-ring resonators," in *18th Annual Symposium of the IEEE Photonics Society Benelux Chapter*, Eindhoven, Nov. 2013, pp. 37–40.

- W. J. Westerveld, J. Pozo, P. M. Muilwijk, S. M. Leinders, P. J. Harmsma, E. Tabak, T. C. van den Dool, K. W. A. van Dongen, M. Yousefi, and H. P. Urbach, "Characterization of optical strain sensors based on silicon waveguides," in *Conference on Lasers and Electro-Optics Europe 2013 and the European Quantum Electronics Conference (CLEO Europe - EQEC 2013)*, München, May 2013, CH3.4.

- W. J. Westerveld, S. M. Leinders, J. Pozo, K. W. A. van Dongen, M. Yousefi, N. de Jong, M. D. Verweij, and H. P. Urbach, "All-optical ultrasound receiver in silicon-on-insulator technology," in *Optics in Cardiology*, Rotterdam, Mar. 2013.

- S. M. Leinders, W. J. Westerveld, J. Pozo, M. Yousefi, H. P. Urbach, and K. W. A. van Dongen, "Membrane design of an all-optical ultrasound receiver in silicon-on-insulator technology," in *4th Dutch Bio-Medical Engineering Conference*, Egmond aan Zee, The Netherlands, Jan. 2013.

- W. J. Westerveld, S. M. J. Pozo, Leinders, K. W. A. van Dongen, M. Yousefi, and H. P. Urbach, "Extension of Marcatili's analytical approach for 220 nm high waveguides in SOI technology," in *17th Annual Symposium of the IEEE Photonics Society Benelux Chapter*, Mons, Nov. 2012, pp. 25–28. [Online]. http://www.photonics-benelux.org

- W. J. Westerveld, J. Pozo, R. A. Nieuwland, S. M. Leinders, K. W. A. van Dongen, and M. Yousefi, "Experimental confirmation of universal relations for microring resonators in SOI technology," in *European Optical Society Annual Meeting (EOSAM 2012)*, Aberdeen, Sep. 2012, Presentation nr. 5995.

- W. J. Westerveld, J. Pozo, R. A. Nieuwland, S. M. Leinders, K. W. A. van Dongen, M. Yousefi, and H. P. Urbach, "Experimental confirmation of universal relations for microring resonators in SOI technology," in *16th European Conference on Integrated Optics (ECIO)*, Barcelona, Apr. 2012, Oral Nr. 187.

- W. J. Westerveld, J. Pozo, P. J. Harmsma, R. Schmits, E. Tabak, S. M. Leinders, K. W. A. van Dongen, H. P. Urbach, and M. Yousefi, "Characterization of the effects that play a role in photonic strain sensors in silicon-on-insulator technology," in *16th Annual Symposium of the IEEE Photonics Society Benelux Chapter*, Gent, Dec. 2011, pp. 69–72. [Online]. http://www.photonics-benelux.org